SCUOLA DI DOTTORATO
UNIVERSITÀ DEGLI STUDI DI MILANO-BICOCCA

Department of Earth and Environmental Sciences (DISAT)

PhD program in Chemical, Geological and Environmental Sciences

Cycle XXX

Curriculum in Environmental Sciences

Development of novel methods to evaluate vegetation status from multi-source remote sensing data

Surname: Celesti
Name: Marco
Registration number: 758963

Tutor: Dr. Colombo Roberto
Supervisor: Dr. Rossini Micol

Coordinator: Prof. Frezzotti Maria Luce

ACADEMIC YEAR 2016/2017

CONTENTS

LIST OF FIGURES

LIST OF TABLES

ACRONYMS

APAR	Absorbed Photosynthetically Active Radiation
ATP	adenosine triphosphate
C_{ab}	chlorophyll a+b content
CCFI	Canopy Cover Fluorescence Index
CHM	Canopy Height Model
CO_2	carbon dioxide
DASF	Directional Area Scattering Factor
DAT	Days After Treatment
DOY	Day Of the Year
DTM	Digital Terrain Model
ETC	Effective Transmittance Correction
ESA	European Space Agency
F	chlorophyll a fluorescence
Fy	fluorescence yield
Fy^*	apparent fluorescence yield
fAPAR	fraction of Absorbed Photosynthetically Active Radiation
fc	vegetation fractional cover
f_{esc}	fluorescence escape probability
FLD	Fraunhofer Line Depth
FLEX	FLuorescence EXplorer
FOV	Field Of View
F_R	fluorescence in the red region (*i.e.*, $\approx 690\,nm$)

$\mathbf{F_{FR}}$	fluorescence in the far-red region (*i.e.*, $\approx$ 740–760 nm)
FWHM	Full Width at Half Maximum
$\Phi_\mathbf{F}$	fluorescence quantum yield
G-LiHT	Goddard LiDAR, Hyperspectral and Thermal
GPP	Gross Primary Production
$\mathbf{g_s}$	Leaf level stomatal conductance
iFLD	improved Fraunhofer Line Depth
IFOV	Instantaneous Field Of View
LAI	Leaf Area Index
Ψ_{leaf}	leaf water potential
LET	Linear Electron Transport
LiDAR	Light Detection And Ranging
LUE	Light Use Efficiency
LWIR	Long Wave InfraRed
MTCI	Meris Terrestrial Chlorophyll Index
NASA	National Aeronautics and Space Administration
NDVI	Normalized Difference Vegetation Index
NEE	Net Ecosystem Exchange
NIR	Near InfraRed
NO	Numerical Optimization
NPQ	Non-Photochemical Quenching
OLS	Ordinary Least Squares
PAR	Photosynthetically Active Radiation
$\mathbf{P_{net}}$	net photosynthesis
PQ	Photochemical Quenching

PRI	Photochemical Reflectance Index
PSI	photosystem I
PSII	photosystem II
ρ	reflectance
RS	Remote Sensing
Reco	ecosystem respiration
RMSE	Root Mean Squared Error
ROI	Region Of Interest
RRMSE	Relative Root Mean Squared Error
RT	Radiative Transfer
RTM	Radiative Transfer Model
S3	Sentinel-3
SFM	Spectral Fitting Methods
SI	Site Index
SSI	Spectral Sampling Interval
SVAT	Soil-Vegetation-Atmosphere Transfer
SVD	Singular Vector Decomposition
SWIR	Short Wave InfraRed
SZA	Sun Zenith Angle
TIN	Triangulated Irregular Network
UAV	Unmanned Aerial Vehicles
VI	Vegetation Index
VNIR	Visible and Near InfraRed
λ	wavelength

ABSTRACT

Hyperspectral Remote Sensing (RS) data have been exploited in the last decades to successfully retrieve information about plant properties at different scales. This thesis focuses on the use of state of the art hyperspectral RS data to retrieve vegetation status at canopy level, using both experimental and modeled data. In the last years, RS of solar-induced chlorophyll a fluorescence (F) emerged as a novel and promising scientific field for studying the dynamic behavior of photosynthesis. F is a physical side product of chlorophyll a light absorption that is emitted as an electromagnetic radiation in the red and far-red spectral regions ($\approx$ 640 to 850 nm), and it is related to the energetic status of the photosystems. Nevertheless, apart from physiology F is concurrently influenced by leaf and canopy structure, pigment concentration and weather/illumination conditions, and its unambiguous interpretation is still challenging. This drives the interest in exploring F-derived metrics able to disentangle the physiological information from the remotely sensed F signal.

The main aim of this Ph.D. was to exploit multi-source remote sensing data to improve vegetation status analysis from above. In particular, I focused on using F, and F-derived metrics, in the red and far-red spectral regions together with hyperspectral reflectance in the Visible and Near InfraRed (VNIR) spectral region, as a tool for monitoring variation in the photosynthetic efficiency of plants in different conditions. The studies presented in this thesis are aimed at exploring the capacity of F and complementary RS-derived variables to track changes in plant physiology due to age-related hydraulic limitation in a pine forest (Chapter 2) and track changes in photosynthetic efficiency due to the application of an abiotic stressor on a lawn (Chapters 3, 4).

The results show that the two peaks of the chlorophyll fluorescence spectrum were accurately estimated from high resolution spectral data collected on the ground and using the high-performance imaging spectrometer HyPlant. Different strategies to take into account the effects of varying illumination conditions and biochemical/structural vegetation parameters on the F signal were applied by means of empirical and physically based models. F-derived metrics in the red region proved to be more sensible to variations in the functional state of the photosynthetic machinery than those in the far-red. This was particularly true in regards to changes in plant physiology in aging loblolly pines, where the decline in red fluorescence yield was explained as a response of the increasing hydraulic

limitation experienced by taller and older plants. Moreover, it was also observed as a faster quenching of the initial rise of red fluorescence yield in the manipulated stress experiment. Nevertheless, in this experiment both red and far-red fluorescence were highly sensible to quick changes in photosynthetic efficiency. In general, additional biophysical and physiological parameters were necessary to interpret the spatial and temporal changes in fluorescence. By combining the information provided by the solar-induced fluorescence, the canopy reflectance, and in one case the canopy temperature, it was possible to derive conceptual models that explained the most relevant events that occurred in the photosynthetic apparatus. When available, these findings were derived independently from both ground-based and aerial (even if with larger uncertainties) RS measurements using high-performance spectrometry. These studies are among the few where red and far-red F, and not only far-red F, were successfully estimated and exploited at canopy level from airborne measurements. The achieved results enforce the importance of retrieveing this signal for vegetation monitoring. Moreover, through the inversion of a coupled physically based radiative transfer model, for the first time the full spectrum of canopy F, the fluorescence quantum yield (Φ_F), as well as the main vegetation parameters that control light absorption and reabsorption, were retrieved concurrently using very-high resolution measured apparent reflectance data. F values were compared to those retrieved with state-of-the-art spectral fitting methods showing very strong correlation, while Φ_F values agreed well with an independent biophysical model for fluorescence and photosynthesis. The effects of pigment content, leaf/canopy structural parameters and physiology were effectively discriminated, and their combined observation over time led to the recognition of dynamic patterns of stress adaptation and stress recovery in the plants.

Overall, the results achieved in this thesis foster the use of hyperspectral RS to obtain information about plant status. In particular, they indicate that F yields coupled with observations of complementary RS parameters, can be effective indicators of the dynamic behavior of the photosynthetic machinery of the plants. Putting this into the perspective of a repeated (or continuous) observation through RS platforms, it will be possible to characterize stress-specific patterns and to effectively distinguish between acute stress events and prolonged stress phases, monitoring their implications on the long-term functioning of the vegetation.

1 INTRODUCTION

Hyperspectral Remote Sensing (RS) data have been exploited in the last decades to successfully retrieve information about plant properties at different scales (Thenkabail, Lyon, and Huete, 2012). The inherent strength of RS techniques for monitoring terrestrial ecosystems resides in their ability to cope with processes that are highly dynamic, both spatially and temporally at a relevant scale for describing them. This thesis focuses on the use of state-of-the-art hyperspectral data to retrieve vegetation status at canopy level, using both experimental and modeled data. Terrestrial vegetation plays a critical role in the global biogeochemical cycles (Franklin et al., 2016), and as any other element in the Earth-surface system, its energy budget is strongly driven by solar radiation through a complex system of processes (*e.g.*, Monson and Baldocchi 2013; Ramanathan 1987). From a physiological point of view, the key process that originates from this interaction is photosynthesis. Photosynthesis is the main mechanism used by plants to fix atmospheric carbon dioxide (CO_2) as organic compounds, storing light energy that can be used to sustain the growth of the organism. With an estimated uptake of more than $120\,Pg\,C\,year^{-1}$ (Beer et al., 2010), it is the largest CO_2 flux on Earth.

Photosynthesis is a highly dynamic process that can be divided in two steps: i) the light reactions; and ii) the carbon reactions. In the light reactions (Figure 1, upper part), the process starts with the interaction between the radiation and the vegetation elements. Part of the Photosynthetically Active Radiation (PAR), defined as the incoming light between 400 and 700 nm, is absorbed by the vegetation pigments (mainly by chlorophyll molecules), bound by proteins to form photosynthetic antenna complexes (Liu et al., 2004). This amount is defined as Absorbed Photosynthetically Active Radiation (APAR), and it is mathematically described as the product of PAR and of the fraction of Absorbed Photosynthetically Active Radiation (fAPAR). fAPAR, in turn, is a property that describes the capability of a vegetation element (*e.g.*, leaf, canopy) to absorb the incoming PAR. The amount of incoming radiation that is not absorbed, can be reflected or transmitted by the vegetation elements. Most of the APAR is moved from the antenna complexes to the reaction centers of photosystem I (PSI) and photosystem II (PSII) (P700 and P680, respectively), specialized pigment-protein complexes able to convert the excitation energy into chemical energy. These two photosystems are present in higher plants and act in reverse order, moving electrons from PSII to PSI in a series of reac-

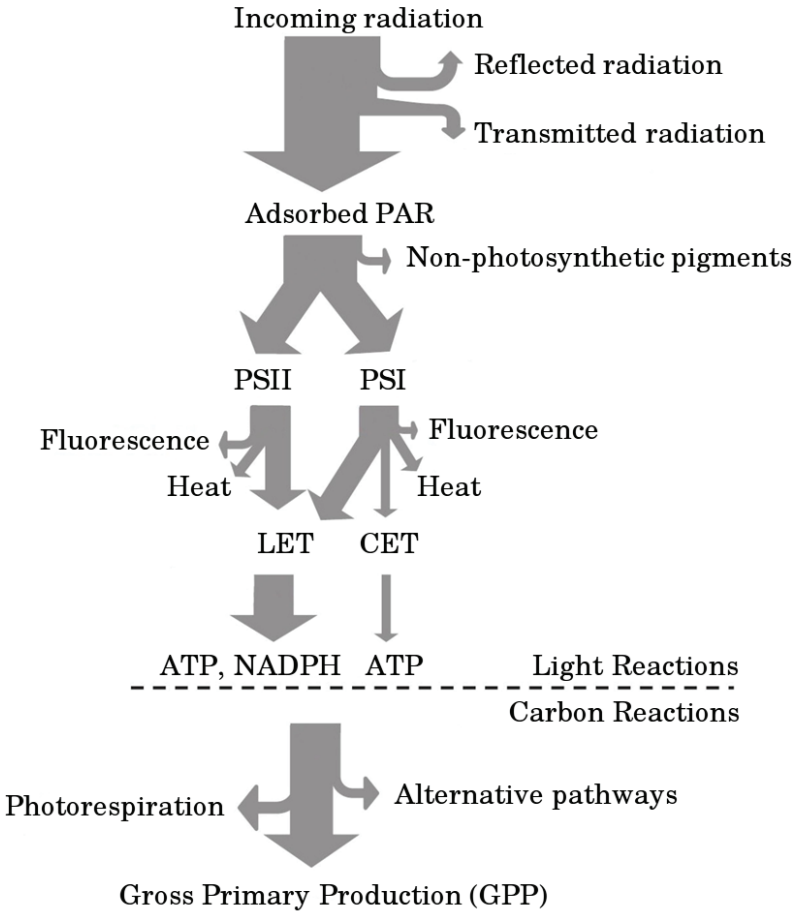

Figure 1: Photosynthetic energy partitioning at the leaf level in the light reactions and in the carbon reactions. Grey arrows represent the flow of energy. Optical signals available to remote sensing include properties of reflected and transmitted light, and chlorophyll a fluorescence. LET, linear electron transport; CET, cyclic electron transport (modified from Porcar-Castell et al., 2014).

tions that form the Linear Electron Transport (LET) (Porcar-Castell et al., 2014). In optimal conditions, most of the energy absorbed by PSII is used for photochemistry (Photochemical Quenching (PQ)), storing the chemical energy in high-energy compounds like adenosine triphosphate (ATP) and NADPH. This energy, can be potentially used for feeding the carbon reactions, where the actual synthesis of carbohydrates takes place (Figure 1, lower part). Following the Light Use Efficiency (LUE) model proposed by (Monteith 1972; Eq. 1), the complex mechanisms that regulate the conversion of APAR into Gross Primary Production (GPP) (*i.e.*, gross photosynthesis) can be expressed with an efficiency factor (LUE_p, or ϵ_p).

$$GPP = PAR \times fAPAR \times LUE_P \tag{1}$$

The amount of absorbed energy not used for PQ has to be quickly released from the photosystems in order to minimize the chances of formation of harmful reactive species. Stress events, to be intended as unfavorable (sub-optimal) growing conditions, can modulate LUE_p inhibiting one or both phases of the photosynthetic process, lowering the actual rates of photosynthesis and threatening the energetic balance. Potentially, these stressed conditions can lead to losses in vegetation health and production with different grades of severity. The capability of the plant to recover from these events is determined by the intensity and the persistence of the stress, but also by the resistance and resilience of the plant to it. Water and nutrient limitation, light intensity, temperature and exposure to oxidant species are among the most common environmental limiting factors for photosynthesis (*e.g.*, Chapin III et al. 1987).

Plants, for their part, evolved many processes to maximize the energy balance between the two phases of photosynthesis (*e.g.*, Walters 2005). Among these, the excess energy at the photosystem level is largely dissipated non-radiatively as heat (Non-Photochemical Quenching (NPQ)) or is emitted at slightly longer wavelength as chlorophyll a fluorescence (F) (*e.g.*, Demmig-Adams and Adams 2006; Flexas et al. 2002). F is a physical side product of light absorption that is emitted as an electromagnetic radiation in the red and far-red spectral regions ($\approx$ 640–850 nm), with two peaks around 690 nm and 740 nm (Figure 2). PSI absorbs at slightly longer wavelengths than PSII, and its contribution to the total emitted fluorescence signal is relatively lower and more constant than the one of PSII (*e.g.*, Genty, Wonders, and Baker 1990). From a spectral point of view, PSI contributes more to fluorescence in the far-red region (*i.e.*, $\approx$ 740–760 nm) (F_{FR}), while PSII has a strong contribution on both fluorescence in the red region (*i.e.*, $\approx$ 690 nm) (F_R) and F_{FR} (Franck, Juneau, and Popovic, 2002).

At leaf scale, the fast dynamics of F actively induced with artificial light sources have been studied for decades to obtain information on plant photosynthetic activity, and they helped elucidating many important features of the mechanism

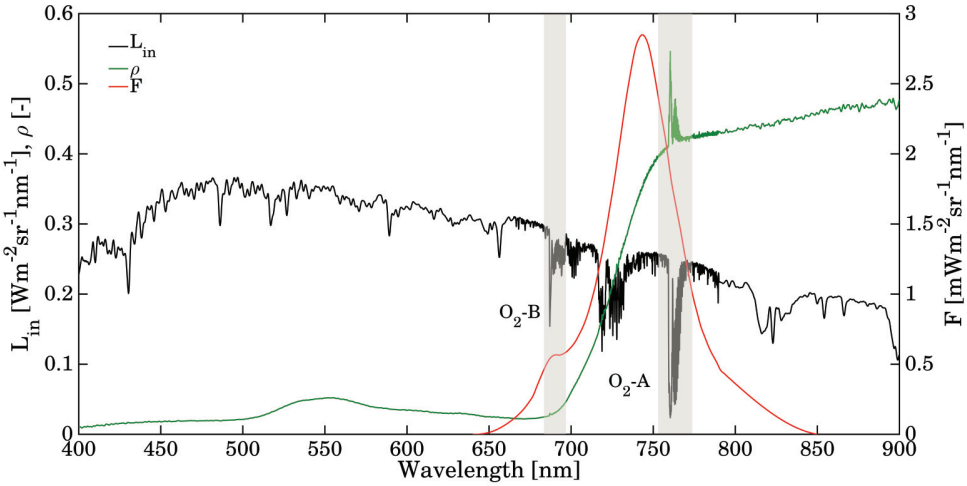

Figure 2: Incoming radiance (L_{in}; black line), reflectance (ρ; green line) and solar-induced chlorophyll a fluorescence (F; red line). The two spectral windows of the O_2-B and the O_2-A oxygen absorption features are highlighted by shadowed areas.

of photosynthesis (Papageorgiou and Govindjee, 2004; Porcar-Castell et al., 2014). Nevertheless, this technique is impractical at larger scales due to technical constrains. As it is, no direct measure of photosynthesis is available at these scales, and the modeled products show large residual uncertainties (Beer et al., 2010), and lack a spatially distributed independent benchmark. In natural conditions, F generates from the absorption of light emitted by the Sun (solar-induced chlorophyll fluorescence, herein F), and it is a relatively weak signal compared to the reflected radiance (≈ 1-5%).

In the last years, RS of F emerged as a novel and promising scientific field for studying the dynamic behavior of photosynthesis (for a review of this topic see Meroni et al., 2009 and Porcar-Castell et al., 2014), since the possibility to retrieve it without using artificial light sources (*i.e.* passively) opens new perspectives for its use at ecosystem, regional or global scale. In fact, the feasibility of consistent retrievals of F has been successfully investigated in the last years from ground based platforms (Julitta et al., 2016; Rossini et al., 2016), Unmanned Aerial Vehicless (UAVs) (Garzonio et al., 2017; Zarco-Tejada et al., 2013), airplanes (Rascher et al., 2015; Rossini et al., 2015) and satellites (Cogliati et al., 2015; Guanter et al., 2015, 2010; Joiner et al., 2016), with a strong impulse given by the activity supporting the recently selected Earth-Explorer 8 FLuorescence EXplorer (FLEX) satellite mission, of the European Space Agency (ESA), specifically intended for global-scale F retrieval from space. FLEX will fly in tandem with the ESA Coper-

nicus Sentinel-3 (S3) satellite ("FLEX-S3" tandem mission), providing F estimates in both the red and far-red regions, as well as complementary products derived from Visible and Near InfraRed (VNIR) reflectance, with an unprecedented spatial resolution (pixel size 300 m × 300 m). In fact, starting from 2012, ESA organized a series of campaigns to test technical and scientific hypothesis to support the FLEX mission. In these campaigns, state-of-the-art ground spectroradiometers where employed together with the innovative HyPlant airborne sensor (Rascher et al., 2015), a precursor of the FLEX optical payload optimized for F retrieval in the red and far-red spectral regions.

The major challenge in the passive F retrieval from RS data is the decoupling of the small F signal from the much higher radiance reflected by the surface (*i.e.*, the vegetation). The F signal is relatively stronger, and can be more easily detected passively, in narrow regions of the spectrum in which irradiance at ground level is strongly reduced. These can be due to dark lines in the solar emission spectrum (*i.e.*, Fraunhofer lines) or to the absorption of radiation within the atmosphere (*i.e.*, *telluric* features). The main telluric features which have been exploited for F estimation are the oxygen (O_2) absorption bands in the Earth atmosphere, O_2-B (centered at 687.0 nm) and O_2-A (centered at 760.4 nm) (Figure 2, grey bands). F is usually retrieved from high spectral resolution radiance measurements using algorithms based either on the Fraunhofer Line Depth (FLD) principle (Plascyk, 1975), the Spectral Fitting Methods (SFM) (Meroni and Colombo, 2006) or the Singular Vector Decomposition (SVD) (Guanter et al., 2012). Recently, Cogliati et al. (2015) and Liu et al. (2015) proposed innovative spectral fitting methods to retrieve the full spectrum of emitted F, opening new perspectives for the development of higher level F products (*e.g.*, quantify the total F flux emitted at the top of the canopy).

A growing body of scientific studies shows that remotely sensed F can be used to track the physiological behavior of plants at several spatial and temporal scales of interest (*e.g.* Damm et al. 2010; Guanter et al. 2014; Köhler et al. 2017; Meroni et al. 2008; Rossini et al. 2015; Rossini et al. 2010; Sun et al. 2017; Walther et al. 2016; Wieneke et al. 2016; Yang et al. 2015; Zhang et al. 2014). Nevertheless, most of these studies did not properly consider that apart from physiology, F is concurrently influenced by leaf and canopy structure, pigment concentration and weather/illumination conditions (Porcar-Castell et al., 2014; Verrelst et al., 2015b). The variability of these factors across space and time can mask, or erroneously emphasize, the variation of F linked to the physiology of the plant, and its unambiguous interpretation is still a largely unsolved challenge. This is especially true in stressed conditions where the energy partitioning between PQ, NPQ and F can be highly varied (Schulze and Caldwell, 1995). On the other hand, these conditions are also among the most interesting cases of application for F, because

traditional RS techniques often fail to identify the stress events before a visible (and not easily reversible) damage occurs (*e.g.* Rossini et al. 2015). Moreover, the vast majority of canopy level studies exploited only F_{FR}, while there is evidence that the combined observation of both F_{FR} and F_R observations can offer additional insights for stress/productivity detection (*e.g.*, Ač et al. 2015; Daumard et al. 2010; Joiner et al. 2016; Middleton et al. 2015), and carry information from different layers of a leaf or a canopy (Gitelson, Buschmann, and Lichtenthaler, 1998; Porcar-Castell et al., 2014). This limitation is mostly driven by the fact that most sensors onboard airborne or satellite platforms that have been used for F retrieval are not optimized for this task, and lack either the spectral range or the spectral resolution to retrieve F_R, or the full spectrum of F.

Following (*e.g.*) Lee et al. (2013), adapting the formulation of the LUE model (Monteith, 1972) the F flux emitted at the top of the vegetation canopy (*i.e.* the quantity directly retrievable from canopy level RS data) can be expressed as a function of the PAR, of the fAPAR, of the LUE_F and of the fluorescence escape probability (f_{esc}) (Eq. 2).

$$F(\lambda) = PAR \times fAPAR \times f_{esc}(\lambda) \times LUE_F(\lambda) \tag{2}$$

$LUE_F(\lambda)$ is the fraction of absorbed PAR emitted as fluorescence at wavelength λ, while $f_{esc}(\lambda)$ is the probability that an emitted fluorescence photon escapes the canopy in the observation direction. LUE_F is not directly measurable at canopy level, but hyperspectral RS data can be used to retrieve information about the first three terms of Eq. 2, and calculate LUE_F consequently from F. Nevertheless, fAPAR estimates from RS are still affected by large errors (Meroni et al., 2013; Pickett-Heaps et al., 2014), and besides the conceptual definition of f_{esc}, its proper quantitative description and quantification from RS is still debated and varies with wavelength (λ). Even neglecting second order complex mechanisms of emission/reabsorption throughout the canopy, the proper computation of LUE_F would imply measuring the full spectrum of emitted F from every observation direction. RS data are rarely able to provide this information, and several proxies for LUE_F have been proposed over time. Among these, the most widely used are the fluorescence yield (Fy) (*i.e.*, the ratio between F and APAR) and the apparent fluorescence yield (Fy^*) (*i.e.*, the ratio between F and PAR). On the other hand, in photosynthesic studies it is practical to use the concept of *quantum yield* to describe the quantum efficiency of the process of fluorescence emission (fluorescence quantum yield (Φ_F)) at photosystem level, but Φ_F can not be measured from above and a modeling step is mandatory to retrieve it from RS data.

RS techniques have the potential to retrieve vegetation parameters that have a direct impact on the Radiative Transfer (RT) of the radiation reflected, transmitted and emitted by the target. These can be biochemical (*e.g.*, pigments content,

dry matter content) or structural parameters (*e.g.*, leaf inclination, Leaf Area Index (LAI), vegetation fractional cover (fc)), characterized at leaf or canopy level, and their link with RT fluxes is described from a variety of empirical and physical models (Verrelst et al., 2015a). Vegetation Indices (VIs) have been widely used as simple numerical indicators of a single vegetation property, building empirical relationships between measurements of a vegetation property and the associated VI value. They are mathematical combinations of two or more bands, that have been increasing in number along with the development of optical sensors. They are generally easy to calculate from RS data, and, although quite effective, the relationships with vegetation parameters are limited to their empirical domain. On the other hand, physically-based Radiative Transfer Models (RTMs) of the vegetation have been used in the last decades to express mathematically the complex interactions between vegetation elements (*e.g.*, tissues, leaves, branches) and the electromagnetic radiation. Some of these models also include interactions with the soil and the atmosphere (Verhoef and Bach, 2003, 2007). In addition to that, Soil-Vegetation-Atmosphere Transfer (SVAT) models (*e.g.*, Sellers 1997; van der Tol et al. 2009; Verhoef and Allen 2000) have been proposed to describe the pathways of energy, carbon and water between soil, vegetation and atmosphere. Among these, the 1-D (vertical) "Soil-Canopy Observation Photosynthesis and Energy fluxes" (SCOPE) model (van der Tol et al., 2009) is an integrated radiative transfer and energy balance model that enables the simulation of canopy leaving hyperspectral reflectance and fluorescence, as well as the turbulent heat fluxes and photosynthesis. It is based on the vastly used PROSPECT (Jacquemoud and Baret, 1990) and the "Scattering by Arbitrary Inclined Leaves" (SAIL) models (Verhoef, 1984) (for a review of application see Jacquemoud et al. 2009), and it is the most commonly used RTM for RS fluorescence applications.

Several approaches have been proposed to retrieve vegetation parameters from the inversion of these RTMs (Verrelst et al., 2015a). For example, van der Tol et al. (2016) successfully exploited high resolution (Spectral Sampling Interval (SSI) = 0.24 nm and Full Width at Half Maximum (FWHM) = 1 nm) top-of-canopy reflectance spectra in the VNIR spectral region, to partially invert SCOPE and retrieve biochemical and structural parameters of the vegetation (*e.g.* pigment concentration, canopy structure), and simulate emitted F_{760}. On the other hand, in a very recent study, Verhoef, Van Der Tol, and Middleton (2017) proposed a method to invert coupled RT models of the soil-leaf-canopy and the surface-atmosphere systems to retrieve the full spectrum of emitted F along with important canopy level biophysical parameters that may help its interpretation from top of atmosphere FLEX-S3 data. Nevertheless, such approach has never been tested on measured RS data.

All together, the aspects introduced in the paragraphs above drive the interest in i) retrieving both F_R and F_{FR} (and potentially the full spectrum) starting from high resolution measured RS data, and ii) discriminating the physiological information in the remotely sensed F signal from the contribution given by biophysical, biochemical and environmental parameters. The first step implies the use of high performing spectrometers covering at very high spectral resolution both the red and the far-red spectral regions (cfr. Cogliati et al. 2015; Julitta et al. 2016) while to fulfill the second, the use of a modeling strategy to account for PAR absorption and F reabsorption inside the canopy is mandatory. These aspects have been explored in this thesis and are discussed in Chapters 2,3 and 4.

1.1 OBJECTIVES

The main aim of this research was to exploit multi-source remotely sensed data to improve vegetation status analysis. In particular, I focused on using F, and F-derived metrics, in the red and far-red spectral regions together with hyperspectral reflectance in the VNIR spectral region, as a tool for monitoring variation in the photosynthetic efficiency of plants in different conditions.

The specific research questions of this thesis are:

- to understand if F and F-derived metrics retrieved in the red and far-red spectral regions from high spatial and spectral resolution data acquired with the HyPlant airborne sensor (Rascher et al., 2015), can be used to track changes in plant physiology associated with age-related hydraulic limitation (Chapter 2);
- to explore the capacity of passive measurements of F, together with complementary remote sensing parameters, to detect short-term dynamics of photosynthetic efficiency in vegetation, induced by manipulated stress (Chapter 3);
- to test the direct inversion of a physically based RTM to retrieve Φ_F, the full spectrum of F and several biochemical and structural vegetation parameters, starting from very high resolution field spectroscopy measurements (Chapter 4).

1.2 THESIS OUTLINE

This Ph.D. thesis is structured as a collection of scientific papers, where each chapter is an article with its own introduction, material and methods, results, dis-

cussions and conclusions. The scientific activity of this Ph.D. project has been mainly based on data collected during the measurements campaigns supporting the future FLEX mission of the ESA. The analyses presented here refer in particular to data acquired in 2013 and 2014.

In Chapter 2, I present the activity conducted on data acquired in 2013 over a managed loblolly pine (*Pinus taeda* L.) forest in North Carolina (USA), aimed at investigating the relationship between stand age-related processes and remotely sensed F. I used data collected with the HyPlant airborne sensor to retrieve F_R, F_{FR} and hyperspectral reflectance over the forest with a high spatial resolution (1 m × 1 m). I characterized the F emission of 18 evenly aged stands in a range from 3 to 46 years old, and I computed the corresponding F yields, dividing F by the APAR derived by the reflectance data. Following the concept of a space-for-time substitution, I compared the age-related changes of F and F yields with the correspondent variation in hydraulic limitation (Drake et al., 2010).

In Chapter 3, I present the outcomes of a campaign held in 2014 in Latisana (Udine, Italy) where three 9 m × 12 m plots of a homogeneous lawn were treated with different doses of Dicuran 700 FW (Syngenta AG), a commercial formulation of Chlortoluron (3-(3-chloro-p-tolyl)-1,1-dimethylurea). This herbicide inhibits photosynthesis by blocking the electron transport chain in the photosynthetic apparatus. In particular, it displaces the plastoquinone (PQ) at the QB binding site on the D1 protein and thereby blocks electron flow from QA to QB. I exploited data collected on the ground with very high resolution spectroradiometers, airborne images collected with the HyPlant and the TASI-600 sensors, as well as canopy-level gas exchange measurements collected with closed chambers, in order to detect short-term dynamics of photosynthetic efficiency in vegetation, induced by stress.

In Chapter 4, starting from the ground level top-of-canopy hyperspectral measurements from Chapter 3, I inverted numerically a simplified version of the SCOPE model (van der Tol et al., 2009) to concurrently retrieve F, Φ_F and several biochemical and biophysical parameters of the vegetation from very high resolution apparent reflectance data. In a second step, I used these retrieved values to recognize dynamic patterns of stress adaptation and stress recovery in the plants.

Chapter 5, concludes this thesis with conclusions, discussion of the main findings and suggestions for future work.

2 VARIABILITY OF SOLAR-INDUCED CHLOROPHYLL FLUORESCENCE ACCORDING TO STAND AGE-RELATED PROCESSES IN A MANAGED LOBLOLLY PINE FOREST

ABSTRACT

[1] Leaf fluorescence can be used to track plant development and stress, and is considered the most direct measurement of photosynthetic activity available from remote sensing techniques. Red and far-red solar induced chlorophyll a fluorescence (F) maps were generated from high spatial resolution images collected with the HyPlant airborne spectrometer over even aged loblolly pine plantations in North Carolina (USA). Canopy fluorescence yield (Fy; *i.e.*, the fluorescence flux normalized by the light absorbed) in the red and far-red peaks was computed. This quantifies the fluorescence emission efficiencies that is more directly linked to canopy function compared to F radiances. Fluorescence fluxes and yields were investigated in relation to tree age to infer new insights on the potential of those measurements in better describing ecosystem processes. The results showed that red fluorescence yield varies with stand age. Young stands exhibited a nearly 2-fold higher red fluorescence yield than mature forest plantations, while the far-red fluorescence yield remained constant. We interpreted this finding in a context of photosynthetic stomatal limitation in aging loblolly pine stands. Current and future satellite missions provide global datasets of F at coarse spatial resolution, resulting in intra-pixel mixture effects, which could be a confounding factor for fluorescence signal interpretation. In order to mitigate this effect, we propose a surrogate of the fluorescence yield, namely the Canopy Cover Fluorescence Index

1 The content of this chapter has been accepted for publication in *Global Change Biology* as Colombo, R., Celesti, M., Bianchi, R., Campbell, P.K.E., Cogliati, S., Cook, B., Corp, L.A., Damm, A., Domec, J.-C., Guanter, L., Julitta, T., Middleton, E.M., Noormets, A., Panigada, C., Pinto, F., Rascher, U., Rossini, M., Schickling, A. "Variability of solar-induced chlorophyll fluorescence according to stand age-related processes in a managed loblolly pine forest", and it is currently in press.

(CCFI) that takes into account the spatial variability of canopy structure by exploiting the vegetation fractional cover. Airborne data were degraded at different spatial resolutions and the fluorescence yields were re-computed and evaluated in relation to tree age. It was found that spatial aggregation tended to mask the effective relationships, while the CCFI was still able to identify this link. This study is a first attempt in interpreting the fluorescence variability in aging forest stands and it may open new perspectives in understanding long-term forest dynamics in response to future climatic conditions from remote sensing of F.

2.1 INTRODUCTION

Leaf structure and physiology change in many woody species when they become sexually mature (*e.g.*, Greenwood 1995). Compared with the knowledge of senescence processes in annual and biennial plants, relatively little is known about age-related changes in woody perennials (Bond, 2000). Old trees differ from younger trees, both physiologically and morphologically. In general, older trees have lower rates of photosynthesis, reduced growth rates (both height and diameter) and a distinctive hydraulic architecture (Meinzer, Lachenbruch, and Dawson, 2011; Ryan and Yoder, 1997). Nutrition, carbon allocation (including respiration), meristematic activity and the tree's hydraulic properties all potentially change with tree age and in most cases result in a slower growth in older trees Domec and Gartner (2003). Moreover, it is generally known that photosynthetic rates of seedlings are higher than in mature trees (Larcher, 1969). Leaf photosynthesis and stand primary production have often been found to decline with increasing plant age and size, as a result of hydraulic or biochemical limitations (Drake et al., 2011; Hubbard, Bond, and Ryan, 1999; Ryan, Phillips, and Bond, 2006; Yoder et al., 1994). Determining why growth is reduced in aging forest stands is a compelling need: the growth patterns are pronounced and predictable but the underlying mechanisms remain unclear (Gower, McMurtrie, and Murty, 1996; Ryan, Binkley, and Fownes, 1997). Even though some work has been done at the leaf level (Beeck et al., 2010; Linkosalo et al., 2014; Reinhardt, Johnson, and Smith, 2009; Shirke, 2001), the response of chlorophyll a fluorescence (F) to these age-related processes has not been investigated previously. F is closely related to actual photosynthetic rates and basically to the functional process linked to the amount of energy (in form of transported electrons) that is provided from photosynthetic light reactions Porcar-Castell et al. (2014).

Remote sensing of F is a research field of growing interest with the potential to provide an improved tool for monitoring plant status and photosynthetic function from above. In this framework, the new satellite mission of the European

Space Agency (ESA), the FLuorescence EXplorer (FLEX) (Drusch et al., 2017), is expected to map canopy fluorescence from space at global level, with 300 m spatial resolution, which will be used to derive the photosynthetic activity of natural and managed ecosystems. Fluorescence is considered the most direct proxy of actual photosynthetic activity available from remote sensing techniques and as such it has been used extensively to track plant status at leaf and canopy level (Ač et al., 2015; Cheng et al., 2013; Damm et al., 2010; Daumard et al., 2010; Goulas et al., 2017; Joiner et al., 2014; Koffi et al., 2015; Meroni and Colombo, 2006; Meroni et al., 2008; Middleton et al., 2012; Moya et al., 2004; Rascher et al., 2009; Rossini et al., 2015; Rossini et al., 2010; Zarco-Tejada, González-Dugo, and Fereres, 2016; Zarco-Tejada, González-Dugo, and Berni, 2012; Zhang et al., 2014). The intensity of the fluorescence signal at canopy level depends on the photosynthetic rates, biophysical, biochemical and structural characteristics of the canopy, incoming radiation and background contributions (Cerovic et al., 1996; Damm et al., 2015a,b; Daumard et al., 2010; Fournier et al., 2012; Hoge, Swift, and Yungel, 1983; Moya et al., 2006; Olioso, Méthy, and Lacaze, 1992; Rossini et al., 2016; Van Wittenberghe et al., 2013; Verrelst et al., 2015). These parameters are highly variable in space and time and they should all be considered to correctly interpret the fluorescence signal. In fact, plants with different photosynthetic rates, chlorophyll content and/or canopy structure and exposed to various irradiance regimes can potentially emit the same amount of fluorescence. The effects of variable incoming illumination can be corrected by computing the apparent fluorescence yield (Fy^*) (*i.e.*, the ratio of the emitted fluorescence flux to the total incoming Photosynthetically Active Radiation (PAR)), which is in fact the parameter most commonly exploited for spatial and temporal comparison of fluorescence satellite derived products collected in different light illumination conditions (*i.e.*, different solar zenith angles, *e.g.*, Guanter et al. 2014). However, to move towards the use of F for net photosynthesis and plant functioning characterization in a heterogeneous landscape it is also necessary to account for vegetation structural/biochemical variations. This can be accomplished by exploiting the canopy fluorescence yield (Fy) (*i.e.*, the ratio of the emitted fluorescence flux to the Absorbed Photosynthetically Active Radiation (APAR)), which is a physically-based index of efficiency that accurately describes the effects of the absorbed radiation on the F signal. The usefulness of F or Fy^* to track the effects of environmental stressors on plant functioning has been demonstrated in numerous investigations (*e.g.*, Guanter et al. 2014; Meroni et al. 2008) while the performances of Fy computed at airborne or satellite level has been investigated in only two studies (Introna and Wood, 2004; Wieneke et al., 2016). This is mainly due to the difficulty in accurately estimating APAR.

Current and future satellite missions will provide global datasets of F at a range of coarse spatial resolutions (*e.g.*, 300 m to 0.5°), resulting in intra-pixel mixture

effects, which will be an unavoidable confounding factor for fluorescence signal interpretation. In this context, there is a need of having simplified F-derived indices for small-scale applications over large regions, which can take into account the spatial variability of canopy structure. Therefore, a new approach is needed to compensate for structural effects on F measurements, including the use of radiative transfer model inversion (Hernández-Clemente et al., 2017; van der Tol et al., 2016; Zhao et al., 2016), spectrally invariant correction factors (*e.g.*, the Directional Area Scattering Factor (DASF), Knyazikhin et al. 2013), or empirical normalization techniques (Colombo, Meroni, and Rossini, 2016).

In this paper, red (F_{690}) and far-red F (F_{740}) maps were generated from high spatial resolution images (1 m) collected with the HyPlant airborne sensor over a range of even aged stands in loblolly pine forest plantations in North Carolina (USA). The canopy fluorescence yields for both red (Fy^{690}) and far-red F (Fy^{740}) were then computed and investigated with the main aim to understand if F varies across stands of different ages, according to structural and physiological parameters. In this context, we hypothesized that hydraulic limitation in older pines could reflect in a lower fluorescence emission compared to the younger trees, due to the reduced rates of photosynthesis. We were also interested in evaluating the effect of pixel size, and the mixture effects, on the relationships between fluorescence and stand age. This study can be considered a first attempt in interpreting the fluorescence variability in aging forest stands and it may open new perspectives in understanding long-term forest dynamics from remote sensing of F.

2.2 DATA AND METHODS

2.2.1 Study area

This study was performed at the Parker Tract forest in the lower coastal plain near Plymouth, North Carolina, USA, in the context of the joint 2013 ESA/NASA FLEX airborne campaign (Middleton et al., 2017). The forest is a 4400 ha managed plantation that contains various loblolly pine (*Pinus taeda* L.) stands of different ages. Parker Tract is a pine forest where stand density is reduced under a prescribed thinning regime as age increases to maximize timber production. According to the Parker Tract forest management plan, pine stand age within the study area ranges from 3 to 46 years old, when the forest have reached high commercial potential and is being harvested. Therefore, we are dealing with juvenile and mature stages. The topography is flat and the climate is maritime temperate zone with a mean annual precipitation of 1320 mm and mean annual temperature is of 15.5 °C. The Parker Tract forest belongs to the Long-Term Ecological Research

Sites and further details on the site are reported in different studies (*e.g.*, Domec et al. 2012; Noormets et al. 2010). Figure 3 shows the location of the study area and the investigated loblolly pine stands (with their plantation age) overlapped to the HyPlant mosaic of airborne images collected over the investigated forest. The tree age classes reported in Figure 3 correspond to years since planting at the time of data acquisition. In particular, tree ages correspond to the time when the sites were graded and planted with 2 years-old seedlings, and thus can be considered a chronosequence. Since no direct dendrochonological and only few physiological measurements were available for comparison between forest data and fluorescence estimates, to better interpret our findings we also exploited data and previous results obtained in a companion loblolly forest at the Duke Forest. The Duke Forest loblolly study area, is located in the Blackwood Division of Duke Forest (US-Dk3; lat/lon 35.9782° / −79.0942°, North Carolina, USA). It represents a late stage post-agricultural succession characteristic of the south-eastern United States. Duke Forest, in addition to mixed deciduous forest, also has even-aged plantation of loblolly pine stands ranging from 14 to 114 years, established in 1983 following a clear cut and a burn (Domec et al., 2015; Novick et al., 2009; Oren et al., 2006).

2.2.2 Field campaign and leaf level measurements

During the field survey in September and October 2013, forest stands characteristics including number of species, average tree height, crown width, crown depth, and tree diameter at breast height (1.3 m) were measured within one-tenth of an acre (0.4 ha) plots and averaging measurements from 2–3 plots per stand, at both Parker Tract (18 stands) and Duke Forest (14 stands). Leaf Area Index (LAI) was measured at all stands using a LAI-2000 Plant Canopy Analyzer (LAI-2000 PCA; Li-Cor, Lincoln, NE, USA). LAI measurements at each location were taken using a standard protocol in diffuse light conditions within one hour of dawn or dusk.

Average carbon (%C) and nitrogen concentration (%N) for pine foliar samples were measured in 26 stands (18 at Duke Forest and 8 at Parker Tract), while leaf chlorophyll content was estimated at 16 stands at Parker Tract. Leaf samples were collected from the 2 most recent annual leaf flushes on 1–3 branches of the sunlit portion of the upper canopy of three pine trees in a stand, using a cherry picker or a rifle. The branch samples were placed in a bag with wet paper towel, on ice, in a dark cooler and taken to a nearby field lab for analysis. Leaf fresh and dry weights were measured on 10 needle fascicles from a sample, using three samples per tree. For pigment determination, needle samples were ground and placed in polystyrene cuvettes containing 4 ml dimethyl sulfoxide (DMSO) and frozen for

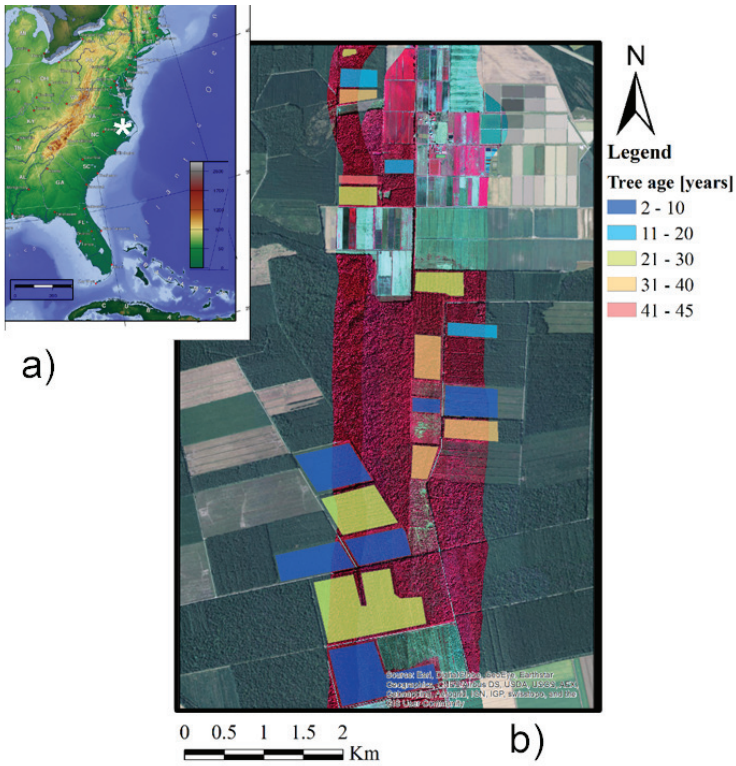

Figure 3: a) Location of the Parker Tract Forest in NC, USA; b) Location of the Loblolly pine even aged stands (18 total) are shown in colored categories, overlapped on a false color composite HyPlant mosaic.

extraction before the measurements. A spectrophotometer was used to determine chlorophyll a, chlorophyll b, total chlorophyll (Cab, $mg\,cm^{-2}$), and carotenoids based on established equations (Chappelle, Kim, and McMurtrey, 1992). Leaf reflectance and transmittance spectra were also measured on needles collected from 25 trees (1-2 trees per stand at Parker Tract), at the end of the growing season, when the needles were fully developed. Hemispherical reflectance and transmittance were measured using an ASD spectrometer (FieldSpec 3, Analytical Spectral Devices, Inc., Bolder Co.) equipped with an external integrating sphere (LI-1800, Li-Cor, Lincoln, NE, USA) and then used to determine fraction of Absorbed Photosynthetically Active Radiation (fAPAR) at leaf level. The needles were arranged side by side following the methodology introduced by Daughtry, Biehl, and Ranson (1989) ("Case 3") as described in Williams (1991). Leaf level stomatal conductance (g_s) and net photosynthesis (P_{net}) measurements at the Parker Tract forest were performed on 17th May 2013, and 30th September 2013 for the mature pine trees (23 years old trees) and on 2nd June 2013 and 1st October 2013 for the young trees (7 years old trees). Meteorological conditions were stable during those weeks and were characterized by clear and warm days. g_s and P_{net} were measured with a LI-6400 gas exchange system (LI-COR, Lincoln, NE, USA). Measurements of g_s were performed on six randomly selected individuals within each age class every two hours beginning at 6:00 h solar time and ending at approximately 15:00 h solar time. Measurements of g_s were conducted on current-year detached fascicles taken from the same shoot simultaneously, and were performed on fully sun exposed south-facing shoots. For the mature trees, shoots from the upper canopy were shot down with a rifle. Needles were not detached for more than five minutes before the measurements were initiated. Previous studies on the same tree species have shown that there were no differences between excised and attached needle gas exchange when measurements were restricted to less than 15 minutes after excision (Drake et al., 2010; Maier et al., 2002). For each needle, the chamber was set to match prevailing environmental conditions assessed immediately prior to the measurement: atmospheric CO_2 concentration (384–405 ppm), relative humidity (46–61 %), photosynthetically active radiation (600–1800 $\mu mol\,m^{-2}\,s^{-1}$), and leaf temperature (27–35 °C). Stomatal conductance and photosynthesis data reported here correspond to the maximum values, *i.e.*, usually taken between 09:30 h and 11:30 h solar time. For normalizing g_s on an all-sided leaf area basis, needle areas were obtained geometrically from dimensions measured using a digital caliper (series 500 Mitutoyo, Aurora, IL, USA) (Rundel and Yoder, 1998)). Along with the gas exchange measurements, leaf water potential (Ψ_{leaf}) were measured at predawn and at midday (11:00 h - 12:00 h solar time) using a pressure chamber (PMS Ins., Albany, OR, USA). For the midday measurements, Ψ_{leaf}, g_s and P_{net} were conducted on detached fascicles taken from the same shoot.

2.2.3 Airborne acquisition and pre-processing

On 26th October 2013, from 09:56 h to 11:08 h solar time, eight aerial images were acquired by the HyPlant airborne imaging spectrometer on board the National Aeronautics and Space Administration (NASA) Langley Research Center's (LARC) UC12 Beechcraft King Air in combination with imagery acquired by the Goddard LiDAR, Hyperspectral and Thermal (G-LiHT) airborne system. Extensive descriptions of these systems are presented in Cook et al. (2013), Middleton et al. (2017), and Rascher et al. (2015). The HyPlant Instantaneous Field Of View (IFOV) is equal to 0.0832°, while the Field Of View (FOV) is of 32.3°. With such a configuration, the aircraft was flown at an average altitude of 610 m, resulting in a HyPlant swath of 384 m, with a spatial pixel size of 1 m. HyPlant system consists of two modules: the broad band dual-channel module (DUAL) to compute surface reflectance in the visible through near and short wave infrared spectral region (380–2500 nm) and the fluorescence module (FLUO) which operates at higher spectral resolution in the 670–780 nm spectral range designed for fluorescence retrievals. HyPlant at-sensor radiance images from the FLUO and the DUAL modules were generated through a dedicated processing chain. The Atmospheric & Topographic Correction model (ATCOR, ReSe Applications Schläpfer) was run to perform the atmospheric correction and then all the images were georectified using the CaliGeo toolbox (SPECIM, Finland). In addition to reflectance and fluorescence, spectral vegetation indices were generated using the Hyplant data. An example of radiance measurements from a loblolly pine acquired with the FLUO module is shown in Figure 4. A canopy tree height map was obtained from the Light Detection And Ranging (LiDAR) data. Classification of G-LiHT LiDAR ground returns was performed with a progressive morphological filter with Delaunay triangulation to generate a Triangulated Irregular

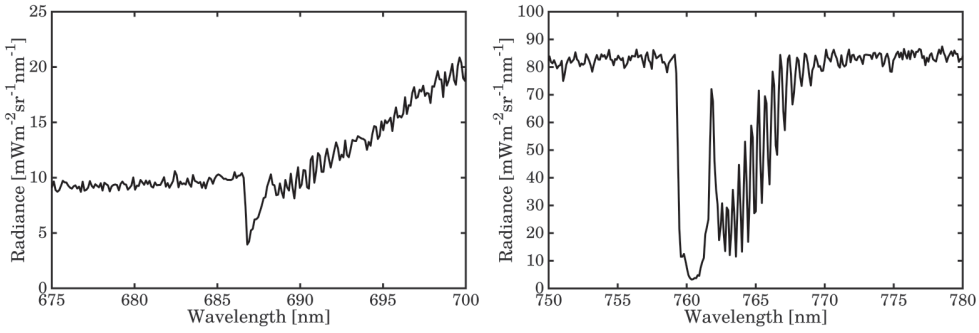

Figure 4: Example of the spectral radiance extracted from the HyPlant image (FLUO module) for a loblolly pine around oxygen B (a) and A (b) absorption bands.

Network (TIN) of ground hits, and the TIN was then used to linearly interpolate the Digital Terrain Model (DTM) on a 1 m raster grid. Additionally, the TIN was used to interpolate the base elevation of every non-ground return, and vegetation heights were computed by difference. The Canopy Height Model (CHM) was created by selecting the greatest return height in every 1 m grid cell. Tree height, defined as the maximum height of each tree, was derived from the CHM by finding the local maximum in a moving window of 3 × 3 pixels (3 × 3 m). Local maxima lower than the 1st quartile of the CHM in the stand were not considered representative of a tree, thus they were neglected. The average tree height for each stand was computed as the average of all tree heights (*i.e.*, the local maxima) within each stand.

2.2.4 Retrieval of Sun-Induced Fluorescence

Among different approaches available for the retrieval of F (*e.g.*, Cogliati et al. 2015), the Singular Vector Decomposition (SVD) (Guanter et al., 2012, 2013) was selected for this study based on successful results with Hyplant data in other studies (*e.g.*, Rossini et al. 2015). This data-driven approach relies on two key assumptions: i) a given radiance spectrum can be modeled as the linear combination of a reflected surface radiance plus a F emission propagated to at-sensor level, and ii) the reflected surface radiance can be formulated as a linear combination of orthogonal spectral vectors. The SVD is comparable to a principal component analysis and reduces the dimensionality of a large set of correlated variables (*e.g.*, training radiance spectra that are free of F emissions) by transforming it into a small set of uncorrelated variables (singular vectors). The definition of a forward model (L) to describe a measured radiance signal including F emissions at sensor level comprises several spectral functions (singular vectors) representing the signal intensity due to surface albedo, illumination angle, atmospheric absorption and scattering effects, spectral slope as a function of surface reflectance, and sensor effects (spectral shifts, band broadening). Further, F radiance ($W\,m^{-2}\,sr^{-1}\,nm^{-1}$) is considered as an additive component to complement the forward model as:

$$L(\omega, F) = \sum_{i=1}^{n_v} \omega_i v_i + F \tag{3}$$

where ω_i corresponds to the weight of a particular singular vector v_i. Typically, 4-5 singular vectors are used to model the at-sensor radiance signal, considering an empirical threshold of 0.05% as minimum information content of a singular vector. Few adjustments were applied to improve the inversion results, such as removing the strongest absorption features since the forward model does not include any

physical formulation of atmospheric absorption or scattering effects, nor the normalization of input radiances and radiances used to obtain the singular vectors based on their spectral slope. The inversion of L was done by means of standard least squares fitting using a retrieval error covariance S_e that is given as:

$$S_e = \delta_m^2 (J^T J)^{-1} \tag{4}$$

where δ_m^2 is the measurement error approximated as standard deviation of a subset of used reference radiance signals and J is the matrix containing the singular vectors and J^T is its transpose. The SVD algorithm was applied to the HyPlant FLUO data to produce maps for the canopy red F radiances at 690 nm and far-red F at 740 nm radiances at the full native HyPlant spatial resolution (1 m).

2.2.5 Retrieval of Absorbed Photosynthetic Active Radiation

The APAR maps were computed as the product of fAPAR and the incoming PAR values. fAPAR can be derived from remote sensing, exploiting either physically based or empirical strategies using spectral vegetation indices (*e.g.*, D'Odorico et al. 2014; Donohue, Roderick, and McVicar 2008; Gobron et al. 2006; Myneni et al. 2002; Pickett-Heaps et al. 2014; Walter-Shea et al. 1997; Widlowski 2010. Following a scheme analogous to Damm et al. (2010), but using the spectral reflectance instead of the incident and reflected radiance, fAPAR was computed in this study as (1-reflectance) in the PAR region (400–700 nm). In addition, for comparison purposes, we also estimated fAPAR as a linear model of the Normalized Difference Vegetation Index (NDVI) (Goward and Huemmrich, 1992; Hatfield, Asrar, and Kanemasu, 1984; Liu, Guan, and Liu, 2017; Myneni and Williams, 1994). The incident PAR was measured at the US-NC2 loblolly plantation flux tower at half-hourly steps, and interpolated to actual overflight times with a piecewise polynomial smoothing spline. During the overpasses (*i.e.*, between 9:56 h and 11:08 h solar time), PAR varied between 1130 $\mu mol\, m^{-2}\, s^{-1}$ and 1430 $\mu mol\, m^{-2}\, s^{-1}$ (247 to 313 $W\, m^{-2}$).

2.2.6 Computation of fluorescence yields of loblolly pine

The F flux can be modeled as the product of PAR, fAPAR and Fy (Eq. 5). The last term is the amount of absorbed radiation emitted as fluorescence (*e.g.*, Lee et al. 2013).

$$F_{[\lambda,t]} = PAR_{[400-700,t]} \times fAPAR_{[\lambda,t]} \times Fy_{[\lambda,t]} \tag{5}$$

The fluorescence flux is dependent on wavelength (λ) and time (t) at which the flux is emitted. Canopy-level fluorescence yield is related to leaf-level fluores-

cence yield, neglecting a second-order term accounting for the reabsorption of the red fluorescence within the canopy and the canopy anisotropy, at both red and far-red wavelengths (Damm et al., 2015b; Guanter et al., 2014). In this study, the computation of the fluorescence yields at full (1 m) spatial resolution was conducted selecting only the loblolly F radiance in each stand. A supervised classification scheme based on the HyPlant DUAL reflectance images was therefore implemented to identify loblolly pine (mainly sunlit pixels). Two hundred training pixels were randomly selected and visually assigned to one of the four spectrally distinguishable classes (*i.e.*, loblolly pine, shadow, bare soil, and other vegetation components). The classified map was used as a mask to extract F and APAR of the loblolly component within 18 different stands identified as Region Of Interest (ROI) of 84 × 84 pixels each. The dimension of the ROI was set according to the forest stand dimensions to get an average stand values of red and far-red F and APAR for the loblolly component (hereafter F_{lob}^{690}, F_{lob}^{740} and $APAR_{lob}$), and the corresponding fluorescence yields (hereafter Fy_{lob}^{690} and Fy_{lob}^{740}). The subscript "lob" indicates the loblolly pine class. The ROIs were selected as close to nadir as possible in order to minimize possible effects dependent on airborne cross-track viewing angles. The Fy maps of the loblolly component were then obtained using Equations 6 and 7, based on values from the maps of loblolly F and APAR.

$$Fy_{lob}^{690} = \frac{F_{lob}^{690}}{APAR_{lob}} \tag{6}$$

$$Fy_{lob}^{740} = \frac{F_{lob}^{740}}{APAR_{lob}} \tag{7}$$

where $APAR_{lob}$is the product of PAR and fAPAR maps of the loblolly pine obtained with the different overpasses. We also tested Fy^{*}, usually employed in remote sensing of fluorescence studies when information about APAR is not available.

2.2.7 Spatial aggregation and definition of the Canopy Cover Fluorescence Index

In the analysis at full resolution, the scheme used in this study was similar to that suggested by Malenovský et al. (2013) and Zarco-Tejada et al. (2004), so that the Fys were mainly extracted from sunlit pixels. The 1 m pixel size allowed the detection of pixels of homogenous vegetation within the stands. HyPlant data were collected in October when the dominant green land cover type was the loblolly pine. Other components, such as understory and deciduous trees, were mainly displaying early autumn senescent foliage, while shadows and bare soils were the

most common classes in older and younger stands, respectively. In these forests, when data are aggregated to even 10 m spatial resolution, these components become mixed and it becomes difficult to find and isolate sunlit loblolly components. To evaluate if the relationships between F and age-related processes are affected by pixel size (surface heterogeneity), a simple spatial-aggregation analysis was carried out by resampling the data at different spatial resolutions (*i.e.*, pixel sizes of 10 × 10, 30 × 30, 60 × 60 and 84 × 84 pixels). The maximum aggregation was fixed at 84 × 84 pixels in order to be consistent with the overall stand size, since larger aggregations would result in including trees with different ages. The output of this process generated maps at different pixel (p) sizes, using aggregated red and far-red fluorescence radiances (F_p^{690}, F_p^{740}), $APAR_p$, red-fluorescence and far-red fluorescence yields ($Fy_p^{690} = F_p^{690} / APAR_p$; $Fy_p^{740} = F_p^{740} / APAR_p$).

We can reasonably assume that the F value of a generic pixel p can be expressed with a linear mixing model driven by vegetation fractional cover (ESA, 2017; Hernández-Clemente et al., 2017; Zarco-Tejada, Suarez, and Gonzalez-Dugo, 2013). In this study, the vegetation fractional cover of the loblolly (fc_{lob}) was computed as the ratio between the number of pixels of the loblolly class divided by total number of pixels in the ROI. For the case having only two components within a pixel, the F flux of the aggregated pixel can be derived from the target component (*i.e.*, in this case F_{lob}^{690}, F_{lob}^{740}), the fluorescence of the other components (oc) within the pixel (F_{oc}^{690}, F_{oc}^{740}), and fc_{lob}. Therefore, the aggregated red F radiance can be estimated as follows:

$$F_p^{690} = F_{lob}^{690} * fc_{lob} + F_{oc}^{690} * (1 - fc_{lob}) \tag{8}$$

The F_{oc}^{690} term in the study area is mainly a combination of senescent vegetation, bare soil and shadows, and we can reasonably consider that such a F flux is almost null or negligible. The F flux of the loblolly component can be therefore directly derived by the aggregated F value and its fractional cover. Using this scheme, we can introduce the Canopy Cover Fluorescence Index (CCFI) that makes use of the loblolly fractional cover within the pixel rather than the typically used fAPAR as the basis for normalizing the F fluxes:

$$CCFI_{690} = \frac{F_p^{690}}{fc_{lob}} \tag{9}$$

This index is considered here to be independent from the spatial variability of land cover proportions within each pixel. In other words, for a single vegetation class discontinuously covering the soil surface, the CCFI approximates Fy_{lob}^{690}, allowing comparisons of F across spatial scales without bias due to the different amounts of vegetation coverage in each pixel.

2.2.8 Statistical analysis

The previously described F-derived metrics were investigated across stands of different ages with data aggregated to different spatial resolutions, by using regression models. Statistical analysis and coding was performed in Matlab R2016a (MathWorks, USA) and IDL 8.2 (Exelis VIS, USA), while image visualization and rendering was done in ENVI 5.2 (Exelis VIS, USA) and QGIS 2.14 (Quantum GIS Development Team, 2016).

2.3 RESULTS

2.3.1 Spatial pattern of forest fluorescence

An example of F maps for three loblolly pine stands characterized by different ages is shown in Figure 5, with the RGB reflectance map from the HyPlant DUAL and the CHM derived from the G-LiHT LiDAR data. The different proportions of shadow and sunlit canopy, as well as the spatial arrangement of the sunlit and shadowed components, are clearly distinguishable in the three stands. In particular, in the younger stands the row-structured pattern followed for plantation is clear, while in the oldest stand canopy closure obscures the planting arrangement. F maps show similar spatial patterns, with lower values in bare or shadowed areas and higher values in the sunlit portion of the canopy. The inter-crown gap pattern in the younger stands is clearly visible both in red and far-red F maps. Fluorescence at 690 nm and 740 nm for loblolly pine class ranged between 0.2 and 0.8 $mW\,m^{-2}\,sr^{-1}\,nm^{-1}$ and between 0.3 and 1.2 $mW\,m^{-2}\,sr^{-1}\,nm^{-1}$, respectively. Non-fluorescent targets (*e.g.*, the roads between the stands) showed F values close to zero, indicating the reliability of the F maps. Overall, the F emission magnitude of loblolly pine is relatively low compared to dense deciduous forests, as reported in previous studies (Rossini et al., 2016) and the values compare well with F ground observations obtained over similar loblolly pine stands (ESA, 2015).

2.3.2 Reflectance measurements and fAPAR maps

Reflectance and transmittance measurements of loblolly pine needles allowed the computation of the average leaf fAPAR, (Figure 6). The proportion of reflected PAR was approximately 8% and the transmitted PAR was $\approx$ 3%, while the remaining fraction of the total incoming PAR was absorbed (fAPAR = 0.89 or 89%; standard deviation = 0.021). Since at individual leaf level, only about 3%

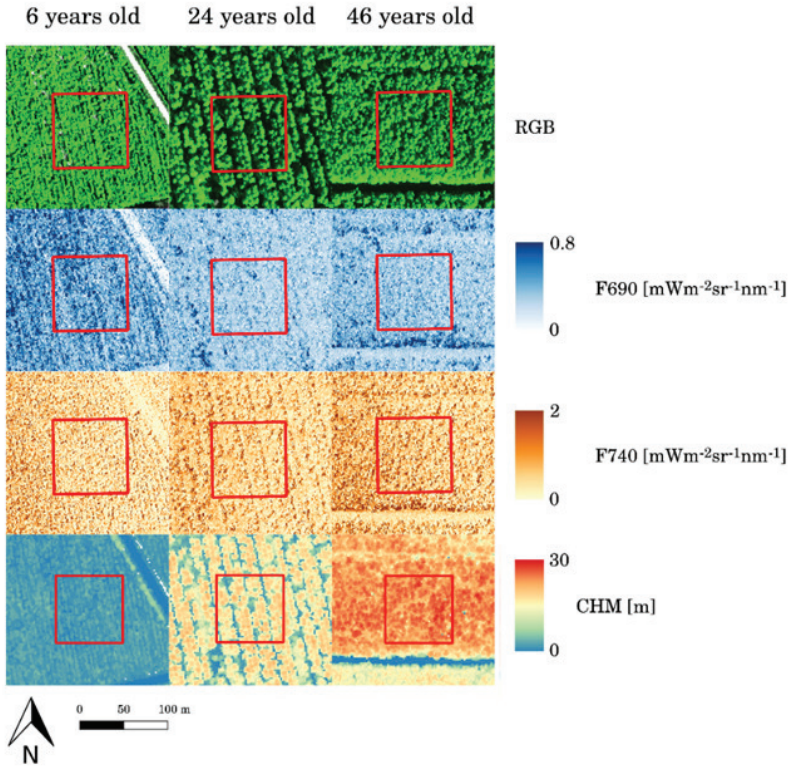

Figure 5: Example of three loblolly pine stands characterized by different ages and heights (left to right: 6, 24 and 46 years old). From top to bottom: RGB color composite from the HyPlant DUAL, F at 690 nm and 740 nm from the HyPlant FLUO, and canopy height map from the G-LiHT LiDAR. The red squares are the 84 × 84 pixels ROI selected for each forest stand.

of PAR is transmitted (but subsequently potentially absorbed by other leaves) we are confident that the approach used in this study to generate fAPAR maps may only slightly overestimate canopy fAPAR, and therefore potentially underestimate fluorescence yield. The strong correlation between the two estimates of fAPAR (R^2= 0.67, Root Mean Squared Error (RMSE) = 0.05, $p < 0.001$) using the methods previously presented, increases the confidence in our results.

2.3.3 Structural, biophysical, biochemical parameters and leaf gas exchanges

The relationship between tree age and canopy height derived from the G-LiHT LiDAR data at Parker Tract was compared with that measured at the Duke Forest by (Drake et al., 2010) for pines. A very similar relationship between tree height and age was found (Figure 7), suggesting that stands at both forests may belong to the same Site Index (SI) and could present similar aging patterns. At the Duke Forest, canopy height ranged from 14 to 43 m, while at the Parker Tract forest tree height varied from 1 to 26 m. Figure 7 shows the relationship between tree age and height for the full dataset including stands from both Parker Tract and Duke Forest modeled using the Gompertz equation (Brook, Traill, and Bradshaw, 2006).

Table 1 and Figure 8 show the relationships between stand age and height (in brackets) with the biophysical and biochemical parameters measured in field and laboratory. These results clearly show that there were no significant relationships between these variables.

The leaf level stomatal conductance (mean and standard error of 6 trees) of young trees was found 82.1 (6.4) / 58.2 (5.8) $\mu mol\, m^{-2}\, s^{-1}$ in June / September, respectively, while for mature trees it was 61.2 (5.7) / 49.5 (4.2) $\mu mol\, m^{-2}\, s^{-1}$ in June / September, respectively. p values for both dates between mature and young trees were < 0.01. Similarly, P_{net} of young and mature trees measured in June were

Table 1: Coefficient of determination (R^2) and p-value of the linear relationships between stand age (and height) versus vegetation variables: total chlorophyll content (Cab), Leaf Area Index (LAI), carbon (C) and nitrogen (N) concentration.

Relationship	R^2	p-value
Age (height) vs chlorophyll a+b content (C_{ab})	0.01 (0.01)	0.68 (0.68)
Age (height) vs LAI	0.13 (0.13)	0.06 (0.04)
Age (height) vs %C	0.05 (0.06)	0.26 (0.22)
Age (height) vs %N	0.03 (0.03)	0.42 (0.39)

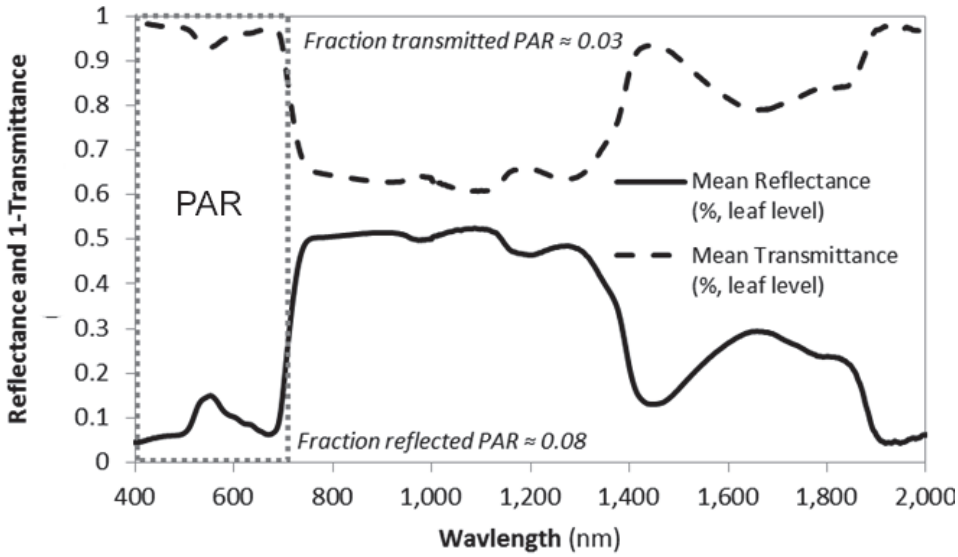

Figure 6: Loblolly pine leaf optical properties (mean reflectance and transmittance).

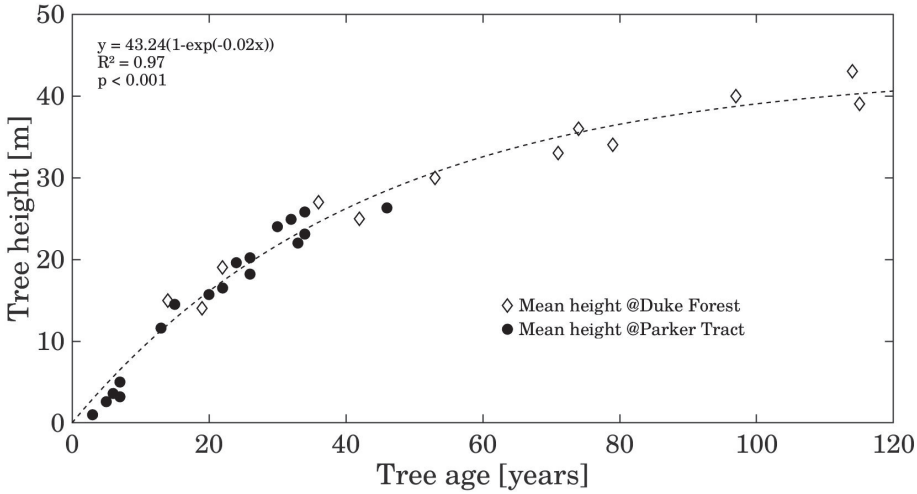

Figure 7: Relationship between tree height and age at Parker Tract (closed symbols) and Duke Forest (open symbols, Drake *et al.*, 2010) (R^2= 0.97).

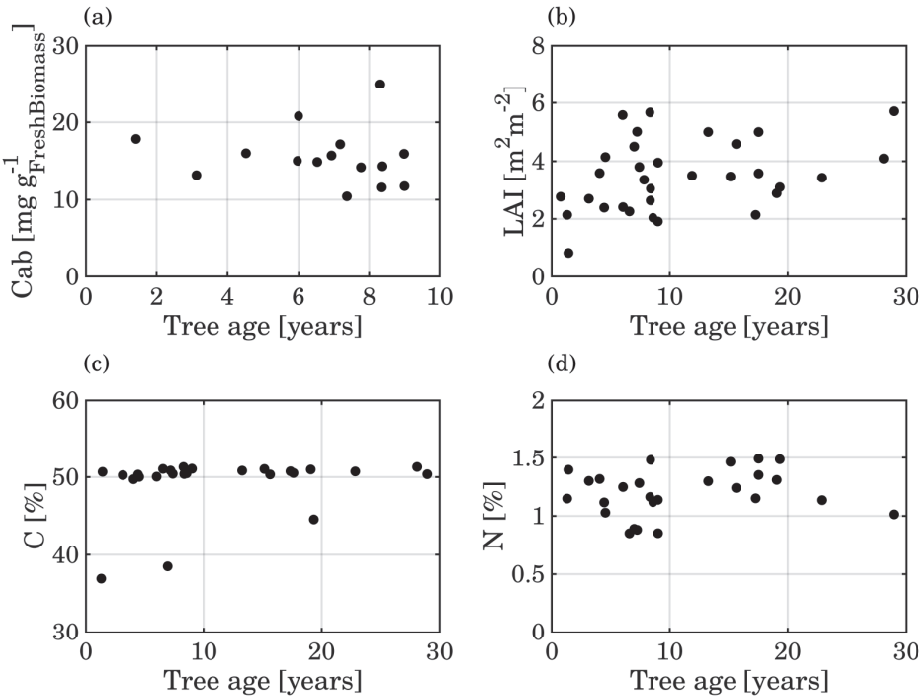

Figure 8: Scatter plot between loblolly tree age and total Cab (a), LAI (b), C (c) and N (d).

7.0 (0.5) and 5.8 (0.6) $\mu mol\, m^{-2}\, s^{-1}$, respectively, and in September were 5.7 (0.7) and 3.8 (0.6) $\mu mol\, m^{-2}\, s^{-1}$, respectively (p values for both dates for P_{net} between mature and young trees were < 0.01). Across stand age, the reduction in P_{net} was highly correlated with the decline in g_s ($P_{net} = 0.089 \times g_s$; $R^2 = 0.84$; with g_s in $mmol\, m^{-2}\, s^{-1}$ and P_{net} in $\mu mol\, m^{-2}\, s^{-1}$). Water stress had a larger effect on P_{net} in old trees than in young trees, even though old trees had similar ($p = 0.42$) predawn water potentials in June and even higher ($p < 0.001$) ones (less negative) in September than young trees (data not shown). The decline in P_{net} between June and September was indeed 18.6% in young trees and 34.5% in mature trees.

2.3.4 Relationship between loblolly fluorescence, APAR, fluorescence yield and tree age

The relationship between loblolly fluorescence (F_{lob}) and tree age obtained at Parker Tract is shown in Figure 9. F_{lob} was derived by HyPlant data at full spatial resolution, while stand age was derived from the Parker Tract management plan (n = 18 stands). Both, F_{lob}^{690} and F_{lob}^{740} show some variability among stands but only F_{lob}^{690} exhibits a statistically significant relationship with tree age. In the case of red-fluorescence, a nonlinear decline shows that young forest stands emit slightly more red fluorescence compared to older trees (Fig. 9a). Overall, we tested different models and we found that the exponential model described the data best, producing the largest coefficient of determination. loblolly APAR shows instead a subtle change with age (Figure 10), with younger stands that absorb less PAR radiation than older canopies. Although there is a link between APAR and F, the latter typically shows an additional response to plant physiology and quickly varies with changing photosynthetic activity even before any variation in the pigment pool occurs (*e.g.*, Rossini et al. 2015). Hence, the relationship between F and APAR is not univocal, and they provide complementary information on different aspects of the photosynthetic process.

The relationships between the red F yield and tree age is shown in Figure 11. The nonlinear decrease in Fy_{lob}^{690} with age is more pronounced and clearer than for F, while there is still no relationship for the far-red F yield (Fy_{lob}^{740}). Fy_{lob}^{690} performed better than Fy^{*690}_{lob}, which was less related to stand age, with results similar to that found for F_{lob}^{690} ($R^2 = 0.41$, data not shown). Overall, young stands exhibiting Fy_{lob}^{690} up to 90% higher than older trees (*e.g.*, 3.8 *vs.* 2.2 $sr^{-1}\, nm^{-1}$).

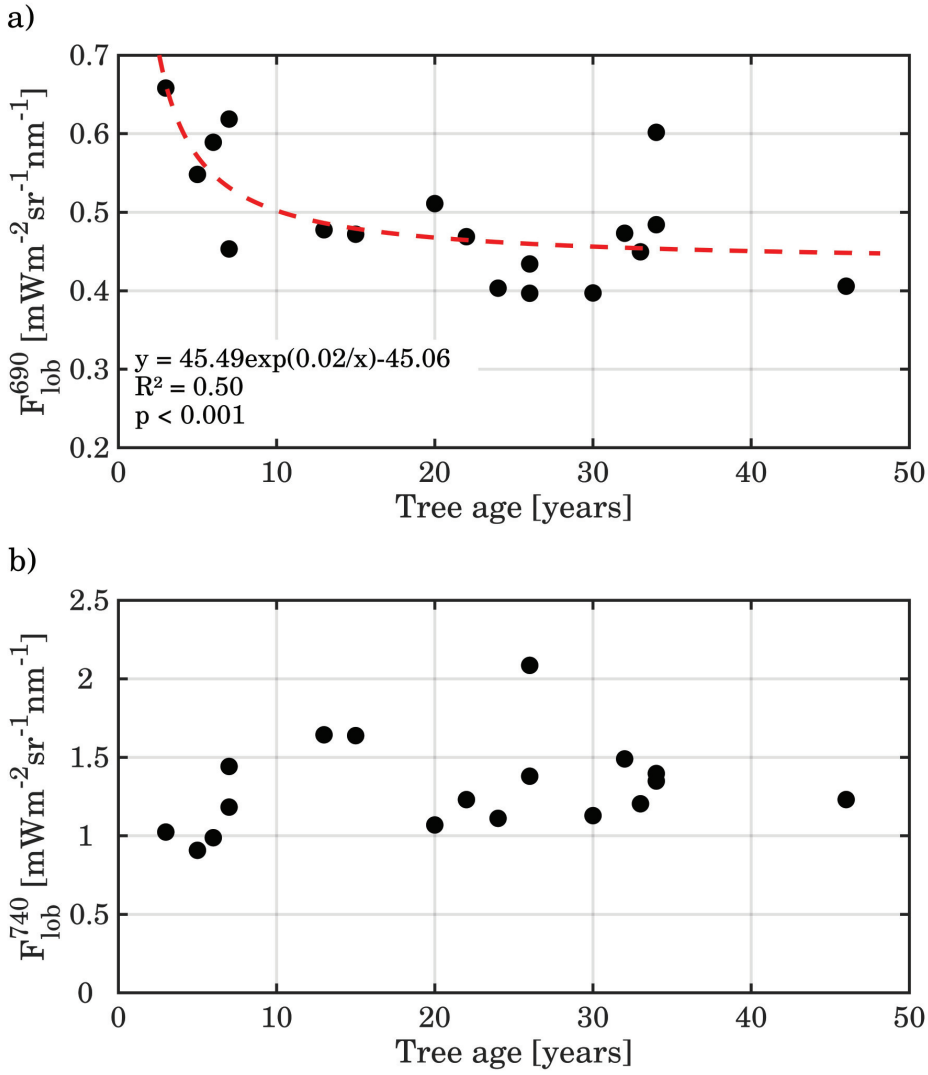

Figure 9: Mean F radiance values (at 690 nm and 740 nm) for the loblolly component, extracted as the average value of the loblolly class in each ROI, and plotted *vs.* tree age. The far-red F radiance is relatively constant so that the F *vs.* tree age relationship is not statistically significant.

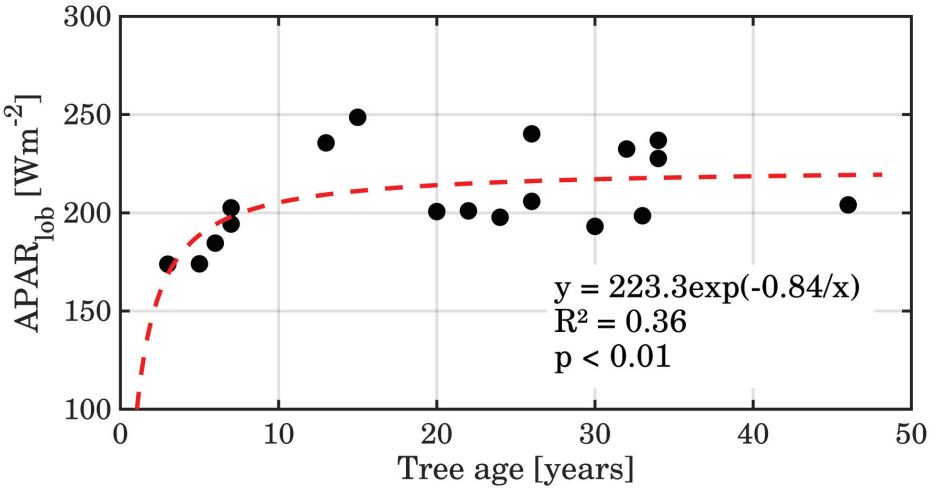

Figure 10: Loblolly APAR values *vs.* tree age for the 18 ROIs.

2.3.5 Impact of spatial aggregation on F-tree age relationships and performances of the Canopy Cover Fluorescence Index

The relationships between spatially aggregated (84 m × 84 m) F_{lob}^{690} and Fy_{lob}^{690} versus stand age are shown in Figure 12. In this case, aggregated pixels are implicitly composed of mixtures of different components. Although it is still possible to observe a slight linear decline of both F_p^{690} and Fy_p^{690} with age, at this coarser spatial resolution this relationship cannot be easily revealed. Similarly, diminishing success for results (in terms of coefficient of determination and significance of the regression) were also found when aggregating at 10 m × 10 m, 30 m × 30 m, 60 m × 60 m spatial resolutions (R^2= 0.30; R^2= 0.27; R^2= 0.25, respectively). We underscore that aggregated pixels never resulted in mixed stands with different ages. Such analysis is beyond the scope of this study. In addition, no statistically significant relationships were found between either $APAR_p$ and stand age or F_p^{740} at different aggregation levels (data not shown). Figure 13a shows the relationship between the fractional cover of the loblolly pine stands and the spatially aggregated red F (84m × 84 m) and indicates that fluorescence is fairly affected by this parameter. The F signal at this spatial resolution is in fact a mixture of the fluorescence fluxes emitted by tree crowns, both sunlit and shadowed, and understory, with different proportions of bare soils and canopy gaps, which causes a variability in the emitted fluorescence flux over stands with different vegetation cover. Moreover, we also tested the relationship between loblolly fractional

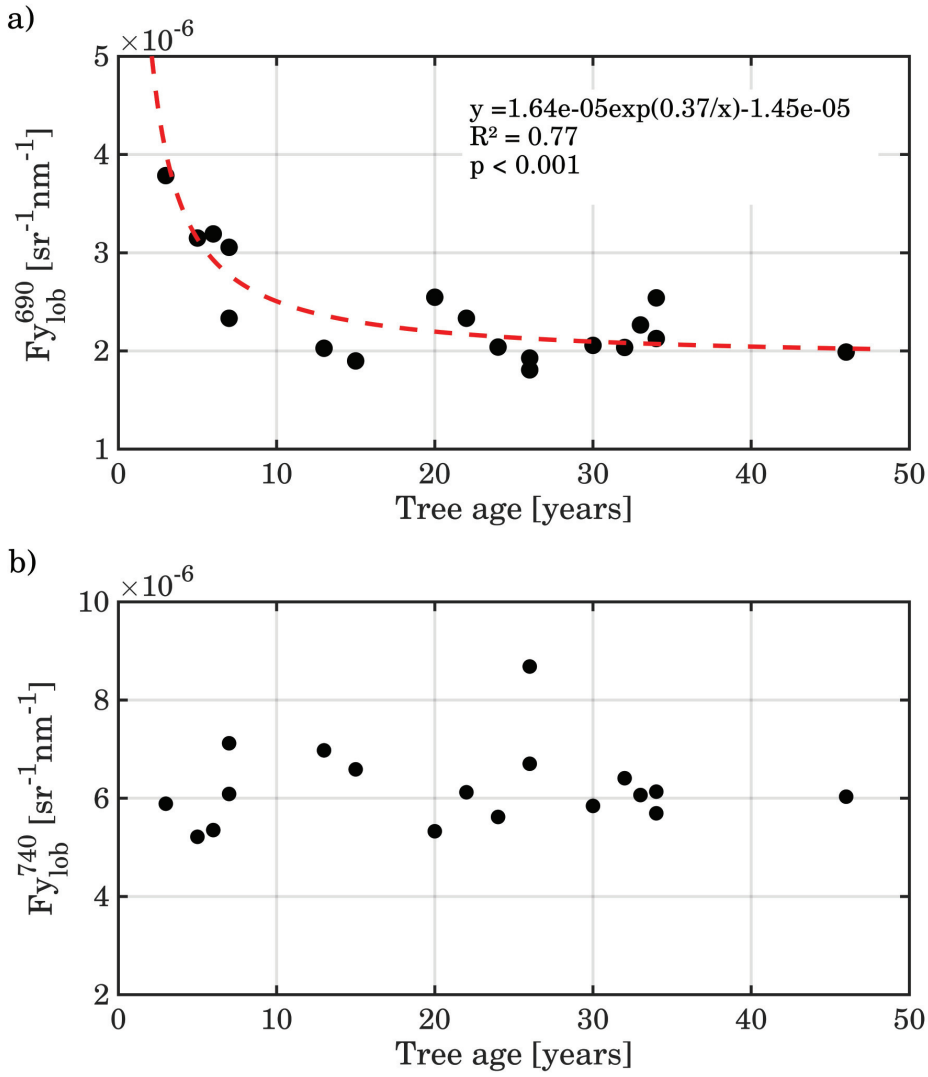

Figure 11: Red and far-red F yields for loblolly pine *vs.* tree age for observations acquired at 1 m.

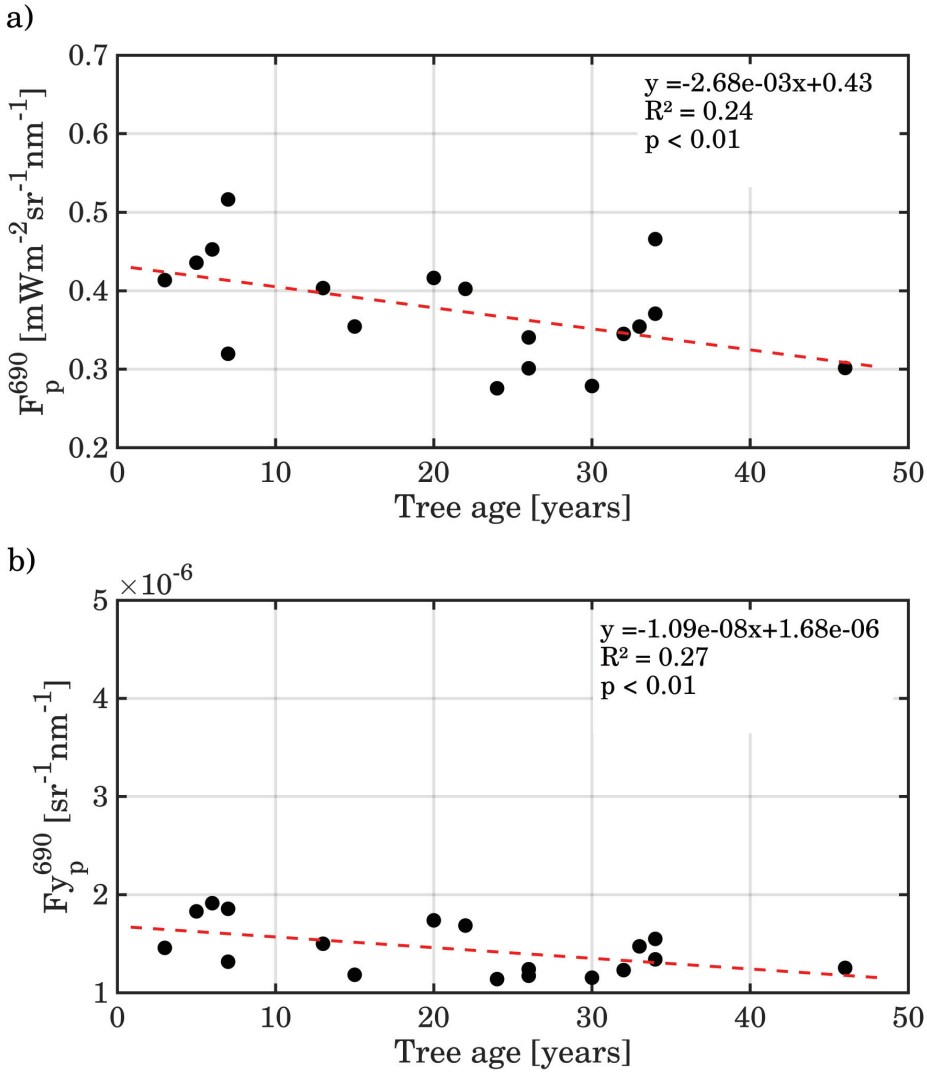

Figure 12: Mean of red F radiance (upper panel) and the red F yield (lower panel) computed at coarse spatial resolution (84 m × 84 m) *vs.* tree age. Note that the axis ranges are deliberatively set equal to those of Figs. 9a and 11a, respectively, in order to facilitate visual comparison.

cover and tree age and we did not find any statistically significant result, although a relevant variability of fractional cover across the different stands (Figure 13b).

To properly interpret F in mixed pixel situations, typical of satellite remote sensing, the spatial variability of vegetation vegetation fractional cover (fc) has to be taken into account. The relationship between CCFI and tree age obtained with aggregated pixel data (84 m × 84 m) is shown in Figure 14. Clearly, CCFI is not the same physical quantity as Fy, since it is not normalized by the absorbed radiation. However, it can provide a surrogate of Fy_{lob}^{690} with potential to account for sub-pixel heterogeneity in coarse spatial resolution data. The relationship shown in Figure 14, closely resembles those for the loblolly red F (Fig. 9a) and its yield (Fig. 11a), providing justification and support for the use of this index in interpreting F retrieved from coarse resolution mixed pixels.

2.4 DISCUSSION AND CONCLUSIONS

2.4.1 Solar-induced canopy fluorescence and age-related processes

A growing body of evidence demonstrates the relationship between F yields and photosynthetic rates, and it is well known that F can be used to monitor plant stress at leaf and canopy levels (*e.g.*, Ač et al. 2015; Meroni et al. 2009). However, the characteristics of F emissions of forest stands of different age have never been investigated. At tree-scale, with HyPlant data at full spatial resolution, our results clearly indicate that in loblolly pine: i) F_{lob}^{690} and Fy_{lob}^{690} vary with stand age; measured levels of F_{lob}^{690} were larger in younger trees compared to older ones (up to 60%) and the decline of Fy_{lob}^{690} with stand age (Fig. 11a) is more pronounced than that for F_{lob}^{690} (Fig. 9a), or for Fy^{*690}_{lob}; ii) only F_{lob}^{690} and Fy_{lob}^{690} declined with tree age, while F_{lob}^{740} and Fy_{lob}^{740} did not (Figs. 9b and 11b).

Overall, Fy_{lob}^{690} seems more informative about tree-age related processes than Fy^{*690}_{lob} (the R^2 value for Fy_{lob}^{690} is about 87% higher) and F_{lob}^{690} radiance itself.

No statistically significant relationship was found between LAI, chlorophyll content, carbon and nitrogen concentration with tree height and age (Table 1 and Figure 8), so that we can reasonably hypothesize that the decline of Fy_{lob}^{690} with age is not primarily driven by biophysical or biochemical parameters. Consequently, within canopy re-absorption of F_{lob}^{690} should not have a main role in Fy_{lob}^{690} decline related to tree age. The decline of F_{lob}^{690} may therefore most likely relate to the underlying physiological processes, that downregulate the photosynthetic activity of the plants during their life cycle. g_s and P_{net} measurements performed at Parker Tract in September clearly show significant reduction with stand age (7 years old trees = 58.2 $mmol\,m^{-2}\,s^{-1}$ for g_s and 5.7 $\mu mol\,m^{-2}\,s^{-1}$ for P_{net}; 23 years old trees

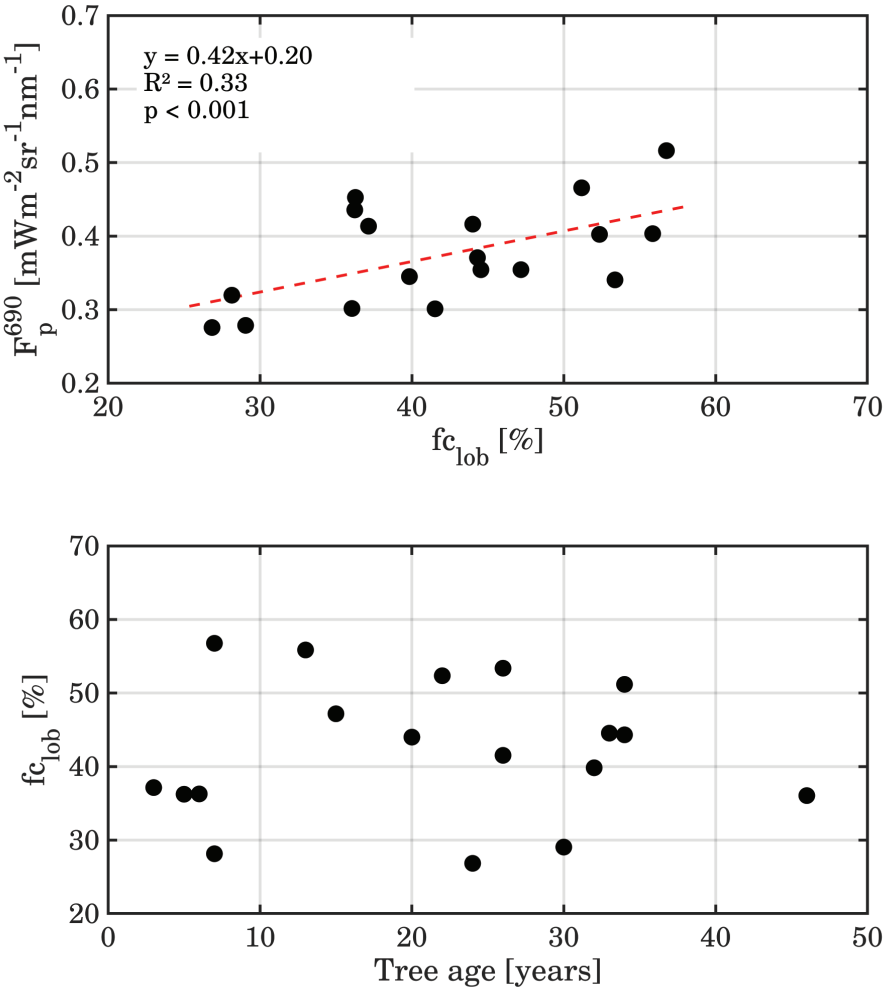

Figure 13: Relationships between aggregated (84 m × 84 m) red fluorescence and loblolly fractional cover (a), and between fractional cover and tree age (b).

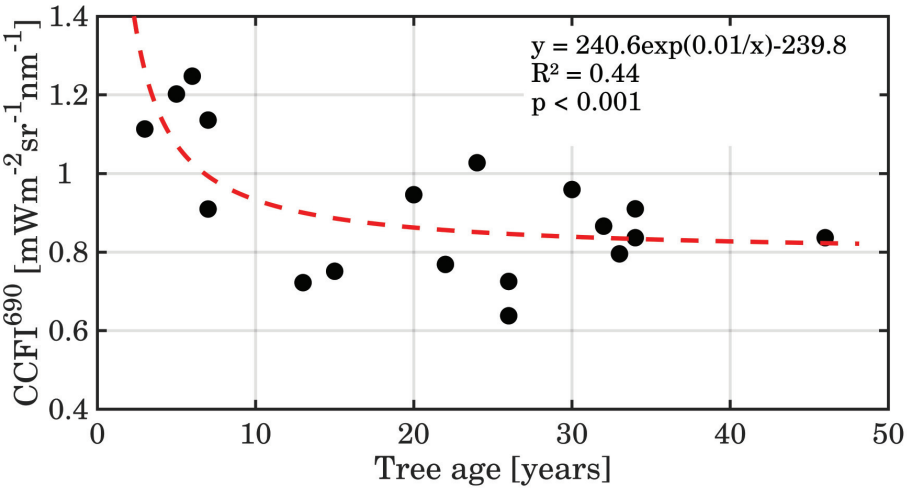

Figure 14: CCFI computed for red F *vs.* tree age.

= 49.5 mmol m^{-2} s^{-1} and 3.8 µmol m^{-2} s^{-1} for P_{net}) and potentially explain the drop of red fluorescence with age. In addition, combining results from predawn water potentials and P_{net} we could determine that mature trees had a reduction in 5.5 µmol m^{-2} s^{-1} MPa^{-1}, as opposed to only 2.9 µmol m^{-2} s^{-1} MPa^{-1} for the young trees. Those values indicated that between June and September mature trees were more sensitive to soil drying, and that the decline in soil water content had a larger effect on P_{net} in old trees than in young trees. Since these measurements only refer to two stands of young and mature trees, to better interpret our findings we also exploited the results observed in the loblolly pine forest at Duke Forest, which exhibits similar Site Index (Figure 6) and has been used for relevant investigations in this context (Domec et al., 2012; Drake et al., 2011, 2010; Noormets et al., 2010). Drake et al. (2010) and Drake et al. (2011) showed that light-saturated photosynthetic CO_2 uptake, the concentration of CO_2 within needle air-spaces and stomatal conductance to H_2O declined with tree age due to an increasing water limitation of the plants, while stomatal limitation to net photosynthesis increased, supporting the hydraulic limitation hypothesis as revised by Ryan et al. (2004) and Ryan, Phillips, and Bond (2006). We exploited the stomatal limitation model developed by Drake et al. (2010) and compared it with the observed decline in Fy_{lob}^{690}, depicting two opposite trends (Figure 15). It is thus plausible to hypotesize that the decline of red F yield is a primary consequence of the reduced carbon and water availability induced by the water limitation pro-

cesses in aging loblolly trees. In other words, the reduced water availability triggers stomata to close, which reduces leaf-internal CO_2 concentrations in the leaf tissue and limits the ability of the carbon fixing enzyme RuBisCO to fix CO_2. This in turn may cause a tailback into the electron transport and finally this is seen in a variation of F (Ač et al., 2015; Damm et al., 2010; Flexas et al., 2002; Rascher et al., 2004; Zarco-Tejada, González-Dugo, and Fereres, 2016). Moreover, the observed drop in red F yield occurs around age 10–15, which for loblolly corresponds to the physiological age of demarcation between juvenile and mature wood (Tasissa and Burkhart, 1998). Domec et al. (2012) showed that cambial activity is closely related to stomatal conductance, thus further enforcing the link between the observed F decline and the increasing water limitation during the physiological maturation process of loblolly pine. However, the drop we observed in Fy_{lob}^{690} is steeper than the increase of stomatal limitation reported at Duke Forest. Our data show in fact a sharp drop in Fy_{lob}^{690} before age 10–15 and then a limited change, while at Duke Forest the stomatal limitation clearly increases up to 40 years. Additional studies are therefore needed to fully characterize the link between these trends and to further unravel the role of physiology in driving fluorescence variability. Even though our analysis has been conducted using pure loblolly pixel only, hence minimizing the effect of canopy closure and mutual shading, the description of the radiative transfer in partly or fully shaded pixels, such as the complex stands in Parker Tract, is challenging and therefore we are aware that other functional and structural factors may partially contribute and explain our findings. Changes in leaf structure, needle length, shoot shape (clumping) and wax deposits on leaf surfaces with aging may in fact alter absorption/scattering of red fluorescence, enhancing the observed decrease with age. Therefore, we cannot completely discard a residual influence of canopy structure, a generic scattering effect with aging or changes in specific leaf area before and after canopy closure, which is reached at stand age of approximately 10 years. In addition, the complex canopy structure of the older pine trees not only subtly increases the APAR but may also produce stronger reabsorption of the red fluorescence within the canopy and therefore reduce the measured top-of-canopy fluorescence. In this study we have addressed the change in F emission from juvenile to mature stands, however future research, considering the natural lifespan of the loblolly trees of 100+ years old (Burns and Honkala, 1990), is needed to confirm our findings. Moreover, accurate determination of Fy should require an estimation of PAR absorbed by green leaves (*e.g.*, Gitelson and Gamon 2015; Zhang et al. 2016) and this could be another key point that should be considered for future investigations.

Although a statistically significant decreasing trend is clearly recognizable in Fy_{lob}^{690} values as plants become older, no significant relationship with tree age was found with F_{lob}^{740} or Fy_{lob}^{740} (Figs. 9b and 11b). The fact that red fluorescence, rather

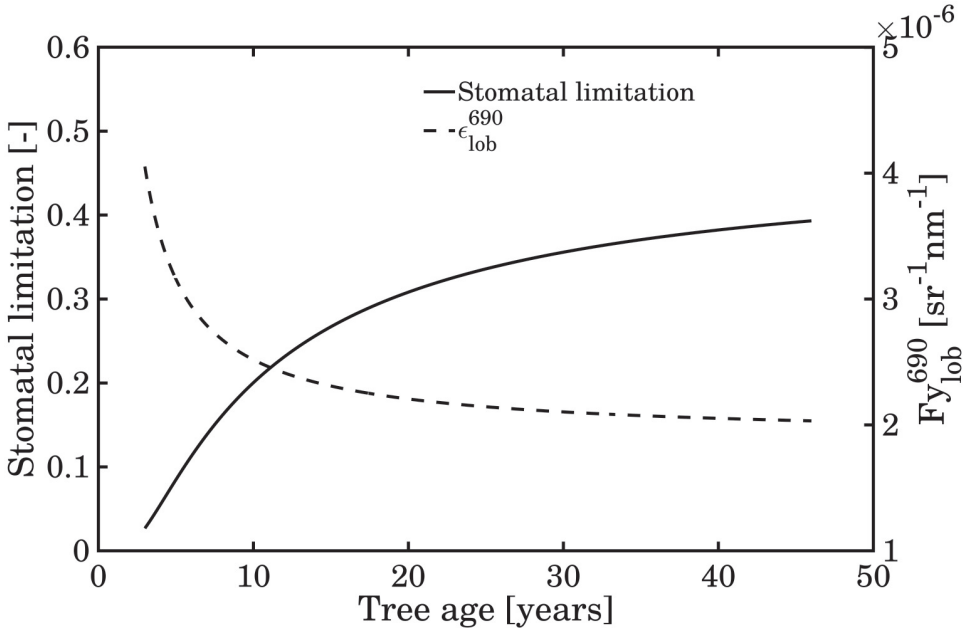

Figure 15: Modeled function of the stomatal limitation in the loblolly chronosequence at Duke Forest using the function derived by Drake *et al.* (2010) and modeled red F yield of the loblolly pine trees at Parker Tract obtained by the function presented in Figure 11a.

than far-red, seems more sensitive to describe these physiological processes can be considered in line with the recent study of Verrelst et al. (2016), which found the red fluorescence as the most sensitive to the canopy net-photosynthesis. Unfortunately, only a few recent studies (Cheng et al., 2013; Goulas et al., 2017; Joiner et al., 2016; Louis et al., 2005; Middleton et al., 2015; Rossini et al., 2015; Wieneke et al., 2016) exploiting both red F and far-red F have been conducted, and future investigations are necessary to consolidate the results found here.

If fluorescence yield changes as trees age, new information will be needed to account for variations in vegetation age classes across landscapes. However, we do not currently know the behaviour of fluorescence when other species- and age-related processes are involved (*e.g.*, within the hypothesis of nutrient limitation) nor do we know how fluorescence behaves across different ecosystems. Consequently, the relationship between F and tree age reported here cannot be generalized or used to track age classes. Further studies, especially dedicated experiments and modeling activities, may help in understanding how the F dynamics can contribute to a better description of the environment, age-related dynamics and climate interactions. The use of Radiative Transfer Models (RTMs) incorporating F (*e.g.*, Hernández-Clemente et al. 2017; van der Tol et al. 2009) coupled with ecosystem process model for estimating storage and flux of carbon, nitrogen and water (*e.g.* BIOME-BGC, Running and Gower 1991) in future research may help in better describing and understanding the role of F in age-related processes.

2.4.2 The need to use normalized F metrics at coarse resolution scale

Although new progress has been made in the methodological and technical aspects of F signal retrieval from space, as shown in recently published global maps (*e.g.*, Joiner et al. 2016), there are definite limitations for F interpretation based on large satellite pixels (*e.g.*, GOME-2, $40\,\mathrm{km} \times 80\,\mathrm{km}$; GOSAT, $10\,\mathrm{km} \times 10\,\mathrm{km}$) which are inevitably comprised of mixed components. Although several orbital missions acquire far-red F at better spatial resolutions (*e.g.*, OCO-2, $\approx 1\,\mathrm{km} \times 2\,\mathrm{km}$; and the upcoming ESA TROPOMI/Sentinel-5P, $7\,\mathrm{km} \times 7\,\mathrm{km}$), the possibility to produce high spatial resolution F maps from space is not yet available. Some of these disadvantages will be mitigated with the advent of the FLEX mission, which will provide full fluorescence emission spectra globally, at an ecologically relevant spatial scale of $0.3\,\mathrm{km} \times 0.3\,\mathrm{km}$, thus reducing the mixture problems currently encountered. The intra-pixel mixture effect is a confounding factor for F signal interpretation and it should be mitigated wherever possible and only after understanding the impact of spatial scale on the F signal, it will be possible to properly

exploit the use of fluorescence for plant status or for biomass applications in heterogeneous landscapes.

For coarse spatial resolution remote sensing observations, the computation and interpretation of Fy (as presented in Equations 6,7) is difficult due to the challenge in characterizing F and APAR for pure target vegetation components. Our results indicate that the mixing of components at coarse spatial resolutions can be considered a "contamination" that hinders the relationship between fluorescence and tree age-related processes, so that thay are no longer clearly detectable in the aggregated (coarse) pixels. Results from analysis with spatially aggregated data at stand-scale revealed that the relationships between red F radiances and yields (Figs. 12a and 12b) were substantially weakened by spatial averaging. In fact, the statistical success in describing the relationship for red F yield was reduced by almost 60% (R^2: 0.65 $\rightarrow$ 0.27, Figs. 11a,12b) and for red F radiances by $\approx$ 50% (R^2: 0.45 $\rightarrow$ 0.24, Figs. 9a and 12a), and the aggregated trends appeared more linear, solely due to spatial aggregation from 1 to 84 m. To mitigate the impact of surface heterogeneity, we propose the CCFI, which was able to produce acceptable results across a range of spatial resolutions (Fig. 14). In the use of the CCFI, the fc_{lob} normalization may be closely related to the fraction of Intercepted PAR (Pickett-Heaps et al., 2014), while less related to the amount of canopy pigments and stand darkness. Thus CCFI, by exploiting fractional cover, seems able to minimize the effects of canopy structure, enhancing differences in the fluorescence yield of young and old loblolly pine trees.

The vegetation fractional cover is a key vegetation parameter that has already been successfully produced using different remote sensing techniques, by exploiting optical or LiDAR imagery, from several current and past airborne or satellite data operating at different spatial and temporal resolutions (*e.g.*, Baret et al. 2007; Busetto, Meroni, and Colombo 2008; Carlson and Ripley 1997; Chen and Cihlar 1996; Gutman and Ignatov 1998; Jiménez-Muñoz et al. 2005; Latifovic and Olthof 2004; North 2002; Olthof and Fraser 2007; Verhoef and Bach 2007). In the context of the FLEX mission, vegetation fractional cover could be dynamically derived at higher spatial resolution from Landsat or Sentinel-2 like missions and then incorporated into the FLEX processing chain to compute the CCFI. The vegetation fractional cover can be more easily estimated than APAR from classification techniques and land use/cover maps. The real benefit in using fractional cover rather than APAR as a normalization tool is that it is more independent of illumination conditions and more stable over time. Thus, it is not mandatory to measure or compute it simultaneously with fluorescence, as it is for APAR, an instantaneous quantity highly dependent on time of acquisition, as fluorescence is. For the satellite perspective, the cosine of the zenith angle normalization can be added to CCFI to take into account the effects of temporal variability of incoming PAR. The com-

putation of CCFI is quite straightforward since it only requires, in addition to F radiances, the knowledge of the fractional vegetation cover in each pixel. However, this normalization cannot be considered as a replacement of Fy, but rather a complementary index that can be used under specific assumptions. CCFI is not applicable in a general framework at canopy level with airborne or satellite measurements, but only in some conditions, where two components with high F contrast contribute to the recorded signal. For savannah-like ecosystems, forests without understory and crops in certain phenological phases, this normalization technique may help to better detect plant status and processes. This index is not particularly suited for fragmented agricultural landscapes with different crops within the same pixel or for complex mixed forests, and therefore additional studies are needed to define strategies for global scale applications. Moreover, further studies exploiting new emerging 3-D radiative transfer models incorporating fluorescence, like FluorWPS (Zhao et al., 2016), FluorFLIGHT (Hernández-Clemente et al., 2017) and DART (Gastellu-Etchegorry et al., 2017) will help to test the performance of CCFI and the effects caused by the canopy structure on the fluorescence signal recorded from mixed pixels. In summary, the CCFI index can be applied, under certain conditions, to coarse spatial resolution data to minimize confounding factors due to the spatial variability of canopy structure, and it is expected to be suitable for applications assessing vegetation function in future Earth Observations in the fluorescence era.

3 DYNAMICS OF SOLAR-INDUCED CHLOROPHYLL FLUORESCENCE AND REFLECTANCE TO DETECT INDUCED VARIATIONS IN PHOTOSYNTHETIC EFFICIENCY

ABSTRACT

[1] The passive measurement of solar-induced chlorophyll a fluorescence (F) represents the most promising tool to remotely quantify changes in photosynthetic functioning at large scales. However, the limited knowledge on the complex relationship between this signal and other processes related to photosynthesis restricts its interpretation under stress conditions. A field campaign was planned to address this issue by inducing variations of photosynthesis and combining daily airborne and ground-based measurements of fluorescence, reflectance and surface temperature. A lawn was sprayed with different doses of an herbicide (Dicuran), differentially inhibiting photosynthesis as detected by chamber gas exchange measurements. This inhibition resulted in a rapid increase of the solar-induced fluorescence (measured at 687 nm and 760 nm) and of the Photochemical Reflectance Index (PRI). The increase of PRI suggests that Dicuran has also an inhibitory effect on the Non-Photochemical Quenching (NPQ). Canopy temperature also increased after the application of Dicuran. A later decrease of fluorescence and PRI was observed together with a reduction of chlorophyll a content and a drop of pigment-related vegetation indices (i.e. NDVI and MTCI). The dosage of Dicuran had an impact in the magnitude of the fluorescence change. The results permitted to formulate a conceptual model that explains the changes observed in all these pa-

1 The content of this chapter has been submitted to *Plant, Cell & Environment* as Pinto, F., Celesti, M. (co-first authorship), Alberti, G., Cogliati, S., Colombo, R., Juszczak, R., Miglietta, F., Palombo, A., Panigada, C., Pignatti, S., Rossini, M., Sakowska, C., Schickling, A., Schuettemeyer, D., Stróżecki, M., Tudoroiu, M., Rascher, U. "Dynamics of solar-induced chlorophyll fluorescence and reflectance to detect induced variations in photosynthetic efficiency".

rameters and that ultimately can be used to elucidate the mechanisms underlying the changes of photosynthetic activity.

Keywords: solar-induced chlorophyll fluorescence, PRI, photosynthesis, Dicuran, canopy temperature

3.1 INTRODUCTION

Photosynthesis is a highly regulated process that dynamically adapts in order to optimize the use of light while avoiding damage in the photosynthetic apparatus. The quantification of these dynamics is of outmost importance to understand the responses of photosynthesis to changes in the environmental conditions. However, measuring these fluctuations is difficult. They occur at different spatial and temporal scales and they do not necessarily involve changes in the biochemical and biophysical properties of the vegetation. Recently, the passive detection of solar-induced fluorescence has been proposed as an approach with a high potential to detect dynamics of photosynthesis (Rascher et al., 2015; Rossini et al., 2015a). Further, the possibility to retrieve fluorescence from remote sensing platforms provides new opportunities to assess plant photosynthetic functions at different temporal and spatial scales. The fluorescence emission is directly linked to photochemistry in plants and it is one of the pathways used by the photosynthetic machinery to dissipate the excess of absorbed light and reduce photo-oxidative stress (Porcar-Castell et al., 2014). Characterized by having two emission peaks around 690 nm and 740 nm, the fluorescence signal is emitted by the chlorophyll a molecules under the prevailing light conditions. At leaf scale, actively induced fluorescence has been used for decades to obtain information on plant photosynthetic activity, helping to elucidate many important features of this process (Papageorgiou and Govindjee, 2004). However, this method is impractical for measurements at canopy or larger scales. Through high spectral resolution radiance measurement of the vegetation, the Fraunhofer Line Depth (FLD) principle allows the passive retrieval of the fluorescence that generates from the absorption of solar radiation under natural conditions (*i.e.*, solar-induced F). This approach opens new perspectives for the measurement of fluorescence to a wide range of different spatio-temporal scales (Meroni et al., 2009). In the last years, several studies have demonstrated the feasibility of measuring fluorescence in the red region (*i.e.*, $\approx$ 690 nm) (F_R) and fluorescence in the far-red region (*i.e.*, $\approx$ 740–760 nm) (F_{FR}) from ground (Cogliati et al., 2015a; Daumard et al., 2010; Pinto et al., 2016; Rossini et al., 2016, 2010), airborne (Damm et al., 2014; Rascher et al., 2015; Rossini et al., 2015a) and satellite platforms (Frankenberg, Butz, and Toon, 2011; Frankenberg et al., 2011; Guanter et al., 2012; Joiner et al., 2011; Joiner et al., 2016). Furthermore, the

FLuorescence EXplorer (FLEX) mission of the European Space Agency (ESA) will be the first satellite mission specifically intended for fluorescence retrieval from space (Drusch et al., 2017). The primary interest of the scientific community for the F signal has been its potential use for improving remote estimations of Gross Primary Production (GPP) based on the Monteith's Light Use Efficiency (LUE) concept (Damm et al., 2010; Guanter et al., 2014; Lee et al., 2013; Perez-Priego et al., 2015; Rossini et al., 2010; Schickling et al., 2016; Wieneke et al., 2016). Nevertheless, the possibility of using remotely sensed F for early stress detection is gaining a significant attention (*e.g.*, Meroni et al. 2008; Rossini et al. 2015a; Rossini et al. 2015b). Stress events are associated with a reduction in the actual photosynthetic activity of plants, and thus changes in the F emission are expected before any noticeable effect on leaf reflectance. However, the co-existence of F with the other two de-excitation pathways, *i.e.* the NPQ and photochemistry (Photochemical Quenching (PQ)), complicates the interpretation of this signal in response to stress. There is not a unique relationship between PQ and F, meaning that F can either increase or decrease depending on the stressor. Recently, Ač et al. (2015) performed a meta-analysis of the response of F_R and F_{FR} to different stressors (*i.e.*, temperature, water and nitrogen availability) and observed consistent stressor-specific patterns in F values. Notwithstanding these findings, the further development of a mechanistic understanding of the link between F and photosynthetic activity under stress depends upon additional information on the NPQ activity and other physiological and physicochemical factors that can eventually affect this relationship, such as stomatal conductance or pigment composition. Potentially, this information can also be obtained using remote sensing. Numerous spectral vegetation indices have been proposed for the quantification of leaf pigments. In particular, indices using bands in the red and red-edge regions are sensible to variations of chlorophyll content in the leaves. Another technique providing relevant physiological information is thermography. Measurements of canopy temperature have been widely used for remote assessments of stomatal conductance (Berni et al., 2009; Fuentes et al., 2012; Panigada et al., 2014; Zarco-Tejada, González-Dugo, and Berni, 2012). On the other hand, the remote quantification of the NPQ is particularly challenging. Gamon, Peñuelas, and Field (1992) formulated the PRI after observing that de-epoxidation of violaxanthin - a process directly involved in the NPQ - causes changes in the leaf reflectance at 531 nm. Strong correlations have been found between PRI and NPQ at leaf and canopy level (*e.g.*, Filella et al. 2009; Filella et al. 1996; Garbulsky et al. 2011; Porcar-Castell et al. 2012). However, measurements of PRI at large vegetation scales can be constrained by the confounding effect of the canopy architecture (*e.g.*, Garbulsky et al. 2011). This study explored the capacity of passive measurements of solar-induced chlorophyll a fluorescence (F) to detect stress-induced short-term dynamics of photosynthetic efficiency in vegetation. Canopy temperature and PRI

were also investigated to explain better the effect of the stress on the vegetation. A dedicated experiment was designed, where plots of homogeneous lawn were treated with different doses of an inhibitor of the photosynthetic electron transport. A time series of very high spectral resolution radiance measurements was acquired at top-of-canopy using field and airborne sensors. The consistency between ground-based and airborne measurements of top-of-canopy fluorescence and reflectance products was assessed. Complementary measurements of surface temperature were acquired using an airborne hyperspectral thermal camera. Parallel ground measurements of carbon dioxide (CO_2) assimilation at canopy level and destructive measurements of chlorophyll content were used for validation of the remote sensing approach. We discuss the temporal evolution of F, PRI, surface temperature and chlorophyll content in relation to the mechanism of action of the stressor. Further, the collected data were used to formulate a conceptual model that linked F with photosynthesis functioning under the current stress conditions.

3.2 MATERIAL AND METHODS

3.2.1 Study site and experiment design

The experiment took place from 7th June 2014 to 3rd July 2014 over a homogeneous lawn of *Poa pratensis* and *Lolium perenne* grown and managed commercially in a lawn farm in Latisana, Italy (Lat: 45.7784°N, Lon: 13.0133°E). In order to induce photosynthetic inhibition, the plants were treated with Dicuran 700 FW (Syngenta AG) which is a commercial formulation of Chlortoluron (3-(3-chloro-p-tolyl)-1,1-dimethylurea). This herbicide inhibits photosynthesis using the same mechanism of action as the herbicide DCMU (Weed Science Society of America, 2016). The DCMU has been widely used in photosynthesis and chlorophyll fluorescence studies because it enhances the fluorescence emission by blocking the electron transport chain in the photosynthetic apparatus (Carter et al., 1996; Lichtenthaler and Rinderle, 1988; Schreiber, 1986). In particular, the DCMU displaces the plastoquinone at the QB binding site on the D1 protein and thereby blocks electron flow from QA to QB. Three plots of $12\,\mathrm{m} \times 9\,\mathrm{m}$ were sprayed using a backpack sprayer with different concentrations of Dicuran: $24\,\mathrm{ml\,l^{-1}}$ (plot D24), $6\,\mathrm{ml\,l^{-1}}$ (plot D6) and $1.5\,\mathrm{ml\,l^{-1}}$ (plot D1.5). Due to logistic constraints, the plots were sprayed at two different dates. Plot D24 was treated in the morning of 12th June 2014, whereas plots D6 and D1.5 were sprayed on 19th June 2014. At each application date, a control plot was sprayed with water. This helped to account for the differences in weather and vegetation conditions between the treatments. While the Control 1 was compared with plot D24, the Control 2 was used

with plots D1.5 and D6. In order to facilitate the comparison of temporal trends between the treatments, all results were expressed in terms of Days After Treatment (DAT). A representation of the field and the distribution of the experiments are described in Figure 16. The spraying and measurements took place under clear sky conditions. During the first part of the campaign (*i.e.*, from 11th June 2014 until 15th June 2014) the weather was stable. In the subsequent days the sky presented some clouds and there was some rainfall in 15th June 2014 and 25th June 2014. However, all measurements were taken only in time windows of clear sky.

3.2.2 Aerial hyperspectral and thermography measurements

Aerial hyperspectral images were obtained using the HyPlant airborne sensor (Specim, Finland) which was mounted in a Cessna 208 Caravan. This hyperspectral imager consists of two push broom modules: the DUAL Channel Imager which provides contiguous spectral information from 370 to 2500 nm (Full Width at Half Maximum (FWHM) = 3 nm in the Visible and Near InfraRed (VNIR) and 10 nm in the Short Wave InfraRed (SWIR) spectral regions) and the Fluorescence Imager (FLUO), which produces data at very-high spectral resolution (FWHM = 0.25 nm) between 670 nm and 780 nm. Both imagers were mounted in a single platform with the mechanical capability to align their field of view (for details see Rascher et al. 2015). The hyperspectral images were recorded from 680 m above ground level resulting in a 1 m $\times$ 1 m of pixel size for both imagers. The measurements were performed around solar noon ($\pm$ 1 h) over the course of 13 days (Table 2). The images from the DUAL module were used to compute spectral reflectance and vegetation indices, while the images from the FLUO module were used for the estimation of F. The DUAL images were radiometrically calibrated and georectified using the CaliGeo toolbox (SPECIM, Finland). Then the Atmospheric & Topographic Correction model (ATCOR, ReSe Applications Schläpfer) was used to estimate the surface spectral reflectance from these images. Three 9 m x 9 m calibration tarps (*i.e.*, white, grey and black) were used to perform an in flight radiometric calibration of the DUAL images. The tarps were located next to each other in a parking lot 800 m away from the experimental site and simultaneous ground and aerial measurements of the tarps spectral radiance were achieved for each flight line. The spectral reflectance of the calibration tarps was measured with a Fieldspec Full Resolution (FR) spectroradiometer (Analytical Spectral Devices Inc., ASD, USA). Twenty measurements were taken over each tarp in order to characterize its spatial variability. A white reference panel (99% Spectralon®, Labsphere Inc., NH, USA) mounted on a leveled tripod was measured every five measurements on the tarps to calculate the sprectral reflectance. The results of

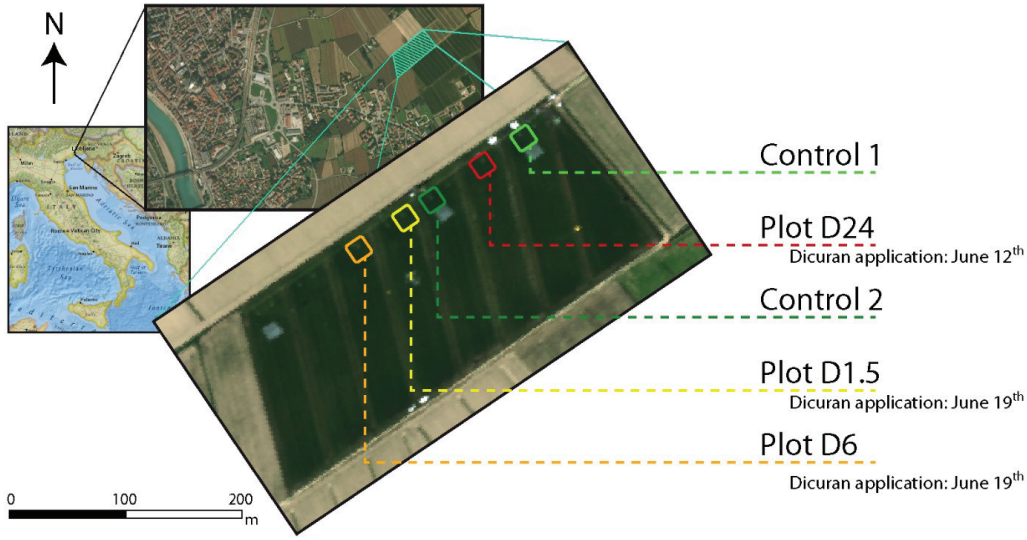

Figure 16: Map of the experimental site in Latisana (UD), Northern Italy.

Table 2: Core dataset of flight lines over the experimental site. DOY is day of the year, time is in UTC+2.

Date	DOY (2014)	Time of HyPlant	Time of TASI
11-Jun	162	14:52	14:51
12-Jun	163	13:40	14:23
13-Jun	164	13:52	14:09
17-Jun	168	-	10:17
18-Jun	169	-	13:20
19-Jun	170	13:34	11:27
21-Jun	172	12:57	14:27
22-Jun	173	12:10	-
24-Jun	175	11:56	-

the atmospheric correction were evaluated by computing the Root Mean Squared Error (RMSE) between the atmospherically corrected data of the DUAL and spectra acquired in-field over the tarps. The average RMSE for the three tarps for all wavelengths considering all the dates was 0.011, indicating a reliable atmospheric correction (Fig. 17). Three vegetation indices related to pigment concentration and photosynthetic activity were calculated from the DUAL module data: the Normalized Difference Vegetation Index (NDVI) (Rouse et al., 1973), the Meris Terrestrial Chlorophyll Index (MTCI) (Dash and Curran, 2007) and the PRI (Gamon, Peñuelas, and Field, 1992). For validation, these indices were also estimated at the ground level as close in time as possible to the airborne sensor overpasses (see Section 3.2.4). For the calculation of broadband vegetation indices (*i.e.*, NDVI and MTCI), several bands were averaged within each spectral region to reduce the noise. Table 3 describes the spectral bands used for the estimation of these indices from both platforms. The images from the FLUO module were radiometrically calibrated and corrected for the point spread function of the instrument using a sensor characterization and an algorithm developed in house. The georectification of the FLUO images was done using CaliGeo. The high-resolution data coming from the FLUO module was finally used to retrieve fluorescence. TASI-600 (ITRES Research Limited, Calgary, Canada) multispectral thermal images were acquired over the study area from 11th June 2014 afternoon until 21st June 2014. The TASI-600 is a pushbroom sensor with 32 spectral bands in the Long Wave InfraRed (LWIR) (8.0–11.5 µm) spectral range. The sensor has a field-of-view of 40° and FWHM of 0.1095 µm (for details see Pignatti et al. 2011). The TASI-600 data were acquired at an altitude of 900 m above ground level corresponding to a ground pixel resolution of 1 m. The days and time of thermal data acquisition are described in Table 2.

Table 3: Vegetation indices calculated from HyPlant DUAL data and ground-based spectroscopy. ρ is the spectral reflectance.

Index	Formulation	Reference
NDVI	$\frac{\rho_{NIR}-\rho_{RED}}{\rho_{NIR}+\rho_{RED}}$	Rouse et al. (1973)
MTCI	$\frac{\rho_{NIR}-\rho_{RED-EDGE}}{\rho_{RED-EDGE}-\rho_{RED}}$	Dash and Curran (2007)
PRI	$\frac{\rho_{530.5}-\rho_{569.9}}{\rho_{530.5}+\rho_{569.9}}$	Gamon, Peñuelas, and Field (1992)

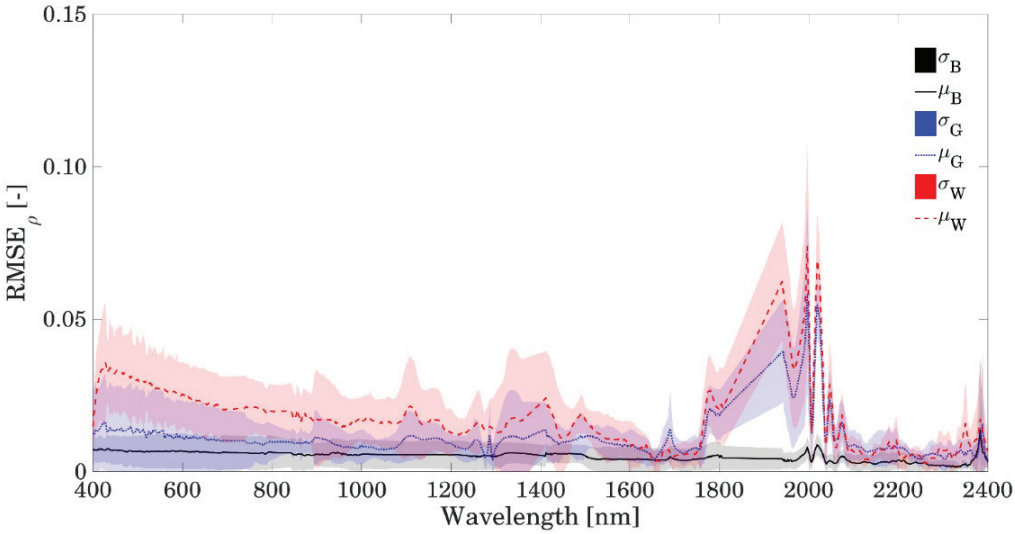

Figure 17: Validation of the atmospheric correction for aerial imagery. The lines represent the mean RMSE for each wavelength calculated by comparing airborne and ground-based spectral reflectance measurements from all the dates over three tarps with different level of reflectance: white (W; red dashed line), grey (G; blue line) and black (B; black line). The colored areas represent the standard deviation of the RSME calculated for each wavelength.

3.2.3 Airborne retrieval of solar-induced chlorophyll fluorescence

The fluorescence emitted by the vegetation can be decoupled from the reflected radiation using the FLD principle. In essence, FLD-based approaches exploit the atmosphere absorption bands, where the background solar radiation is strongly diminished and the contribution of F to the overall vegetation radiance increases (Maier, Günther, and Stellmes, 2003; Meroni et al., 2009; Plascyk, 1975). In this study, we used the improved Fraunhofer Line Depth (iFLD) proposed by Alonso et al. (2008) to estimate fluorescence in the O_2-A(*i.e.* at 760 nm; F_{760}) and O_2-B(*i.e.* at 687 nm; F_{687}) absorption bands. The iFLD method estimates the fluorescence by building a system of equations where the at-sensor radiance is modeled at two different wavelengths: inside (i) and outside (o) the absorption band. Following Damm et al. (2015), the radiance measured by an airborne sensor a specific wavelength over the vegetation can be described by:

$$L_j^{AtS} = \frac{E_j^o \cos\Theta_{il}}{\pi}\left[\langle\rho_{so}^j\rangle + \frac{\left(\langle\tau_{ss}^j\tau_{oo}^j\rangle + \langle\tau_{sd}^j\tau_{oo}^j\rangle + \langle\tau_{ss}^j\tau_{do}^j\rangle + \langle\tau_{sd}^j\tau_{do}^j\rangle\right)R_j}{1 - R_j\langle\rho_{dd}^j\rangle}\right] + \\ + \frac{F_j\left(\langle\tau_{oo}^j\rangle + \langle\tau_{do}^j\rangle\right)}{1 - R_j\langle\rho_{dd}^j\rangle}, j = i, o \tag{10}$$

where E^o is the extraterrestrial solar irradiance, Θ_{il} is the illumination zenith angle, ρ_{so} is the path reflectance of the atmosphere, and ρ_{dd} is the spherical albedo of the atmosphere. The terms τ_{ss} and τ_{sd} are the direct and diffuse transmittance of the atmosphere for sunlight, whereas τ_{oo} and τ_{do} represent the direct and hemispherical-directional transmittance in the view direction, respectively. Assuming that the irradiance and the fluorescence emission (F) are isotropic, and that the surface reflectance of the vegetation (R) has a Lambertian behavior, the atmospheric parameters described above (*i.e.*, E^o, ρ_{so}, ρ_{dd}, τ_{ss}, τ_{sd}, τ_{oo} and τ_{do}) can be estimated using MODTRAN according to Damm et al. (2015). Then, four variables are unknown in the system of equations: the reflectance and the fluorescence inside and outside of the absorption band (R_i, R_o, F_i and F_o). Assuming that both variables vary linearly between the outside and inside of the absorption band, the iFLD method relates them with the coefficients A and B as following:

$$\begin{cases} R_o = AR_i \\ F_o(\langle\tau_{oo}^o\rangle + \tau_{do}^o) = BF_i(\langle\tau_{oo}^o\rangle + \tau_{do}^o)) \end{cases} \tag{11}$$

with A and B estimated according to Alonso et al. (2008), the fluorescence inside the O_2-A and O_2-B bands can be calculated using Eq. 10 and Eq. 11 as:

$$F_i = \frac{AX_I(E_o + X_o\langle\rho^o_{dd}\rangle) - X_o(E_i + X_i\langle\rho^i_{dd}\rangle)}{[A(E_o + X_o\langle\rho^o_{dd}\rangle) - B(E_i + X_i\langle\rho^i_{dd}\rangle)][\langle\tau^i_{oo}\rangle + \langle\tau^i_{do}\rangle]} \tag{12}$$

with

$$X_j = \left(L_j^{AtS} - \frac{\langle E^o_j \cos\Theta_{il}\rangle}{\pi}\langle\rho^j_{so}\rangle\right), j = i, o \tag{13}$$

and

$$E_j = \frac{\langle E^o_j \cos\Theta_{il}\rangle}{\pi}\left(\langle\tau^j_{ss}\tau^j_{oo}\rangle + \langle\tau^j_{sd}\tau^j_{oo}\rangle + \langle\tau^j_{ss}\tau^j_{do}\rangle + \langle\tau^j_{sd}\tau^j_{do}\rangle\right), j = i, o \tag{14}$$

The atmospheric parameters were simulated at highest spectral resolution assuming middle latitude summer atmospheric conditions, martime aerosol model, and the default visibility of ATCOR (*i.e.*, 23 km). Then they were spectrally resampled to meet our sensor configuration taking into account the across-track spectral shift and FWHM. It is important to note that in those parts of Eqs. 10-13 that are enclosed between angle brackets, the parameters were first multiplied at their highest resolution and then their product was convolved to meet our sensor configuration. This is necessary in order to compensate for the strong modulation of these parameters by the absorption bands and their strong correlation over finite spectral intervals, which results in a direct violation of the Beer's law (Damm et al., 2015).

The use of standard atmospheric conditions can lead to inaccurate estimations of some atmospheric parameters that have a great impact on the final fluorescence values. Two empirical corrections were implemented to improve the accuracy of the fluorescence estimation. The first one aimed to obtain a better estimation of the path reflectance of the atmosphere. For a non-fluorescence target, the Eq. 10 could be simplified as a two-variable linear equation:

$$L_j^{AtS} = \frac{E^o_j \cos\Theta_{il}}{\pi}\langle\rho^j_{so}\rangle \cdot \left[\frac{(E^o_j \cos\Theta_{il})(\rho^j_{so})\left(\langle\tau^j_{ss}\tau^j_{oo}\rangle + \langle\tau^j_{sd}\tau^j_{oo}\rangle + \langle\tau^j_{ss}\tau^j_{do}\rangle + \langle\tau^j_{sd}\tau^j_{do}\rangle\right)}{\pi\left(1 - R_j\langle\rho^j_{dd}\rangle\right)}\right] R_j, j = i, o \tag{15}$$

where L_j^{AtS} and R_j represent the dependent and independent variables, respectively. For two or more non-fluorescence surfaces lying under the same illumination conditions, the values of the different atmospheric parameters could be

assumed to be the same. If the R_j and L_j^{AtS} of each of these non-fluorescence targets are known, and assuming a linear response of the sensor, a linear regression can be performed to estimate the constants of Eq. 15, and therefore to adjust the value of ρ_{so}^{j} (E_j^o and $\cos\Theta_{il}$ are known since they depend on the date and the time of the day and not on the atmospheric conditions). The calibration tarps were used for this purpose. The ρ_{so}^{j} estimated from the tarp measurements was assumed constant in the entire scene. Further inaccuracies and uncertainties in the atmospheric and sensor characterization were compensated using the Effective Transmittance Correction (ETC) method (Damm et al., 2014; Guanter et al., 2007). In this approach, values of τ_{oo}^{i} were adjusted across-track using a simple correction coefficient that is calculated from pixels that are known to be non-fluorescent surfaces (*e.g.*, bare soil; for details see Pinto et al. 2016). Since the primary driver of fluorescence emission at canopy level is the incoming radiation, it was necessary to normalize the values of fluorescence by Photosynthetically Active Radiation (PAR) in order to separate the treatments effect from natural variations in the illumination conditions along the experiment. Therefore, the apparent fluorescence yield (Fy^*) was computed as Fy^* = F/PAR for the fluorescence at 687 nm (Fy^*_{687}) and 760 nm (Fy^*_{760}).

3.2.4 Ground based spectroscopy

Downwelling and upwelling radiances were measured over the experimental plots with three portable spectrometers (OceanOptics, Dunedin, FL, USA) operating in the VNIR spectral regions (Table 4). The spectrometers were housed in a Peltier thermally regulated box (model NT-16, Magapor, Zaragoza, Spain) keeping the internal temperature at 25 °C in order to ensure the stability of both the intensity and the spectral information of the measured signal (Meroni and Colombo, 2009). The bare optical fiber of the spectrometers (field of view of 25°) were placed at 130 cm above the top of the canopy looking in nadir direction resulting in a measured circular surface of approximately 58 cm of diameter. A modified tripod allowed to alternate measurements between a calibrated white reference panel (99% Spectralon®, Labsphere Inc., North Sutton, NH, USA) and the vegetation (for further details see Rossini et al. 2016). Readings over the white panel were used to estimate the downwelling radiation. Ground-based spectral data were acquired from around 10:00 until 16:00, depending on the weather conditions. Measurements close to noon were selected in order to match the airborne data. Each measurement consisted of three spectral readings recorded sequentially: over the white panel, the vegetation and the white panel again. Each of these spectra represented the average of 10 and 3 scans - for the full range and the

Table 4: Summary of the technical characteristics of the Ocean Optics spectrometers (Dunedin, USA) used for the field measurements. "Range" is the spectral range, "SSI" is the Spectral Sampling Interval, "FWHM" is the "Full Width at Half Maximum" and "SNR" is the nominal Signal-to-Noise Ratio.

ID	Model	Range [nm]	SSI [nm]	FWHM [nm]	SNR
S-Full	HR4000	400-1000	0.24	1.00	300:1
S-O_2-B	QE65000	657-743	0.10	0.25	1000:1
S-O_2-A	HR4000	717-805	0.02	0.10	300:1

other two spectrometers, respectively - in order to reduce instrumental noise. The relative variation between the two measurements over the white panel was used as a quality check for the illumination condition stability. Spectrometers' dark current measurements were recorded to account for white noise in the data. The data were recorded using the dedicated software 3S (Meroni and Colombo, 2009) and processed with a IDL (ITTVIS IDL 7.1.1) application developed in house (Meroni et al., 2011). Five consecutive measurements were taken for each plot under stable illumination conditions before moving to the next one.

Ground reflectance measurements acquired in the VNIR regions were used to compute the vegetation indices indicated in Table 3. The fluorescence was estimated in the red and far-red region (F_{687} and F_{760}, respectively) using the Spectral Fitting Methods (SFM) originally presented in Meroni and Colombo (2006) and recently optimized in Cogliati et al. (2015b) at the O_2-B and O_2-A oxygen absorption bands. The spectral interval used for F_{760} estimation was set from 759.00 to 767.76 nm (*i.e.*, 439 spectral channels), while the spectral range between 684.00 and 696.00 nm (*i.e.*, 200 spectral channels) was used for estimating the F_{687}.

3.2.5 Canopy Gas exchange chamber measurements

The non-steady-state flow-through chamber system was used in order to estimate CO_2 and H_2O fluxes from the plots. The Net Ecosystem Exchange (NEE) and the ecosystem respiration (Reco) were derived directly from measurements using a transparent and an opaque chamber, respectively (chamber's dimension: 0.78 m × 0.78 m × 0.50 m). Chambers were equipped with fans, temperature sensor (T-107, Campbell Scientific, USA) and a vent to equilibrate pressure changes in accordance to Juszczak and Augustin (2013) as well as with SKP215 PAR quantum sensor (Skye Instruments, UK) installed on top of the transparent chamber.

No cooling devices were used (as described in Chojnicki et al. 2010) in order to not reduce H_2O fluxes. Gas concertation changes in the chambers were measured with the LI-840 infrared gas analyzer (Li-COR, Lincoln, NE, USA) installed in a portable control box (for details see Acosta et al. 2017; Chojnicki et al. 2010). During measurements, chambers were fixed to the preinstalled soil frames (one per experimental plot) inserted in the soil to 5 cm depth on 5th June 2014. Soil frames were leveled on the day of installation. The closure time of the transparent chamber was no longer than one minute to avoid overheating of the chamber headspace and two minutes for the opaque chamber. The flux measurements started at 10:00 AM and were continued till 16:00 (CEST), but only measurements taken around solar noon (± 1 h) were used to calculate average midday fluxes analyzed in this study. At noon, NEE measurements were taken just after reflectance and fluorescence measurements on the same plots. Reco measurements followed the NEE estimations. The measured CO_2 concentrations were corrected for water dilution in accordance to Perez-Priego et al. (2015). CO_2 and H_2O fluxes were calculated based on gas concentration changes over the closure time using the linear regression type as described in Juszczak and Augustin (2013). Fluxes were calculated from the first 30–40 seconds of measurements for data with the highest regression slopes in order to avoid underestimation of the fluxes due to *e.g.* gas saturation, in accordance with Hoffmann et al. (2015). The amount of CO_2 assimilated by GPP was calculated as the difference between Reco and NEE taken consecutively with both chambers. The LUE was calculated as the ratio between GPP and PAR.

3.2.6 Airborne retrieval of surface temperature

Thermal images were geometrically and radiometrically corrected with the GEOCORR and the RADCORR software (ITRES Research Limited, Calgary, Canada). An additional code developed by the Italian National Research Council (CNR IMAA; `http://www.imaa.cnr.it/`) was used to remove the blinking pixels that still affect the imagery (Santini et al., 2014). The atmospheric correction of spectral radiances was executed by applying the in-scene atmospheric compensation (ISAC) algorithm (Young, 1998). This procedure was chosen as it is commonly used for in-scene atmospheric thermal data correction, and because it requires only the at-sensor radiance data as input to estimate the upwelling radiance and transmissivity of the atmosphere. The temperature retrieval was then performed by using the temperature emissivity separation methods (TES), applying the normalization emissivity method and selecting an emissivity of 0.98 for the pixel with the maximum brightness temperature (Li et al., 2013). In order to validate the TASI-600 retrieved temperature we used the ground-measured temperature of a

swimming pool located in the Latisana test site and acquired using a thermocouple contemporary with the TASI overpass. The difference between the measured and average TASI temperature retrieved on the pool was 0.2 K. To reduce the white noise introduced by the TES algorithm in the temperature images, we retrieved for each flight-line the brightness temperature using a linear regression between the TES temperature images and the integrated radiance images. To account for the changes in the meteorological conditions along the experiment, the difference in temperature between each treated plot and the closest control plot (ΔT) was used to study the effect of the Dicuran in the canopy temperature.

3.2.7 Pigment concentration

Leaf samples were collected for laboratory measurements of the chlorophyll (Chl) and carotenoids (Car) content. Seven samples were collected for each plot 10 h after the treatments. Each of the samples consisted in 3–5 leaves. Fresh samples were weighted (fresh weight; FW) for later estimation of Chl content in $\mu g\, g_{FW}^{-1}$. The leaf material was harvested, placed in plastic tubes (Safe Lock, Eppendorf, Germany), stored immediately in liquid-nitrogen and later transferred into a $-80\,^{\circ}C$ freezer for long-term storage. The extraction of Chl a, Chl b and Car was carried out using a mixture of 1000 ml of 100% acetone buffered with 20 g of magnesium hydroxide carbonate and stored at 4 °C. Hereafter this solution is referred as acetone. The samples were grinded using 200 µl of acetone and 2 steel balls of 5 mm diameter in a mixer mill (MM200, Retsch, Germany) for two minutes. The extract was pipetted into a new 2 ml Eppendorf tube. The grinding jar and the steel balls were washed with acetone and this solution was used to fill the sample up to 500 µl. The samples were then centrifuged at 13 000 rpm for 5 minutes at 4 °C. The excess solution was then measured in the spectroradiometer (Uvikon XL, BIO-TEK Instruments, Winooski, VT, U.S.) using a 1 cm glass cuvette. The estimation of the concentration of Chl and Car was carried out using a modified version of the method suggested by Lichtenthaler and Buschmann (2001), where the absorbance readings at 470 nm, 645 nm, 662 nm and 710 nm were used according to the following formulas:

$$\begin{cases} \text{Chl a} = [11.24(A_{662} - A_{710}) - 2.04(A_{645} - A_{710})]\frac{\alpha}{\beta} \\ \text{Chl b} = [20.13(A_{645} - A_{710}) - 4.19(A_{662} - A_{710})]\frac{\alpha}{\beta} \\ \text{Car} = [(1000(A_{740} - A_{710}) - 1.9\text{Chl a} - 63.14\text{Chl b})/214]\frac{\alpha}{\beta} \end{cases} \quad (16)$$

where Chl and Car are expressed in $\mu g\, cm^{-2}$ or $mg\, g_{FW}^{-1}$. A_{470}, A_{662}, A_{645} and A_{710} represent the absorption reading at 470 nm, 645 nm, 662 nm and 710 nm,

respectively. The coefficients α and β represent the volume of the extract (*i.e.*, 5 ml) and the fresh weight of the sample in g, respectively.

3.3 RESULTS

3.3.1 CO_2 assimilation

Table 5 shows the results of the gas exchange measurements taken in all the treatments around noon the same day of the application of Dicuran, and in the subsequent three days in case of plot D24. All treated plots showed a drop of LUE and CO_2 assimilation (expressed as GPP) after the application compared to the control plot. The level of inhibition of photosynthesis was closely related with the dose of Dicuran. While the lowest concentration of Dicuran (*i.e.*, 1.5 ml l^{-1}) only induced a drop in GPP of about 17% in the first day, the dose of 6 ml l^{-1} reduced photosynthesis by nearly 35%. A significant decrease of GPP of nearly 90% was observed in plants treated with the highest dose (*i.e.*, plot D24). Similarly, the magnitude of the drop in LUE was determined by the dosage of Dicuran, with the lowest LUE observed in plot D24 three days after the treatment. In plot D24, the NEE tended to decrease in the next three days following the application. A similar trend was observed for GPP, with an exception on day 2 after the treatment, when an increase of GPP and LUE was detected. This behavior could not be confirmed for lower doses of Dicuran as the chamber measurements were not continued in the following day. The application of Dicuran also induced changes in respiration rate. An increase was observed in plots D24 and D1.5 immediately after the treatment. Respiration in plot D6 was smaller than in the control plot, but this effect might be attributed to drier conditions at this plot, which is confirmed by the smaller H_2O fluxes. The treatment with the herbicide did not have a significant effect in the evapotranspiration (*i.e.* H_2O fluxes) during the same day of the application. However, plot D24 showed a decrease compared to the control in the subsequent two days.

3.3.2 TASI surface temperature

A raise in the canopy temperature in all treated plots was detected by the aerial thermal images. Figure 18 shows how the difference in temperature between D24 and the control plot (ΔT) increased gradually during the five days following the application. A rise in ΔT of 0.8 K could be observed one day after the treatment. The peak of temperature for D24 was observed on DAT 5, where ΔT was 1.7 K.

Table 5: CO_2 fluxes, H_2O flux and LUE at midday for the treated and the control plots. GPP, Reco and NEE are expressed in [$\mu mol_{CO_2} m^{-2} s^{-1}$], LUE is in [$\mu mol_{CO_2} \mu mol_{PAR}^{-1}$] and F_{H_2O} (the flux of H_2O) is in [$mmol_{H_2O} m^{-2} s^{-1}$]. DOY is the day of the year.

DAT	Treatment	GPP	Reco	NEE	LUE	F_{H_2O}
0	Control	43.70 ± 1.2	17.96 ± 1.5	-25.74 ± 1.1	0.02333	9.97 ± 2.6
	D1.5	36.34 ± 6.5	27.86 ± 3.9	- 8.48 ± 2.6	0.01878	11.44 ± 0.2
	D6	28.20 ± 3.0	13.50 ± 2.7	- 14.69 ± 0.4	0.01494	9.30 ± 1.7
0	Control	38.79 ± 6.3	14.91 ± 1.5	- 23.89 ± 5.0	0.01971	11.88 ± 0.9
	D24	4.33 ± 1.4	22.08 ± 1.0	17.75 ± 2.4	0.0022	12.43 ± 1.1
1	Control	41.18 ± 3.3	20.45 ± 2.9	-20.73± 0.7	0.02041	9.97 ± 0.6
	D24	8.91 ± 1.6	23.33 ± 1.9	14.43 ± 2.4	0.00452	7.67 ± 1.2
2	Control	45.32 ± 5.1	22.27 ± 5.2	-23.05 ± 1.1	0.02106	8.01 ± 0.3
	D24	18.85 ± 4.8	33.53 ± 2.6	14.68 ± 2.3	0.00871	4.70 ±1.15
3	Control	49.79 ± 5.6	25.42 ± 4.8	-24.37 ± 0.8	0.02482	6.63 ± 0.4
	D24	3.78 ± 0.3	11.62 ± 1.1	7.84 ± 0.7	0.00169	6.21 ±0.02

In the following four days the ΔT decreased and the plot D24 had a similar temperature than the control by the end of the experiment. Plots treated with lower doses also showed an increase of temperature. D6 showed a ΔT of 0.6 K two days after the application while for D1.5 the ΔT was 1.1 K in the same time period. No further measurements were taken in the plots treated with lower doses. Therefore, it was not possible to see whether the temperature decreased in a similar way as in plot D24.

3.3.3 Changes in spectral vegetation indices as result of the Dicuran action

Airborne images revealed changes in the spectral reflectance of canopies treated with Dicuran. In treated plots, vegetation indices related to green biomass and leaf pigment concentration, such as NDVI and MTCI, showed a sustained decrease in time in comparison to the control (Figs. 20A and 20D). This was also observed in ground-based top-of-canopy measurements (Fig 20B and 20E), existing a good correlation between the values calculated from both platforms throughout the whole experiment (Fig 20C and 20F). Before the treatments, the plots showed values of NDVI around 0.84 and 0.9 for airborne and ground-based data, respectively (Figs. 20A and 20B). Two days after the Dicuran application, the NDVI decreased at a different degree in the treated plots while it remained constant for the control plots. In plot D24, the NDVI dropped continuously towards the end of the experiment, reaching a value nearly 10% lower compared to the control plots measured at the same time. In plots treated with lower doses this decrease was smaller. Moreover, two days after the treatment the value of NDVI tended to stabilize in these plots. The MTCI also dropped after the application of Dicuran (Figs. 19, 20D and 20E). However, these changes were larger than in NDVI, especially in the case of plots treated with lower doses. In both airborne and ground-based data, the MTCI in plots D1.5 and D6 showed a drop at a similar rate than in D24. Nevertheless, the latter showed a continuous decrease towards the last measurement while in the formers the MTCI stabilized three days after the application. Control plots did not vary significantly in their MTCI during the course of the experiment, showing always higher values than the treated plots. The dynamics of MTCI during the experiment were closely related to the changes observed in the content of Chl a in the leaves ($R^2 = 0.749$; $p < 0.01$; Fig. 21). This confirms that MTCI was a good proxy to detect changes in chlorophyll content induced by Dicuran. Substantial changes in PRI were also detected in the data collected by both platforms (Fig. 19, 20G and 20H). Treated plots showed a markedly increase of PRI immediately after the application of Dicuran. D24 showed the highest peak while D6 the

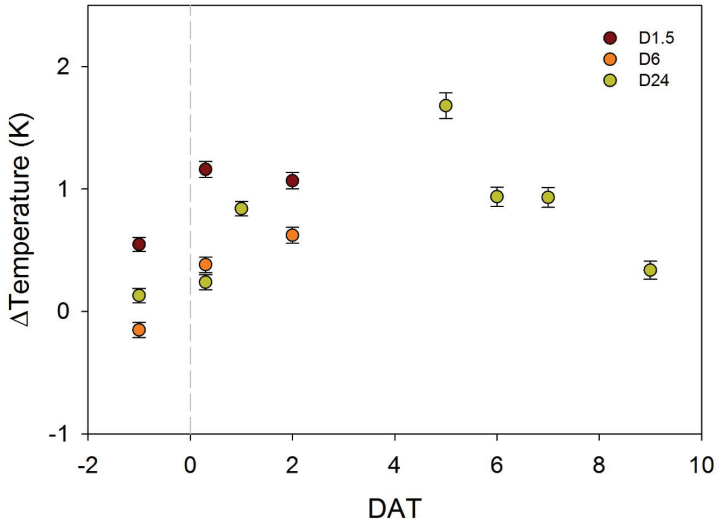

Figure 18: Dynamic changes of canopy temperature in plots treated with different doses of Dicuran. Values represent the difference in temperature (in K) between each plot and an adjacent control plot.

lowest. In all the treatments, the peak was followed by an abrupt decrease. After seven days, the PRI of all treatments reached values below those measured in the control plots and remained low until the end of the experiment showing no signs of recovery. Considering that the calculation of PRI includes wavelengths in the visible part of the spectrum, the relationship between PRI and leaf pigments was tested. A significant correlation ($R^2 = 0.33$; $p < 0.05$) was found only between PRI and the ratio carotenoids/chlorophyll (Car/Chl; Fig. 21). Therefore, the decline of Chlorophyll concentration would explain 30% of the drop of PRI from day one after the treatment.

3.3.4 Dynamics of solar-induce chlorophyll fluorescence

Figure 22 shows the maps of F_{687} and F_{760} retrieved from the HyPlant sensor. F values were extracted from the maps and normalized by the incoming PAR to compute the Fy^* in Figure 23. Dynamic changes of Fy^*_{687} and Fy^*_{760} in response to the treatment with Dicuran were detected by both airborne and ground-based platforms (Fig. 23). Before the application of the herbicide the aerial images depicted similar fluorescence yields (*i.e.*, $Fy^*_{687} \approx 1.5 \times 10^{-5}$ and $Fy^*_{760} \approx 4.3 \times 10^{-5}$) for all the plots. A substantial and fast increment in Fy^* was observed in all the treated

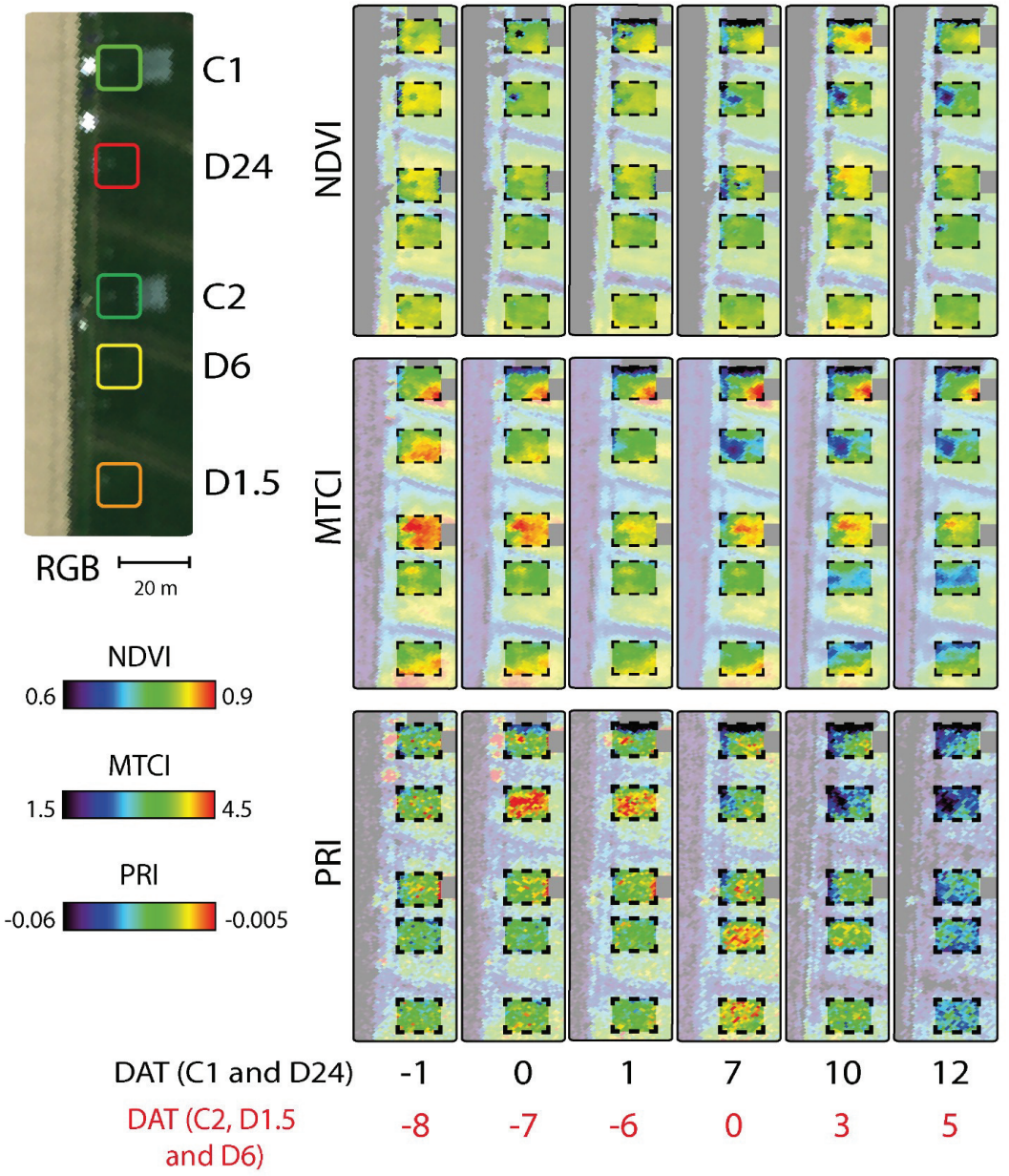

Figure 19: Representation of airborne images showing the dynamics of vegetation indices NDVI, MTCI and PRI for each plot. Time is expressed in days after treatment (DAT), where DAT 0 represents the day of the application.

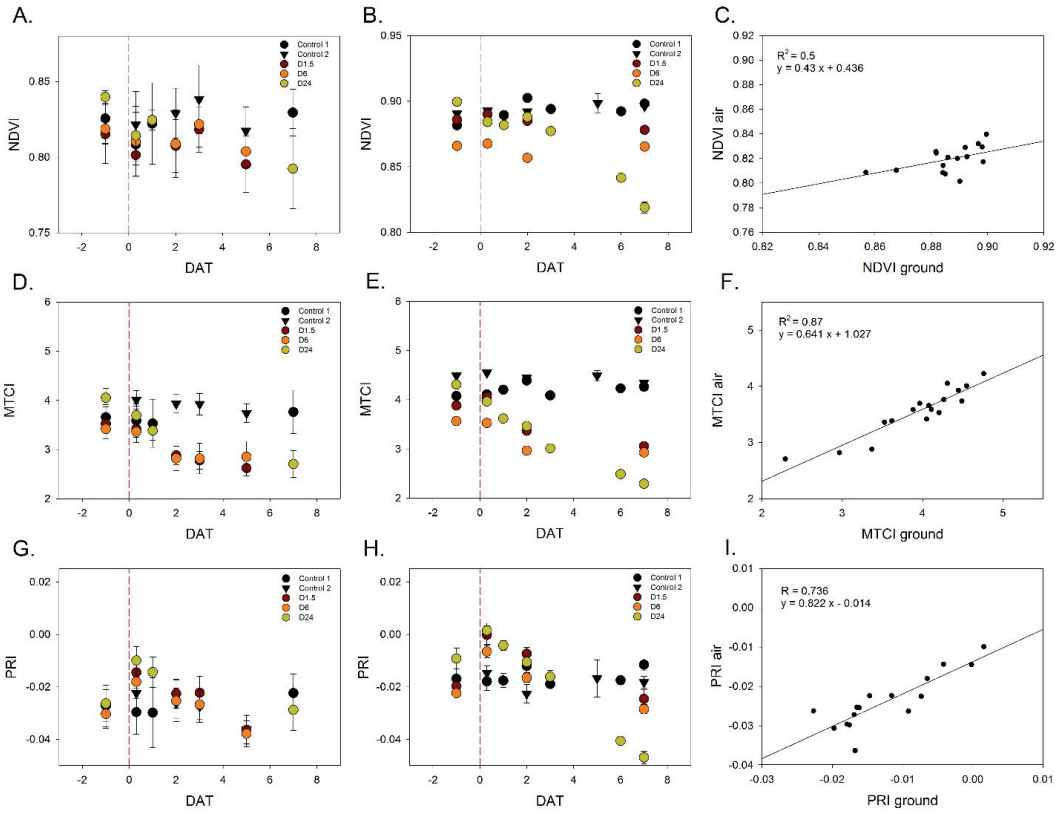

Figure 20: Dynamic changes of vegetation indices during the experiment for all the plots estimated from airborne data (A, D and G) and ground based measurements (B, E and H). Temporal trends of NDVI (A and B), MTCI (D and E) and PRI (G and H). Correlation between airborne and ground observations for NDVI (C), MTCI (F) and PRI (I). Data obtained before DAT −2 were not included for clarity of the results.

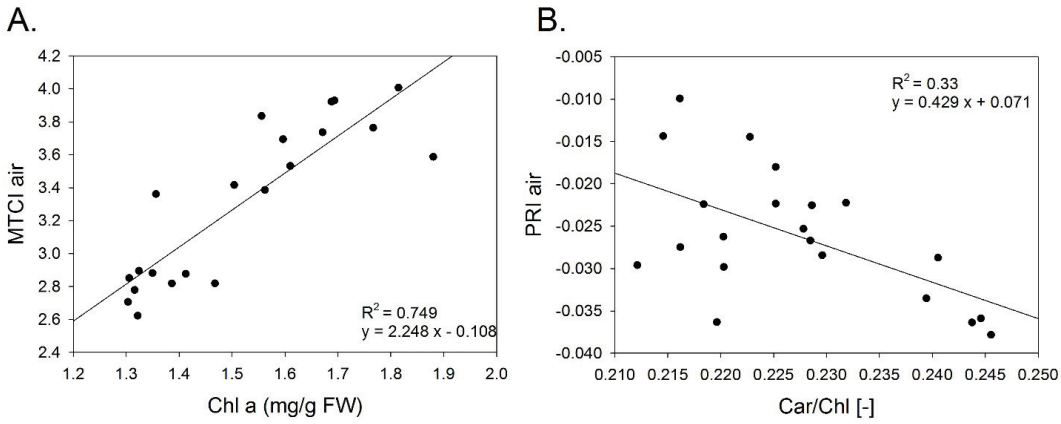

Figure 21: Relationship between the concentration of Chl a and the MTCI (A) and between the ratio Carontenoids/Chlorophyll (Car/Chl) and the PRI (B). The MTCI and PRI were estimated from the spectral reflectance measured with the airborne DUAL module. Data points represent the measurements of all plots for all the dates where airborne data coincided with leaf sampling.

plots after the application. In plot D24, $Fy^{*}{}^{690}_{lob}$ and Fy^{*}_{760} increased nearly 50% and 90%, respectively, only few hours after the herbicide was sprayed (Figs. 21 and 23). Consistently, ground-based measurements detected for the same plot an increase of 146% and 121%, respectively. In the following day, the fluorescence in plot D24 dropped at a fast rate and by DAT 7 the magnitude of Fy^{*} was similar to the initial pre-treatment values. Although the fluorescence dynamics in plots D6 and D1.5 followed a similar trend as in D24, some relevant differences were detected. First, both plots showed lower peaks for Fy^{*}_{687} and Fy^{*}_{760} than in plot D24. Secondly, the rate of Fy^{*}_{687} recovery was lower in the ground-based data than in the aerial data. However, it is important to consider that both systems measured over different areas and that the retrieval of fluorescence at 687 nm is prone to noise due to the shallower O_2-B band. All this can result in inconsistencies between the data from the two platforms. Despite of these limitations, the correlation between ground and aerial data was high (Figs. 23C and 23F), with coefficients of determination of 0.43 and 0.75 ($p < 0.05$) for F_{687} and F_{760}, respectively. A peculiar difference could be observed between the kinetics of Fy^{*}_{687} and Fy^{*}_{760} measured in D1.5 and D6. While in both treatments the Fy^{*}_{687} reached a peak the same day of the application, the maximum Fy^{*}_{760} occurred only 2 to 3 days after the treatment (Figs. 23A, 23B, 23D and 23E). This difference becomes more evident when comparing changes in fluorescence and PRI (Fig. 24). The peak of PRI coincided with the peak of Fy^{*}_{687}, but in the following days Fy^{*}_{760} continued increasing (at a lower rate) despite the drop of PRI.

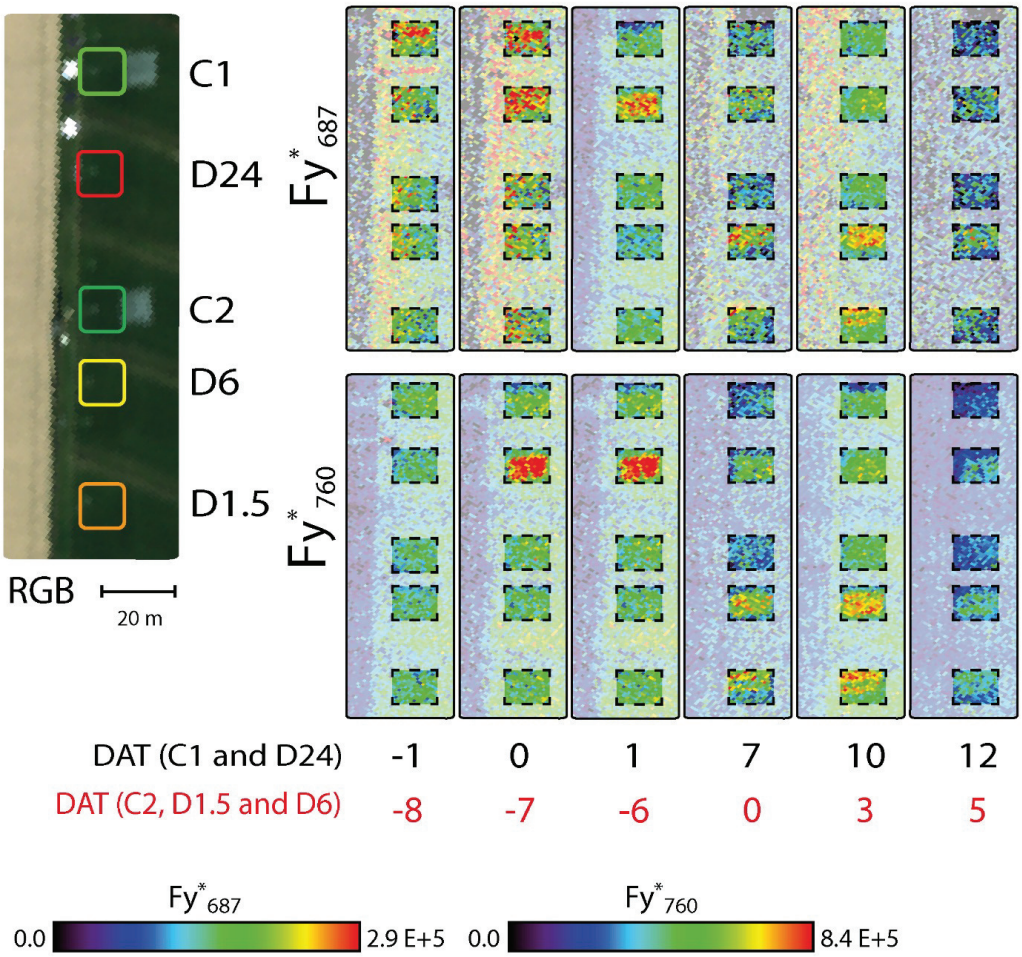

Figure 22: Representation of airborne images showing the dynamics of fluorescence at 687 nm (A: F_{687}) and at 760 nm (B: F_{760}) for each plot. Time is expressed in days after treatment (DAT), where DAT 0 represents the day of the application.

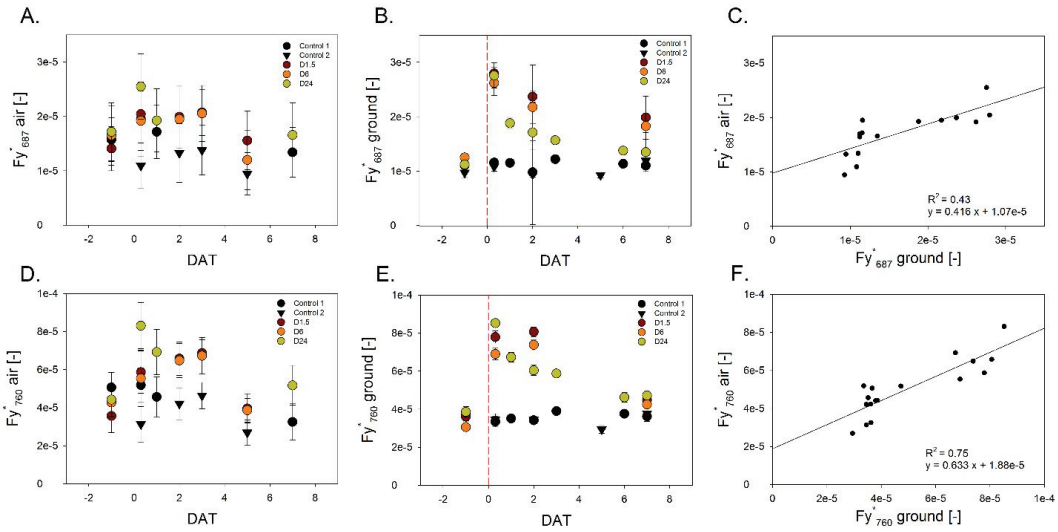

Figure 23: Dynamic changes of fluorescence during the experiment for all the plots estimated from airborne data (A and D) and ground based measurements (B and E). Fy^*_{687} (A and B) and Fy^*_{760} (D and E). Correlation between airborne and ground observations for Fy^*_{687} (C) and Fy^*_{760} (F). Data obtained before DAT −2 were not included for clarity of the results.

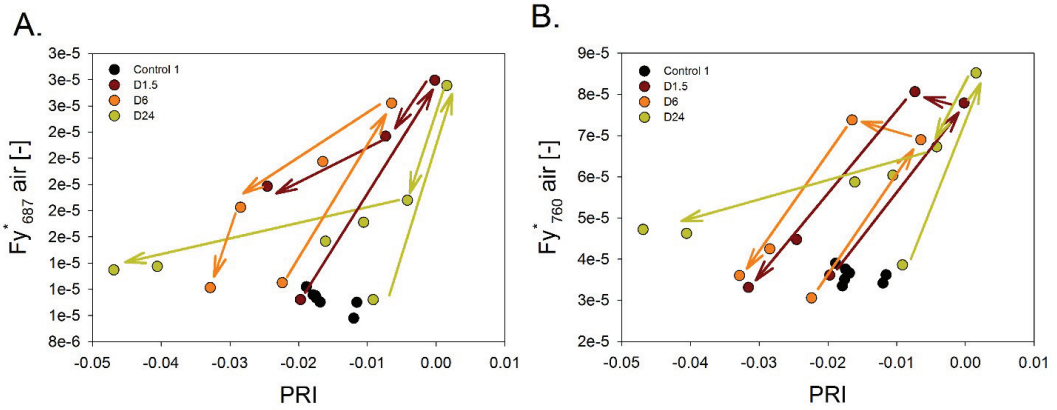

Figure 24: Relationship in time between PRI and the solar-induced fluorescence apparent yield at 687 nm (Fy^*_{687}) and 760 nm (Fy^*_{760}). The arrows indicate the time series and trends of the measurements in each plot.

3.4 DISCUSSION

In this study, we aimed to contribute to the understanding of the relationship between solar-induced chlorophyll fluorescence and photosynthesis under stress conditions. Short-term induced alterations of photosynthesis functioning in grass resulted in quick changes of Fy^* that were detected by the ground-based and airborne platforms. These changes resulted from alterations in various physiological and biophysical processes produced by the herbicide and that were detected by the ancillary remote sensing parameters. Thus, the information on the changes in the pigment composition, the activity of non-photochemical energy dissipation mechanisms (NPQ) and the canopy temperature, represented excellent complements to improve the understanding of the functional interplay of photosynthetic regulation and facilitate the interpretation of the dynamics observed in the fluorescence signal.

The use of Dicuran as stressor permitted to have a quick and well-characterized effect in the photosynthetic apparatus. Dicuran is an herbicide that blocks the binding site of Plastoquinone A in the photosystem II (PSII) and therefore inhibits the photosynthetic electron transport towards the photosystem I (PSI) (Rossini et al., 2015a; Schreiber, 1986; Van Rensen, 1989). The conditions created after its application are suitable for the analysis of the fluorescence behavior in relation to biochemical and biophysical changes in the photosynthetic apparatus. Other stress factors that may occur under natural environmental conditions generally induce a different response of fluorescence emission. Natural stress factors induce a reduction of photosynthetic efficiency but typically increase the NPQ resulting in a decline in fluorescence emission. An exception is the stress induced by cold temperatures, where NPQ activity can drastically be reduced, thus inducing a raise in fluorescence. Despite of the differences that might exist between the action of Dicuran and natural stressors, some of the alterations in the processes involved in photosynthesis are comparable.

The photochemistry was effectively blocked by the Dicuran as demonstrated by the rapid reduction of CO_2 assimilation rates and LUE. Moreover, the increase of canopy temperature suggests that treated plants closed their stomata the days following the application. Hence, the fast increase of Fy^* observed after the application of Dicuran can be attributed to the sudden inhibition of the electron transport chain. The variations in solar-induced fluorescence after the peak and differences between the treatments may be attributed to the subsequent re-distribution of energy in the available dissipation pathways. The differences in GPP, LUE, ΔT and Fy^* observed between the treatments immediately after the application of Dicuran denoted a higher degree of photosynthesis inhibition with increasing concentrations of the herbicide. The gradual decrease of Fy^* observed after the peak and

toward the end of the experiment can be partly explained by a degradation of chlorophyll molecules as suggested by the drop in MTCI during this time. This reduction in the chlorophyll content may be a direct consequence of a photodamage and part of the photoprotective mechanisms to reduce the absorbed radiation (Osmond, 1994). It is worth highlighting the higher sensitivity that MTCI showed to changes in chlorophyll content in contrast to the NDVI. Given the dense canopy of the grass were the experiments were performed, it is likely that the NDVI was close to saturation and therefore rather insensitive to small changes in pigment composition.

The PRI has been reported to be a good estimator of NPQ (Gamon, Peñuelas, and Field, 1992; Panigada et al., 2014; Schickling et al., 2016). However, it is also sensible to changes in the content of pigments in leaves, in particular to the ratio Car/Chl (Garbulsky et al., 2011; Panigada et al., 2009). We attribute the initial peak of PRI to changes in NPQ activity. Under optimal conditions, the PRI decreases towards midday because of the activation of the xanthophyll cycle, a major component of the NPQ (Muller, 2001). A similar tendency was observed in a diurnal sequence of airborne data acquired during this field campaign (data not shown). Therefore, the high PRI observed in treated plots at midday suggests a partial or full inhibition of the NPQ. This is in agreement with Gamon et al. (1990), who observed that DCMU (with a similar mechanism of action as Dicuran) had an inhibitory effect over the violaxanthin de-epoxidation through the avoidance of the protonation of the thylakoid lumen, and consequently reflectance at 531 nm did not vary. This partial inhibition of the NPQ would contribute to the raise of fluorescence immediately after the treatment. Furthermore, the lower peaks of PRI observed in lower doses treatments suggest only a partial inhibition of the NPQ. This would partly explain the lower peaks observed for Fy^*_{687} and Fy^*_{760} in these plots. The later decay of PRI in all treatments might be related to an activation of the NPQ, which in turn would be responsible to quench the fluorescence emission as observed in the following days after the peaks. This could also explain the partial recover of GPP observed at this time, suggesting an eventual reversible effect of the Dicuran. However, it is worth mentioning that other factors could affect the GPP estimation at this point. We observed an increase of canopy respiration that may be related to an upregulated use of plants' carbohydrate reserves, which is likely to occur under stressful conditions. This increase of respiration do not necessarily mean an increase of photosynthesis. The continuous decrease of NEE and the transpiration rate within days support this interpretation. However, the correct quantitative interpretation of respiration rates for the precise calculation of GPP is error prone and we thus do not want to overinterpret these findings. Under this scenario, the decrease of fluorescence yield and PRI after their peaks could be better explained by the pigment degradation inferred from NDVI and MTCI mea-

surements and confirmed by the laboratory measurements. In our measurement, nearly 40% of the variation of PRI was explained by changes in the Car/Chl relationship confirming the findings of Panigada et al. (2009). A decrease of this ratio driven by the degradation of chlorophyll would result in a lower PRI. Likewise, the emission of fluorescence would be reduced in all wavelengths due to a lower absorption of PAR.

The differences between the kinetics of Fy^*_{687} and Fy^*_{760} can provide valuable information to elucidate at which level the stress is affecting photosynthesis. In this experiment we observed that in the lower doses treatments the initial rise of Fy^*_{687} was quenched faster than Fy^*_{760}. This quick decrease of Fy^*_{687} coincides with the drop of PRI and thus can be attributed to the combined action of NPQ and the degradation of chlorophyll. In the case of Fy^*_{760}, the peak was observed after the PRI started to decrease. One reason for this can be that the Dicuran action affects directly the short-term regulatory mechanisms of light harvesting in the PSII, where the F_{687} originates. Hence, any evolution of the stress would modulate this signal almost instantaneously. On the other hand, F_{760} is emitted by both photosystems. Therefore, the fraction of F_{760} emitted from the less regulated PSI would respond slower to adaptation mechanisms. Further analyzes in this respect escape from the scope of this study. However, we acknowledge the importance of studying further the different response of F_{687} and F_{760} to the action of various stresses.

The set of parameters measured during this study demonstrated to provide relevant information that can be used to describe changes in a series of related processes that ultimately impact the functioning of photosynthesis and that ultimately govern photosynthetic CO_2 uptake. The following conceptual model can be derived from our results. The sudden increase of solar-induced fluorescence yield reflects the immediate inhibition of the photosynthetic electron transport in light reactions. Additionally, non-photochemical mechanisms for energy dissipation were inhibited as suggested by the quick changes in PRI. This makes the photosynthetic apparatus susceptible to photodamage. A degradation of chlorophyll took place almost immediately because of the excess of energy as well as part of the strategy to reduce the absorbed radiation. At the same time, the blockage of the photosynthetic light reactions ceased the reduction of NADP+ to NADPH and the formation of ATP, which results in an almost complete downregulation of CO_2 fixation by Rubisco, which is clearly reflected in a drop of carbon assimilation detected by our gas exchange measurements. Consequently, the stomata closed to avoid water loss inducing an increase of the canopy temperature (as suggested by the decrease of the transpiration rates). In the following days, the gradual decline of chlorophyll content (inferred from the changes in MTCI) and a partial re-activation of the NPQ quenched the fluorescence signal. Although the

GPP data showed some signs of recovery in some of the treated plots, the drastic drop of fluorescence yield and PRI towards the end of the experiment were better explained by a long-term breakdown of chlorophyll and possibly to an irreversible damage in the photosynthetic apparatus. Indeed, by the end of the experiment the plants treated with the highest dose were killed by the action of the herbicide.

3.5 CONCLUSIONS

In this experimental study, we explored the use of solar-induced chlorophyll fluorescence as a proxy to detect stress-induced limitations in photosynthetic activity at canopy level. The use of the herbicide Dicuran permitted to simulate a stress event that triggered changes in different components of the photosynthetic apparatus. We showed that no measurement parameter alone was sufficient to reflect the dynamic changes of CO_2 uptake rate. Both fluorescence measured at 687 nm and 760 nm could clearly track functional impairments of photosynthetic electron transport rate and thus is the superior remote sensing indicator for tracking acute limitation of actual photosynthesis. However, longer term adaptation of the photosynthetic apparatus involve a complex interplay of optimizing photosynthetic efficiency at PSII, the different pathways of non-photochemical energy dissipation, a balanced stomatal regulation and the breakdown and repair of pigments. The measurement of all these components is therefore necessary in the design of a forward model to unravel the mechanism of action of a stressor, and to estimate photosynthetic CO_2 uptake rates and GPP. The FLEX satellite mission is designed to provide all necessary input parameters for the development of such a model. Based on the results of this and other studies, we propose that the following parameters are relevant to constrain a forward estimation of photosynthetic carbon uptake: (i) the efficiency of photosynthetic electron transport (approximated by fluorescence emission), (ii) the degree of non-photochemical energy dissipation (estimated by reflectance changes in the green spectral range), (iii) the amount and composition of photosynthetic pigments (measured by canopy reflectance and improved by fluorescence measures), and finally (iv) an estimate of stomatal opening (as assessed by canopy temperature).

4 EXPLORING THE PHYSIOLOGICAL INFORMATION OF SOLAR-INDUCED CHLOROPHYLL FLUORESCENCE THROUGH RADIATIVE TRANSFER MODEL INVERSION

ABSTRACT

[1] The combined retrieval of vegetation biochemical and biophysical parameters and chlorophyll a fluorescence (F) was investigated exploiting high resolution spectral measurements in the visible and near-infrared spectral regions. A numerical inversion of the radiative transfer modules for fluorescence and reflectance of the "Soil-Canopy Observation Photosynthesis and Energy fluxes" (SCOPE) model was performed. First, the retrieval scheme was validated on a synthetic dataset generated with the SCOPE model, varying the main parameters over a wide range of possible values. Then, it was applied to very high resolution (sub-nanometer) canopy level spectral measurements collected over a lawn treated with different doses of a herbicide (Dicuran) known to instantaneously inhibit both Photochemical and Non-Photochemical Quenching (PQ and NPQ, respectively). As a reference, F values obtained with the model inversion were compared to those retrieved with state of the art Spectral Fitting Methods (SFM) and SpecFit retrieval algorithms. For the first time the full spectrum of canopy F, the fluorescence emission efficiency (Φ_F), as well as the main vegetation parameters that control light absorption and reabsorption, were retrieved concurrently using canopy-level high resolution apparent reflectance (ρ^*) spectra. The effects of pigment content, leaf/canopy structural properties and physiology were effectively discriminated. Their combined observation over time led to the recognition of dynamic patterns of stress adaptation and stress recovery. Φ_F retrieved from ρ^* was eventually com-

1 The content of this chapter has been submitted to *Remote Sensing of Environment* as Celesti, M., van der Tol, C., Cogliati, S., Panigadaa, C., Yang, P., Pinto, F., Rascher, U., Miglietta, F., Colombo, R., Rossini, M. "Exploring the physiological information of solar-induced chlorophyll fluorescence through radiative transfer model inversion", and it is currently under review.

pared with an independent biophysical model of photosynthesis and fluorescence. These results foster the use of repeated hyperspectral remote sensing observations together with radiative transfer and biochemical models for plant status monitoring.

Keywords: solar-induced chlorophyll fluorescence, fluorescence quantum efficiency, SCOPE, numerical optimization, plant status

4.1 INTRODUCTION

In the last years, Remote Sensing (RS) of chlorophyll a fluorescence (F) emerged as a novel and promising scientific field for studying the dynamic behavior of photosynthesis (for a review of this topic see Meroni et al., 2009 and Porcar-Castell et al., 2014). F is a physical side product of light absorption that is emitted as an electromagnetic radiation in the red and far-red spectral regions ($\approx$ 640–850 nm), and it is related to the energetic status of the photosystems. The FLuorescence EXplorer (FLEX) mission, selected as the 8th *Earth Explorer* of the European Space Agency (ESA) and planned for launch in 2022, is the first satellite mission specifically designed and optimized for fluorescence observation from space. One of the main goals of the FLEX mission will be to retrieve F using the spectral features in the oxygen A (O_2-A; centered at 760.4 nm) and B (O_2-B; centered at 687.0 nm) absorption bands, as well as the full spectrum of emitted fluorescence. The feasibility of consistent retrieval of F from ground based, airborne and satellite platforms has been investigated in the last years (Cogliati et al., 2015; Guanter et al., 2015, 2010; Meroni et al., 2008; Migliavacca et al., 2017; Rascher et al., 2015; Rossini et al., 2015; Rossini et al., 2016; Yang et al., 2015). Nevertheless, due to the concurrent influence of physiology, leaf and canopy structure, pigment concentration and weather conditions on F (Porcar-Castell et al., 2014; Verrelst et al., 2015b), it's unambiguous interpretation in terms of the quantification of vegetation photosynthesis and stress detection is a largely unsolved challenge. Several authors (*e.g.*, Damm et al., 2010; Guanter et al., 2014; Lee et al., 2013) exploited the conceptual scheme of the Light Use Efficiency (LUE) model, proposed by Monteith (1972) for the Gross Primary Production (GPP), to express F as:

$$F(\lambda) = PAR \times fAPAR \times Fy(\lambda) \times f_{esc}(\lambda) \tag{17}$$

where PAR is the Photosynthetically Active Radiation, fAPAR is the fraction of PAR that is absorbed by vegetation (*i.e.*, the fraction of PAR that is transformed into Absorbed Photosynthetically Active Radiation (APAR)), Fy is the fluorescence yield (*i.e.*, the fraction of absorbed radiation emitted as fluorescence), and $f_{esc}(\lambda)$

the "escape probability" (the probability that an emitted fluorescence photon escapes the canopy in the direction of the sensor). These three processes together (*i.e.*, the absorption of light, the emission as fluorescence, and the escape of F from the canopy) determine the directional F flux emitted at the top of the canopy. Given these definitions, the fluorescence emitted by all leaves at a wavelength λ ($F^{TOT}(\lambda)$) can be defined as the ratio of $F(\lambda)$ and $f_{esc}(\lambda)$, and integrated over all wavelengths of the spectrum of emitted fluorescence to obtain the total emitted fluorescence by all photosystems (F_{int}^{TOT}; Eq. 18).

$$F_{int}^{TOT} = \int_{640}^{850} \frac{F(\lambda)}{f_{esc}(\lambda)} d\lambda \tag{18}$$

After substitution of $APAR = fAPAR \times PAR$ in Eq. 17, and after converting APAR and F_{int}^{TOT} from energy units to quanta using the Planck's constant, the fluorescence quantum yield (Φ_F) at photosystem level can be defined as:

$$\Phi_F = \frac{F_{int}^{TOT}}{APAR} \tag{19}$$

Φ_F is modulated by changes in the physiological status of plants, and represents the fraction of absorbed quanta that is not used for Photochemical Quenching (PQ) and Non-Photochemical Quenching (NPQ). In photosynthesic studies it is practical to use quantum yields for describing the quantum efficiency of the involved processes, and another common way to represent these dissipation pathways is by using rate coefficients K (Butler, 1978; Eq. 20).

$$\Phi_F = \frac{K_F}{K_F + K_D + K_N + K_P} \tag{20}$$

where K_F, K_D, K_N and K_P are the relative rate constants for fluorescence, constitutive thermal dissipation, NPQ and PQ, respectively (cfr. Porcar-Castell 2011). It is also valid that the sum of the quantum yields (Φ) is equal to 1 (Eq. 21).

$$\Phi_F + \Phi_D + \Phi_N + \Phi_P = 1 \tag{21}$$

Given this energy balance formulation, it is clear that any variation in Φ_F reflects variations in one or more of the other Φ, and consequently in one or more of the other processes. Although the potential of Φ_F to monitor photosynthesis has been demonstrated, it is not trivial to quantify it from canopy level measurements, with increasing complexity when moving from field to airborne and satellite observations. In particular: i) the calculation of F_{int}^{TOT} (Eq. 18) requires the retrieval of the full spectrum of emitted F, but only few attempts have been made so far to retrieve it at canopy level from ground measurements (Liu et al., 2015; Zhao

et al., 2014), airborne (Cogliati et al., 2016) or simulated satellite data (Cogliati et al., 2015; Sabater et al., 2015); ii) it is not possible to directly measure f_{esc}; iii) the proper quantification of the components of APAR from RS is still challenging (cfr. Garbulsky et al., 2010; Gitelson and Gamon, 2015). Apart from ground or near ground measurements, any retrieval of PAR or fAPAR from RS platforms is mediated by a model, and the disagreement between currently available fAPAR products is high (Meroni et al., 2013; Pickett-Heaps et al., 2014).

Physically-based Radiative Transfer Models (RTMs) of the vegetation have been used in the last decades to express mathematically the complex interactions between plant elements (*e.g.*, tissues, leaves, branches) and the electromagnetic radiation. Verrelst et al. (2015a) pointed out that the quantification of surface biogeophysical variables is inherently model-dependent, because models bridge the gap between RS observations and the physical processes and surface properties that drive them. Some of these models also include interactions with the soil and the atmosphere (Verhoef and Bach, 2003, 2007). In addition to that, Soil-Vegetation-Atmosphere Transfer (SVAT) models (*e.g.*, Sellers, 1997; van der Tol et al., 2009; Verhoef and Allen, 2000) have been proposed to describe the pathways of energy, carbon and water between soil, vegetation and atmosphere. Among these, the 1-D (vertical) "Soil-Canopy Observation Photosynthesis and Energy fluxes" (SCOPE) model (van der Tol et al., 2009) is an integrated radiative transfer and energy balance model that enables the simulation of canopy leaving hyperspectral reflectance and fluorescence, as well as the turbulent heat fluxes and photosynthesis. van der Tol et al. (2016) successfully exploited high resolution (Spectral Sampling Interval (SSI) = 0.24 nm and Full Width at Half Maximum (FWHM) = 1 nm) top-of-canopy reflectance spectra in the Visible and Near InfraRed (VNIR) spectral region, to partially invert SCOPE and retrieve biochemical and structural parameters of the vegetation (*e.g.*, pigment concentration, canopy structure), and simulate emitted F_{760}. Recently, Hernández-Clemente et al. (2017), Liu et al. (2017), and Zhao et al. (2016) extended 3-D radiative transfer models to simulate F in complex canopies. In particular, Hernández-Clemente et al. (2017) used FluorFLIGHT to account for the effects of sunlit/shadow pixels, vegetation structure and fractional cover on F in an oak forest, highlighting the importance of a proper modeling approach to relate F to forest health. Nevertheless, these models are generally slower and require a larger number of input parameters than simpler 1-D RTMs, and this can be a limiting factor for their large-scale application.

In this work we propose a novel approach to characterize the physiological conditions of plants from hyperspectral RS data. In particular, the specific objectives of this work are: i) to propose and validate a method to invert a "light" version of the SCOPE model, retrieving concurrently F, Φ_F and the main biochemical and biophysical parameters of the vegetation that control APAR; ii) to compare the

retrieved F values with state of the art SFM and SpecFit algorithms; iii) to analyze the temporal evolution of the retrieved parameters in a controlled stress experiment; iv) to compare the retrieved Φ_F values with an independent biochemical model of photosynthesis and fluorescence (van der Tol et al., 2014).

4.2 MATERIALS AND METHODS

4.2.1 Experimental setup

The field campaign was conducted in a farm in Latisana (Udine, Italy; 13.013E, 45.779N) from 7th June 2014 to 3rd July 2014, during the ESA founded FLEX-EU campaign (cfr. Section 3.2). Three parcels ($9\,m \times 12\,m$) of a commercially produced lawn were treated with increasing doses of Dicuran 700 FW (Syngenta AG), a commercial formulation of Chlorotoluron (3-(3-chloro-p-tolyl)-1,1-dimethylurea). Dicuran is an herbicide that interferes with the light reactions of photosynthesis, inhibiting the electron transport chain from photosystem II (PSII) to photosystem I (PSI). This translates in a strong decrease of PQ, and in an accumulation of absorbed energy inside the reaction centers that has to be rapidly dissipated to avoid oxidative stress. Dicuran is also known to inhibit NPQ, hence we expect a strong increase of Φ_F, driven by an increase in F emission, after the treatment. On the other hand, the vegetation biophysical and biochemical parameters should only be influenced at a later stage. Three additional non-treated plots were sprayed with water and used as control. A similar treatment was exploited in Rossini et al. (2015), with noticeable effects on both F_{687} and F_{760}. The lawn was frequently irrigated during the campaign and was expected to never experience water limited conditions. A preliminary assessment of the full dataset (cfr. Chapter 3) showed i) no differences in the dynamics of the control plots, and ii) that the effect on F and reflectance of the two lower doses of Dicuran was comparable. Hence, for the sake of simplicity, data shown in this paper refer only to three plots, representative of the more (maximum dose, $24\,ml\,l^{-1}$) and less stressed (minimum dose, $1.5\,ml\,l^{-1}$) among the treated plots, as well as a control plot. Due to logistic constraints, the herbicide was applied on the two plots seven days apart (12th June 2014 and 19th June 2014, respectively) hence in this paper the Days After Treatment (DAT), instead of the Day Of the Year (DOY) will be used.

4.2.2 Top-of-canopy hyperspectral measurements

High resolution spectral measurements were performed in the field with three Ocean Optics (Dunedin, USA) portable spectrometers operating in the Visible and Near InfraRed (VNIR) spectral region with different spectral configurations (Table 6). The spectrometers were housed in a Peltier thermally regulated box (model NT-16, Magapor, Zaragoza, Spain) keeping the internal temperature at 25 °C in order to ensure the stability of both the intensity and the spectral information of the measured signal. The targets were measured from nadir with bare optical fibers (field of view of 25°) at a distance of 1.30 m, yielding to an observed circular surface of approximately 0.58 m of diameter. The fibers were mounted downlooking on a specially modified tripod that allowed the alternate measurement of the vegetated target and of the white reference calibrated panel (Labsphere Inc., North Sutton, NH, USA). A picture of the overall spectroscopic measurements setup is reported in Figure 25a. This system has been widely used in the last decade to provide consistent values of reflectance and fluorescence in different field campaigns, over a wide range of crops and natural vegetation (Rossini et al., 2016). The spectral data were acquired with a dedicated software (3S; Meroni and Colombo, 2009) and processed with a specifically developed IDL (ITTVIS IDL 7.1.1) application described in Meroni et al., 2011. Each acquisition consisted of three spectra recorded sequentially: L_{in}^{meas} measured over the calibrated white reference panel, L_{out}^{meas} over the target and L_{in}^{meas} again. The actual L_{in}^{meas} at the time of the target measurement was estimated by linear interpolation. The relative variation of the two L_{in}^{meas} measurements was used as a quality check for illumination condition stability (*i.e.*, total variation below 5%). Each of these spectra is the average of 10 and 3 scans (for the full range and the other two spectrometers, respectively) in order to reduce instrumental noise.

Table 6: Summary of the technical characteristics of the Ocean Optics spectrometers (Dunedin, USA) used in the measurement campaign. "Range" is the spectral range, "SSI" is the Spectral Sampling Interval, "FWHM" is the "Full Width at Half Maximum" and "SNR" is the nominal Signal-to-Noise Ratio.

ID	Model	Range [nm]	SSI [nm]	FWHM [nm]	SNR
S-Full	HR4000	400-1000	0.24	1.00	300:1
S-O_2-B	QE65000	657-743	0.10	0.25	1000:1
S-O_2-A	HR4000	717-805	0.02	0.10	300:1

Figure 25b shows a nadiral picture of one of the measured lawn parcel. A white frame was used as a reference to ensure spatially consistent measurements of the vegetated surface (depicted approximately with the yellow circle) over time. To ensure that the white frame had no effect on the measurements (*i.e.*, signal contamination due to adjacency effects), two consecutive measurements with and without the frame were compared, showing no significant differences in terms of reflectance and fluorescence (data not shown). Ground measurements were performed over the whole time window of the campaign. Measurements started around 10:00 until 16:00 (CEST), depending on the weather conditions. The plots were measured moving the instruments from the first to the last plot cyclically during the day. Five consecutive acquisitions were taken for each plot under stable illumination conditions before moving to the next one. The final spectral dataset consisted of $\approx$ 600 measurements. The spectra collected with the three spectrometers were converted from digital numbers to radiance and then merged together in order to cover the VNIR spectrum (400-900 nm) with the maximum possible spectral resolution (*i.e.*, minimum SSI and FWHM). In this work, in fact, in order to retrieve concurrently the biophysical parameters by model inversion technique, the F_{687} and F_{760} at the oxygen absorption bands, as well as the full spectrum F, the spectra collected with the highest spectral resolution spectrometers (S-O_2-B and S-O_2-A) were accurately inter-calibrated based on the lower resolution spectrometer (S-Full), and merged together to obtain a single spectrum with the highest possible resolution (Figure 26). Top-of-canopy solar-induced fluorescence was retrieved in the O_2-A and O_2-B oxygen absorption bands using state of the art Spectral Fitting Methods (SFM) (Cogliati et al., 2015), originally proposed by Meroni and Colombo (2006) and Meroni et al. (2010). This method models the fluorescence emission and the *true* reflectance (ρ^{SFM}; *i.e.*, the ratio of the reflected radiance and the incoming radiance) as a function of wavelengths inside the O_2-A and O_2-B oxygen absorption bands. F^{SFM} and ρ^{SFM} were modeled using Voigt functions and piecewise cubic splines, respectively. Moreover, the SpecFit algorithm as described in Cogliati et al. (2015) was applied to retrieve the full spectrum of the F emission ($F^{SpecFit}$) in the spectral range from 670–780 nm. The integral of each F spectrum ($F_{int}^{SpecFit}$) was computed by means of trapezoidal numerical integration.

Starting from the measured radiance fluxes, the measured *apparent* reflectance ($\rho^{*,meas}$) was computed. $\rho^{*,meas}$ is a quantity defined as the ratio between the radiance leaving the vegetation surface ($L_{out}{}^{meas}$) and the incoming radiance ($L_{in}{}^{meas}$). It differs from the *true* reflectance (ρ) for including not only the reflected, but also the emitted radiance (*i.e.*, the fluorescence).

(a) (b)

Figure 25: a) Picture of the spectroscopic setup in the field; b) Parcel of the measured lawn: the yellow circle is approximately the area measured with the spectroscopic system.

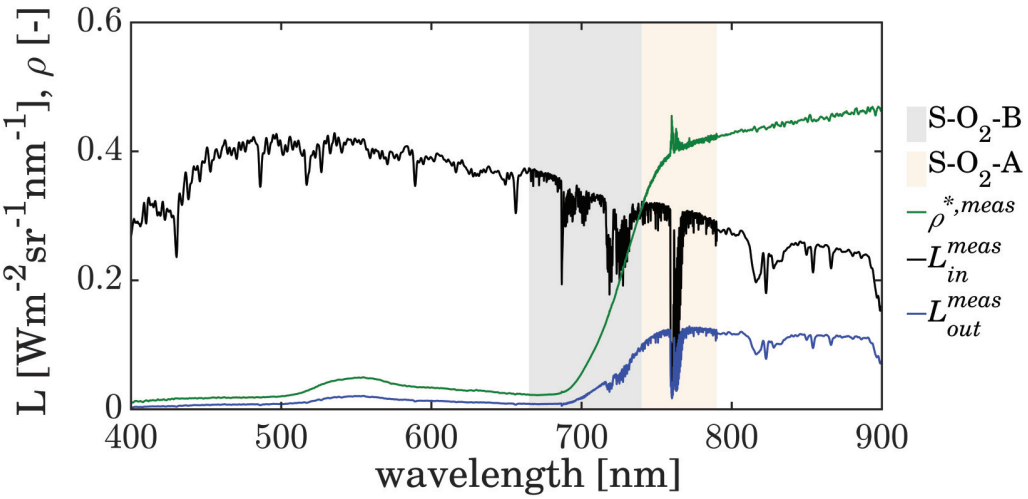

Figure 26: Example of the spectra collected with the three spectrometers merged together to obtain the highest resolution spectral configuration. The shaded area represents the regions where the data from the high resolution spectrometers (S-O_2-B and S-O_2-A) were used instead of the full-range one (S-Full).

4.2.3 Modeling setup

MODEL DESCRIPTION The Radiative Transfer (RT) routines used to simulate reflectance and fluorescence were taken from the SCOPE model (version 1.70[2]). Four routines were selected for this purpose. At leaf level, reflectance and fluorescence spectra were simulated with a modified version of the Fluspect-B model (Verhoef, 2011; Vilfan et al., 2016), while for propagation through the canopy the routines RTMo for incident light and RTMf for fluorescence were used. Fluspect-B is based on the PROSPECT model (Jacquemoud and Baret, 1990), with the addition of backward and forward fluorescence spectra. Here, the absorption coefficients of leaf biochemical components from the recently published PROSPECT-D (Féret et al., 2017) were used. RTMo is based on the SAIL model (Verhoef, 1984), and it simulates the four-stream radiative transfer of the incident light, resulting in the reflectance. Finally, RTMf propagates the fluorescence fluxes simulated by Fluspect-B inside the canopy based on the distribution of APAR and the scattering coefficients modeled with RTMo. The soil reflectance was modeled using the "Global Soil Vector" (GSV) model (Jiang and Hongliang, 2012; Verhoef, Tol, and Middleton, 2014). The coupled model resulting from the combination of Fluspect-B, RTMo, RTMf and GSV is a "light" version of SCOPE, and it is referred to as "RTMc" in this study.

MODEL INVERSION The model inversion routine for the retrieval of biophysical and biochemical parameters of the vegetation was based on a Numerical Optimization (NO) algorithm that minimizes the differences between the measured and the modeled apparent reflectance in the spectral region from 400–900 nm. The modeled apparent reflectance ($\rho^{*,RTM}$) is defined by the ratio of the modeled radiance leaving the vegetation surface (L_{out}^{RTM}) and the incoming radiance:

$$\rho^{*,RTM} = \frac{L_{refl}^{RTM} + F_{out}^{RTM}}{L_{in}^{meas}} = \frac{L_{out}^{RTM}}{L_{in}^{meas}} \tag{22}$$

where F_{out}^{RTM} is the modeled fluorescence in the observation direction, and the modeled reflected radiance (L_{refl}^{RTM}) is computed as:

$$L_{refl}^{RTM} = \frac{r_{so}(\pi L_{sun}^{meas}) + r_{do}(\pi L_{sky}^{meas})}{\pi} \tag{23}$$

where r_{so} and r_{do} are the canopy reflectance factors of the direct (solar) and diffuse (sky) components of the incoming irradiance (πL_{sun}^{meas} and πL_{sky}^{meas}, respectively). L_{sun}^{meas} and L_{sky}^{meas} were not directly measured in the field, but were

2 https://github.com/Christiaanvandertol/SCOPE.git

obtained by decomposing L_{in}^{meas} according to a simulation produced with the MODerate resolution atmospheric TRANsmission (MODTRAN) RT model (Berk et al., 2014), so that the sum of the two components was equal to the measured total $L_{in}{}^{meas}$ (Eq. 24).

$$L_{in}^{meas} = L_{sun}^{meas} + L_{sky}^{meas} \tag{24}$$

An example of the spectra obtained from this decomposition is shown in Figure 27. Given a set of arbitrary starting model parameters (Table 7, column SV), the true solar zenith and azimuth angles, and the L_{sun}^{meas} and L_{sky}^{meas} components, the NO algorithm iteratively executes the RTMc model, varying all the free parameters within their range of variation (Table 7), until a cost function is minimized. A number of parameters were left free to vary during the inversion routine. In

Table 7: Lower boundaries (LB), upper boundaries (UB), *a priori* values (p_0), assumed standard deviations (σ_{p_0}) and starting values (SV) of each retrieved parameter. Free parameters include six Fluspect-B parameters for Chlorophyll (C_{ab}) and carotenoids (C_{car}), leaf dry matter (C_{dm}), water content (C_w) and senescent material (C_s), and fluorescence quantum efficiency (fqe), the Leaf Area Index (LAI) from the SAIL model, and the volumetric soil moisture percentage in the root zone (SMp) from the GSV model.

Parameter	Unit	LB	UB	p_0	σ_{p_0}	SV
C_{ab}	$\mu g\,cm^{-2}$	0	100	40	30	40
C_{car}	$\mu g\,cm^{-2}$	0	30	10	10^9	10
C_{dm}	$g\,cm^{-2}$	0	0.04	0.01	10^9	0.005
C_w	cm	0	0.05	0.01	10^9	0.02
C_s	-	0	0.4	0.15	10^9	0.1
fqe	-	0	1	0.01	10^9	0.01
LAI	$m^2\,m^{-2}$	0	6	2	1	3
SMp	%	5	55	30	10^9	30

particular, six Fluspect-B parameters for chlorophyll (C_{ab}) and carotenoid content (C_{car}), leaf dry matter (C_{dm}), water content (C_w), senescent material (C_s), the fluorescence quantum efficiency (fqe), and the Leaf Area Index (LAI) from the SAIL model. SMp is a parameter in the GSV model for the volumetric soil moisture percentage in the root zone, and it was left free to account for potential variations in the soil brightness due to soil moisture content. The Fluspect-B parameter "fqe" corresponds to the fluorescence emission efficiency (Φ_F) in Eqs. 17, 21. In order to test the retrieval scheme in a generally applicable configuration, the lower (Table 7, column LB) and upper boundaries (column UB) of the free parameters were left

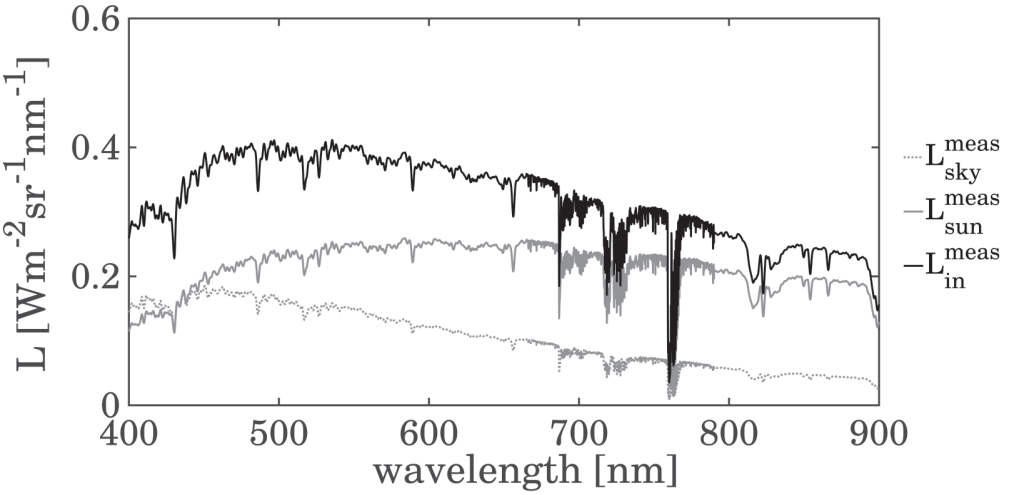

Figure 27: Example of the measured total incoming radiance (L_{in}^{meas}) and the decomposed direct (L_{sun}^{meas}) and diffuse (L_{sky}^{meas}) fluxes.

very wide. A spherical leaf angle distribution (LIDFa = −0.35; LIDFb = −0.15), was chosen to model the lawn canopy. It was left fixed because no variation in the canopy architecture was observed during the campaign.

Following van der Tol et al. (2016), we used the `lsqnonlin` function of the optimization toolbox in MATLAB® R2016b, selecting a Trust-Region-Reflective least squares algorithm for updating parameters after each iteration step. The cost function "f" was defined as:

$$
\begin{aligned}
f &= ER1^T ER1 + w * ER2^T ER2 \qquad (25)\\
ER1 &= \begin{cases} \rho^{*,RTM}(\lambda) - \rho^{*,meas}(\lambda) & ,\lambda \in \lambda_{noabs} \\ (\rho^{*,RTM}(\lambda) - \rho_{BL}^{*,RTM}(\lambda)) + & \\ \quad -(\rho^{*,meas}(\lambda) - \rho_{BL}^{*,meas}(\lambda)) & ,\lambda \in \lambda_{abs} \end{cases}\\
ER2 &= \frac{p - p_0}{\sigma_{p_0}}
\end{aligned}
$$

with λ_{abs} being the spectral ranges within the fluorescence emission region where major atmospheric absorption features occur, in particular:

- O_2-A from 754–775 nm
- O_2-B from 685–688 nm
- H_2O from 715–734 nm

and λ_{noabs} all other wavelengths in the 400–900 nm spectral range. The first term of the cost function (ER1) calculates the residuals between the modeled ($\rho^{*,RTM}$) and the measured apparent reflectance ($\rho^{*,meas}$). Outside the oxygen absorption bands, simply the difference between $\rho^{*,RTM}$ and $\rho^{*,meas}$ is used. However, inside the absorption bands, the apparent reflectance is normalized (subtracted) by a "baseline reflectance" (ρ^{*}_{BL}, the "baseline" of ρ^{*}). This ensures that the heights of the spikes in the apparent reflectance relative to the shoulders outside the absorption bands are reproduced rather than the absolute heights. This appears necessary as the $\rho^{*,RTM}$ may have some residual bias in the red-edge and the Near InfraRed (NIR) plateau, which could strongly affect the retrieved fluorescence. ρ^{*}_{BL} is calculated by fitting a linear spline function to the ρ^{*} curve once the peaks due to F contribution are removed, an approach conceptually similar to the one used in the iFLD fluorescence retrieval (Alonso et al., 2008). ER1 in the absorption bands is then calculated as the difference of the modeled and measured residuals between ρ^{*} and ρ^{*}_{BL}. Figure 28a shows an example of the minuend ($\rho^{*,meas} - \rho^{*,meas}_{BL}$) and the subtrahend ($\rho^{*,RTM} - \rho^{*,RTM}_{BL}$) of ER1 (Eq. 25), in the spectral region around the O_2-A band, while in Figure 28b ER1 computed for the whole dataset is compared to the difference between $\rho^{*,RTM}$ and $\rho^{*,meas}$. The second term (ER2) includes the posterior (p) and *a priori* (p_0) values of the model parameters, as well as their expected standard deviation (σ_p), weighted for a factor $w = 3 \times 10^{-2}$ (van der Tol et al., 2016). The output of this process is an optimized set of the input parameters, as well as the corresponding modeled reflectance and fluorescence spectra (Figure 29). The integral of each F spectrum (F^{RTM}_{int}) was computed by means of trapezoidal numerical integration. In order to be consistent with the calculation of ($F^{SpecFit}_{int}$), the spectral range was limited between 670 and 780 nm.

MODEL VALIDATION In order to test the retrieval algorithms described in the previous section (*i.e.*, RTMc inversion, SFM and SpecFit), we created a large synthetic (> 800 000) look-up table of apparent reflectance spectra with RTMc, with the same spectral characteristics of the measured data. RTMc input parameters were varied over a wide range of possible values (*i.e.*, between LB and UB in Table 7), with a fixed-pass sampling ensuring at least 5 steps for each parameter. In addition, the short-wave incoming radiation (R_{in}) was varied between 400 and 1000 $W\,m^{-2}$ with a 200 $W\,m^{-2}$ step. A subset of randomly selected 1000 simulations was used to perform the inversion and to test the retrieval algorithms.

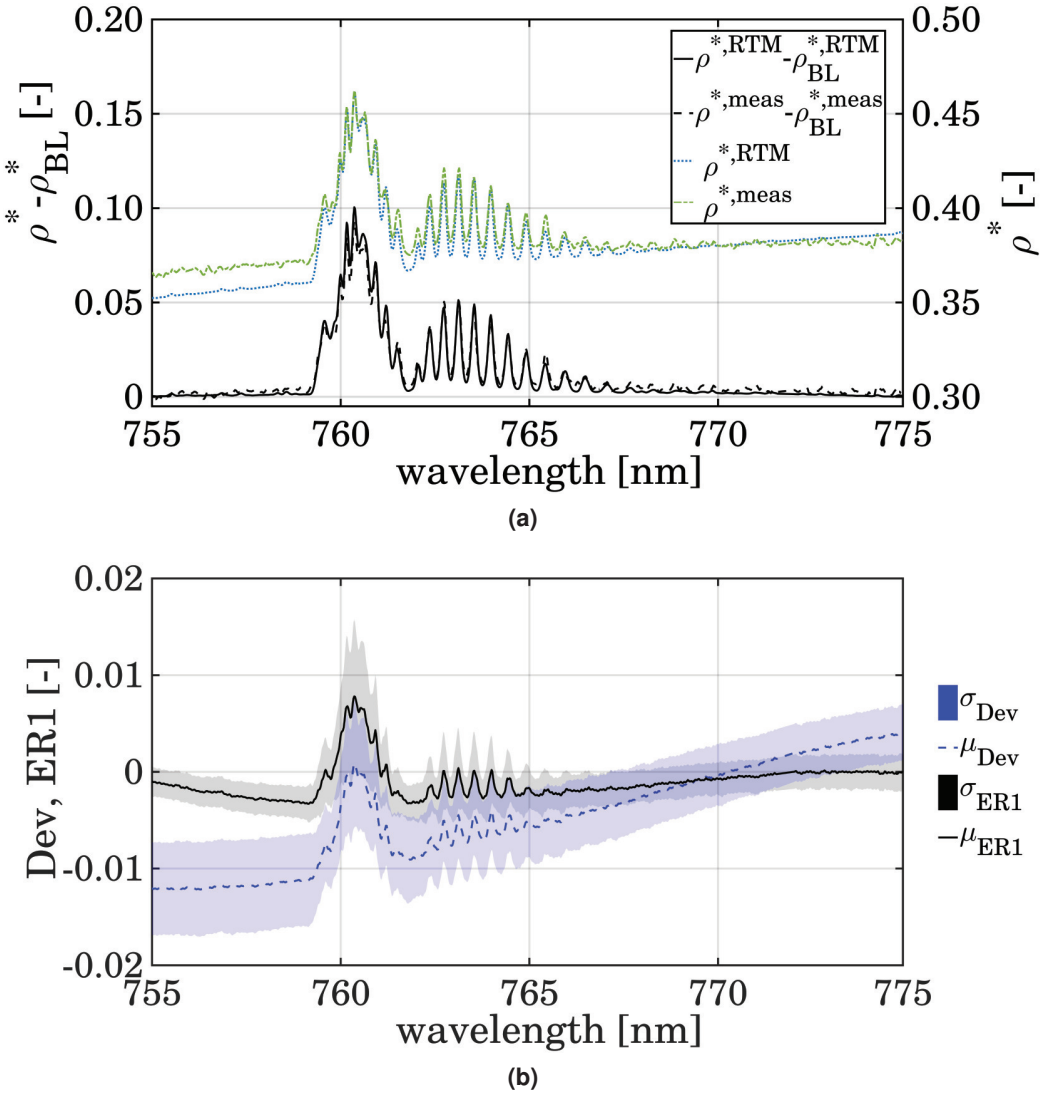

Figure 28: a) Example of the minuend ($\rho^{*,meas} - \rho^{*,meas}_{BL}$) and the subtrahend ($\rho^{*,RTM} - \rho^{*,RTM}_{BL}$) of the term ER1 in the cost function (Eq. 25), as well as the modeled ($\rho^{*,RTM}$) and measured ($\rho^{*,meas}$) apparent reflectance in the spectral region around the O_2-A band. b) Mean (μ) and standard deviation (σ) of the difference between $\rho^{*,RTM}$ and $\rho^{*,meas}$ (Dev) and of the ER1 term of the cost function, in the spectral region around the O_2-A band. Data in (b) refer to the whole dataset.

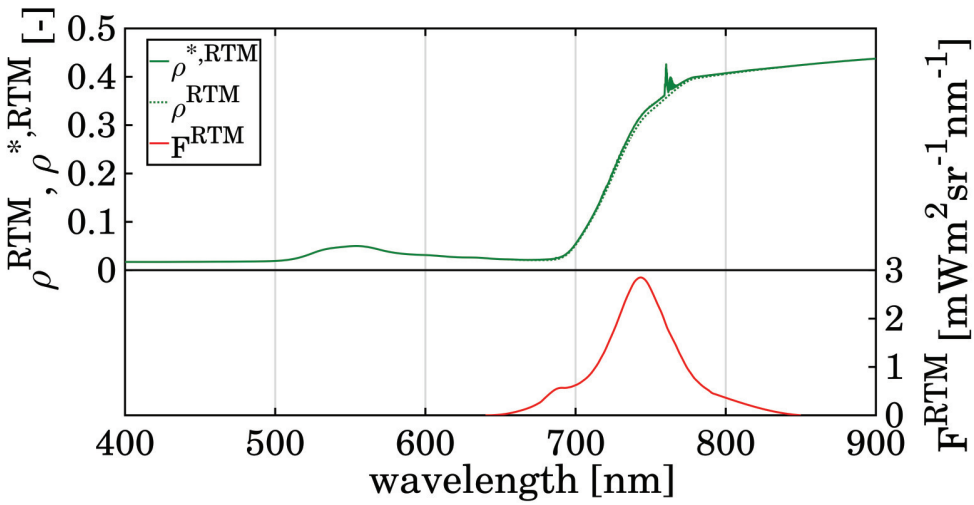

Figure 29: Example of the true (ρ^{RTM}) and apparent ($\rho^{*,RTM}$) reflectance and fluorescence (F^{RTM}) spectra simulated with the RTMc model.

4.2.4 Regression models and error estimation

All data in the plots are reported as mean ± standard deviation, unless differently indicated. Similarly, the linear regression models shown in this paper are obtained with Ordinary Least Squares (OLS) fitting. For the robust regression models, the `bisquare` weighting scheme for downweighting outliers included in MATLAB® R2016b `fitlm` function was used.

The Root Mean Squared Error (RMSE) and the Relative Root Mean Squared Error (RRMSE) were computed according to Eq. 26 and Eq. 27, respectively. Together with the slope (m), the intercept (q) and the coefficient of determination (R^2), they were used to compare the retrieved ($\hat{y}$) and the reference (y) values.

$$\mathrm{RMSE} = \sqrt{\frac{\sum_{i=1}^{n}(\hat{y}_i - y_i)^2}{n}} \tag{26}$$

$$\mathrm{RRMSE} = \sqrt{\frac{\sum_{i=1}^{n}\left(\frac{\hat{y}_i - y_i}{y_i}\right)^2}{n}} * 100 \tag{27}$$

where n is the number of observations.

4.3 RESULTS AND DISCUSSION

4.3.1 Evaluation of the modeled reflectance and fluorescence

Table 8 shows the results of the inversion of the RTMc model on the simulated spectral dataset. The comparison between fluorescence values at 687 nm (F_{687}^{RTM}) and at 760 nm (F_{760}^{RTM}) retrieved inverting RTMc and the reference values are reported as well. In general, the agreement between true and retrieved biochemical and biophysical vegetation parameters is quite good: the R^2 values are generally larger than 0.9 for most of the parameters, and the RMSEs are reasonably low. The slope of the OLS linear model for F_{687}^{RTM} and F_{760}^{RTM} are close to one, while there is a certain overestimation in retrieved F_{760}^{RTM} ($q = 0.59\,mW\,m^{-2}\,sr^{-1}\,nm^{-1}$). F^{RTM} values integrated over the whole emission spectrum (F_{int}^{RTM}) show similar R^2 value, with RMSE = $41.26\,mW\,m^{-2}\,sr^{-1}$ and $q = 55.08\,mW\,m^{-2}\,sr^{-1}$. The RRMSE is generally lower or very close to 10%. When applying robust bisquare linear regression, the variance explained by the model is often close to 100%, and the RMSE is very low. Nevertheless, fqe is still overestimated ($m = 1.33$), and a positive bias in F_{760}^{RTM} and F_{int}^{RTM} values is still present ($q = 0.39\,mW\,m^{-2}\,sr^{-1}\,nm^{-1}$ and $q = 37.92\,mW\,m^{-2}\,sr^{-1}$, respectively). The general slight overestimation of the F values retrieved with RTMc is linked to the overestimation of the retrieved fqe parameter since at photosystem level there is a multiplicative factor between the two. This, in turn, can be partially due to the extremely wide range of simulated fqe values, an unrealistic case far from real world applications where the F emission is much more constrained by fqe. Nevertheless, in order to test the most general and worst possible scenario (in terms of retrieval uncertainty), the full range of variation of fqe (0–1) was used for both the simulation and the retrieval.

In order to evaluate the performances of the SFM and the SpecFit retrieval algorithms, F_{687}^{SFM} and F_{760}^{SFM} were retrieved starting from the simulated spectra, and the integral of the emitted fluorescence spectrum in the 670–780 nm spectral range was computed. If no additional noise is added to the simulated data, the agreement between the modeled (*i.e.*, the reference values in this case) and the retrieved F^{SFM} values is almost perfect (F_{687}^{SFM}: R^2= 1.00, RMSE = $0.08\,mW\,m^{-2}\,sr^{-1}\,nm^{-1}$; F_{760}^{SFM}: R^2= 1.00, RMSE = $0.03\,mW\,m^{-2}\,sr^{-1}\,nm^{-1}$; $F_{int}^{SpecFit}$: R^2= 1.00, RMSE = $0.03\,mW\,m^{-2}\,sr^{-1}$), even though F_{687}^{SFM} values are slightly overestimated ($m = 1.05\,mW\,m^{-2}\,sr^{-1}\,nm^{-1}$). In all cases the RRMSE is lower than 10%, with a very low value of 0.67% for F_{760}^{SFM}, and these values further improve if robust bisquare linear regression models are used. These results confirm what was observed in Cogliati et al. (2015), and indicate that SFM and SpecFit are very good performing fluorescence retrieval algorithms when a proper estimation of the incoming solar

Table 8: Coefficient of determination (R^2), Root Mean Square Error (RMSE), Relative Root Mean Square Error (RRMSE), slope (m) and intercept (q) of the OLS linear regression model between reference and retrieved values of RTMc parameters, fluorescence at 687 nm (F_{687}^{RTM}) and at 760 nm (F_{760}^{RTM}), as well as the integral of the full spectrum of F (F_{int}^{RTM}) are reported. Regression coefficients between reference values and F retrieved with SFM (F_{687}^{SFM} and F_{760}^{SFM}) and with SpecFit ($F_{int}^{SpecFit}$) starting from the simulated spectra are reported too. All values in brackets refer to the robust bisquare linear regression model. p-value is always < 0.001.

Parameter	Unit	R^2	RMSE	RRMSE [%]	m	q
C_{ab}	$\mu g\,cm^{-2}$	0.94 (0.99)	3.87 (1.19)	9.83 (3.02)	0.88 (0.91)	0.38 (0.00)
C_{car}	$\mu g\,cm^{-2}$	0.87 (0.98)	1.27 (0.57)	12.74 (5.70)	1.01 (1.04)	0.27 (0.01)
LAI	$m^2\,m^{-2}$	0.97 (0.97)	0.29 (0.26)	8.64 (7.75)	1.10 (1.13)	0.01 (-0.07)
fqe	-	0.95 (0.99)	0.004 (0.003)	10.38 (7.79)	1.34 (1.33)	0.004 (0.003)
F_{687}^{RTM}	$mW\,m^{-2}\,sr^{-1}\,nm^{-1}$	0.96 (0.99)	0.17 (0.12)	10.42 (7.36)	1.03 (1.02)	0.18 (0.13)
F_{760}^{RTM}	$mW\,m^{-2}\,sr^{-1}\,nm^{-1}$	0.95 (0.99)	0.95 (0.27)	8.67 (4.88)	0.99 (1.00)	0.59 (0.39)
F_{int}^{RTM}	$mW\,m^{-2}\,sr^{-1}$	0.96 (1.00)	41.26 (27.39)	8.31 (5.51)	1.00 (1.00)	55.08 (37.92)
F_{687}^{SFM}	$mW\,m^{-2}\,sr^{-1}\,nm^{-1}$	1.00 (1.00)	0.08 (0.03)	5.62 (2.11)	1.05 (1.02)	-0.01 (0.01)
F_{760}^{SFM}	$mW\,m^{-2}\,sr^{-1}\,nm^{-1}$	1.00 (1.00)	0.03 (0.03)	0.67 (0.67)	0.99 (0.99)	0.00 (-0.01)
$F_{int}^{SpecFit}$	$mW\,m^{-2}\,sr^{-1}$	0.99 (1.00)	36.70 (25.70)	8.49 (5.95)	1.01 (1.02)	0.90 (0.40)

irradiance is provided (a perfect atmospheric correction is in fact assumed in this case).

In this paragraph the results of the measured spectral dataset are reported. Figure 30 shows an example of the measured ($\rho^{*,meas}$) and retrieved ($\rho^{*,RTM}$) apparent reflectance (left panel). The regions around the O_2-B and O_2-A oxygen absorption bands are highlighted. F_{687}^{SFM} and F_{760}^{SFM} values retrieved with SFM, the full F spectrum retrieved with SpecFit, as well as the F spectrum retrieved with RTMc (F^{RTM}) are reported. The deviation (difference) and the RRMSE between measured and retrieved apparent reflectance, computed for the whole dataset across the whole spectral range used for the model inversion, are shown in Figure 31. In general the fitting is good, but the model systematically overestimates ρ^* in the blue region and it is not perfectly able to reproduce the slope of the red-edge and the NIR plateau. In particular, ρ^* is overestimated before 450 nm, from 700–745 nm, and from 770–835 nm, and it is underestimated afterwards. In the green region, from 500–550 nm, the model reproduced almost correctly the shape of the measured apparent reflectance, while small second order differences are still present. The overestimation of ρ^* in the blue could be triggered by a small underestimation of L_{sky}^{meas} (imperfect characterization of the atmospheric scattering). The remaining discrepancies in ρ^* can be partially attributed to the pigment absorption coefficients (cfr. van der Tol et al., 2016), especially in the green and red spectral regions. The discrepancy in the red-edge region, and in particular from 700–770 nm is likely due to the effect of an inaccurate retrieval of the senescent material in the leaves (C_s), a parameter that preferentially affects the slope of the reflectance in this spectral region. Figure 32 shows the variation induced in the reflectance spectra when selectively varying C_s from 0 to 0.25. Uncertainties in the characterization of the direct and the diffuse components of the incoming radiation should have a very limited effect on the shape of the modeled reflectance outside the atmospheric absorption bands. The measurements, in fact, were always performed in cloud-free conditions, with Sun Zenith Angles (SZAs) lower than 60°, and the real SZA was used to simulate the reflectance components in the model inversion routine. The fraction of direct/diffuse irradiance can nevertheless partly explain the residual difference in the modeling of apparent reflectance in the O_2-A band (750–770 nm). The depth of the absorption band depends on the path-length followed by photons from the Sun via the target to the sensor (Cogliati et al., 2015), being therefore influenced by the direct/diffuse ratio. This is true for the O_2-B band as well, but its depth and width are lower compared to the O_2-A band, therefore this effect is less pronounced. The OLS linear regression model between F_{687}^{SFM} and F_{687}^{RTM} computed for the whole dataset of field measurements shows a good correlation between the two fluorescence retrievals ($R^2 = 0.84$) with a RMSE of 0.15 $mW\,m^{-2}\,sr^{-1}\,nm^{-1}$ (Figure 33a). Two point clouds are clearly dis-

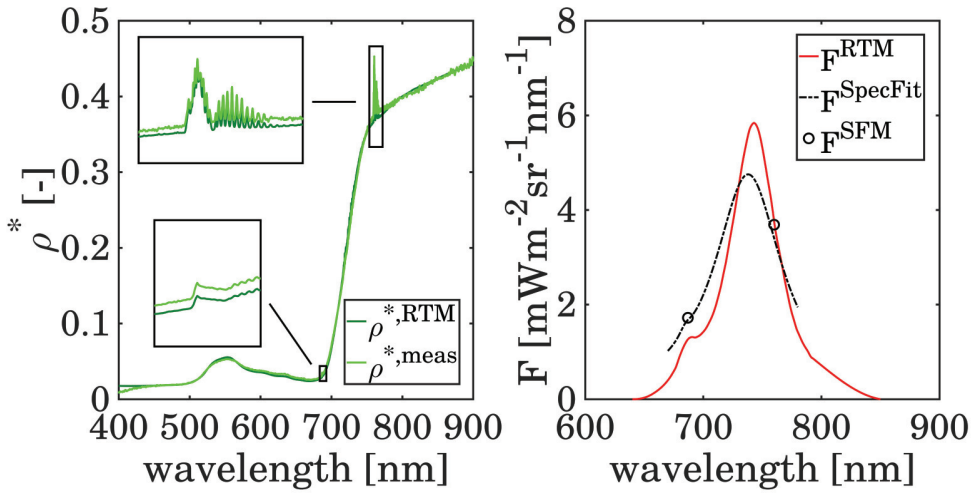

Figure 30: Example of the measured and retrieved apparent reflectance (left) and fluorescence values (right). The regions around the O_2-B and O_2-A oxygen absorption bands are highlighted.

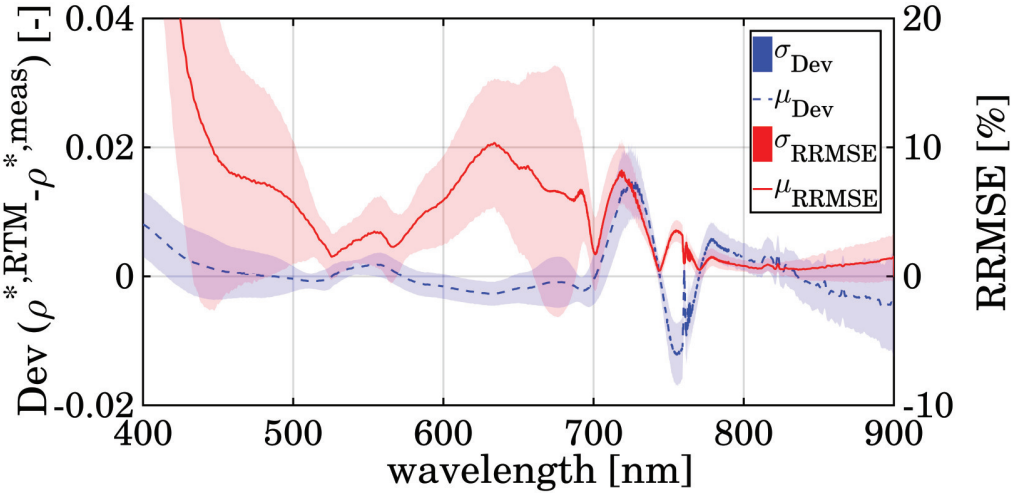

Figure 31: Mean (μ) and standard deviation (σ) of the difference (Dev) and the Relative Root Mean Square Error (RRMSE) between measured and retrieved apparent reflectance (ρ*), computed for the whole dataset across the whole spectral range used for the model inversion.

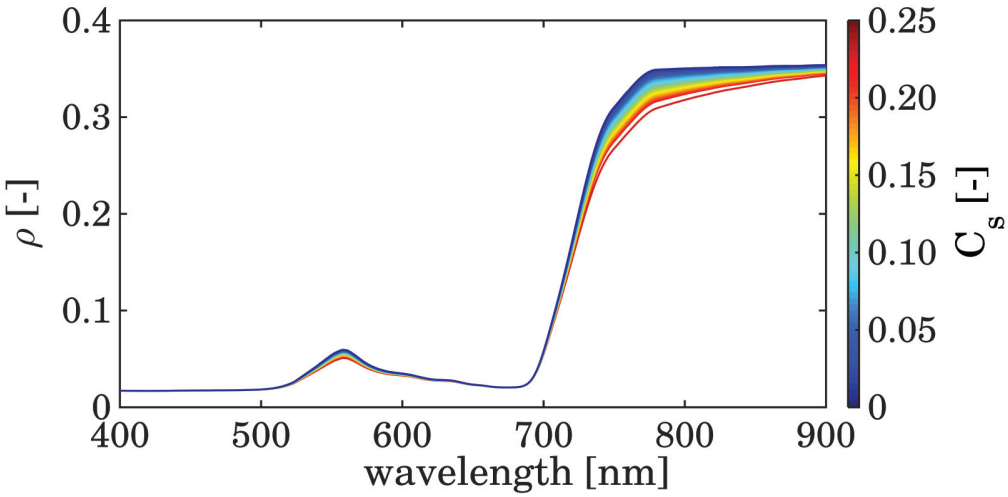

Figure 32: Reflectance simulated with SCOPE 1.70 varying the content of senescent material in the leaves (C_s) from 0 to 0.25.

tinguishable, one composed by F_{687} values between 0.5 $mW\,m^{-2}\,sr^{-1}\,nm^{-1}$ and 1 $mW\,m^{-2}\,sr^{-1}\,nm^{-1}$, and the other composed by higher values. F_{760} (Figure 33b) shows an even higher R^2 (0.97) and a slope much closer to 1 ($m = 1.03$), while the average RMSE is 0.22 $mW\,m^{-2}\,sr^{-1}\,nm^{-1}$. F_{int}^{RTM} values (Figure 33c) closely resemble $F_{int}^{SpecFit}$ ones ($m = 1.02$; $q = 39.17\,mW\,m^{-2}\,sr^{-1}$; $R^2 = 0.96$; RMSE = 22.91 $mW\,m^{-2}\,sr^{-1}$). When applying a robust bisquare linear regression model to the data (green dashed line), the fittings improve. In particular, the RMSE of F_{687} and F_{760} decreases to 0.14 $mW\,m^{-2}\,sr^{-1}\,nm^{-1}$ and 0.19 $mW\,m^{-2}\,sr^{-1}\,nm^{-1}$, respectively, while the R^2 slightly increases to 0.85 and 0.98. Nevertheless, the slope of the linear model for F_{687} is still far from one (m = 0.81) and the intercept (q) is 0.22 $mW\,m^{-2}\,sr^{-1}\,nm^{-1}$, while F_{760} from RTMc inversion is overestimated of about 0.51 $mW\,m^{-2}\,sr^{-1}\,nm^{-1}$. It is worth noting that the two fluorescence retrievals are completely independent and use different parametrization of the functions describing both fluorescence and reflectance. In this perspective, and lacking an independent reference for F values, RMSE and RRMSE are to be interpreted as "deviations" more than "errors". Moreover, due to the herbicide application, the range of variation of F_{760} and F_{687} found in this study is extreme when compared to what has been observed with the same measurement setup over a wide range of crops and natural vegetation (Rossini et al., 2016). This indicates that both SFM/SpecFit and the SCOPE-based RTMc model are flexible enough to cope with different (up to extreme) variations in emitted F triggered by stress events.

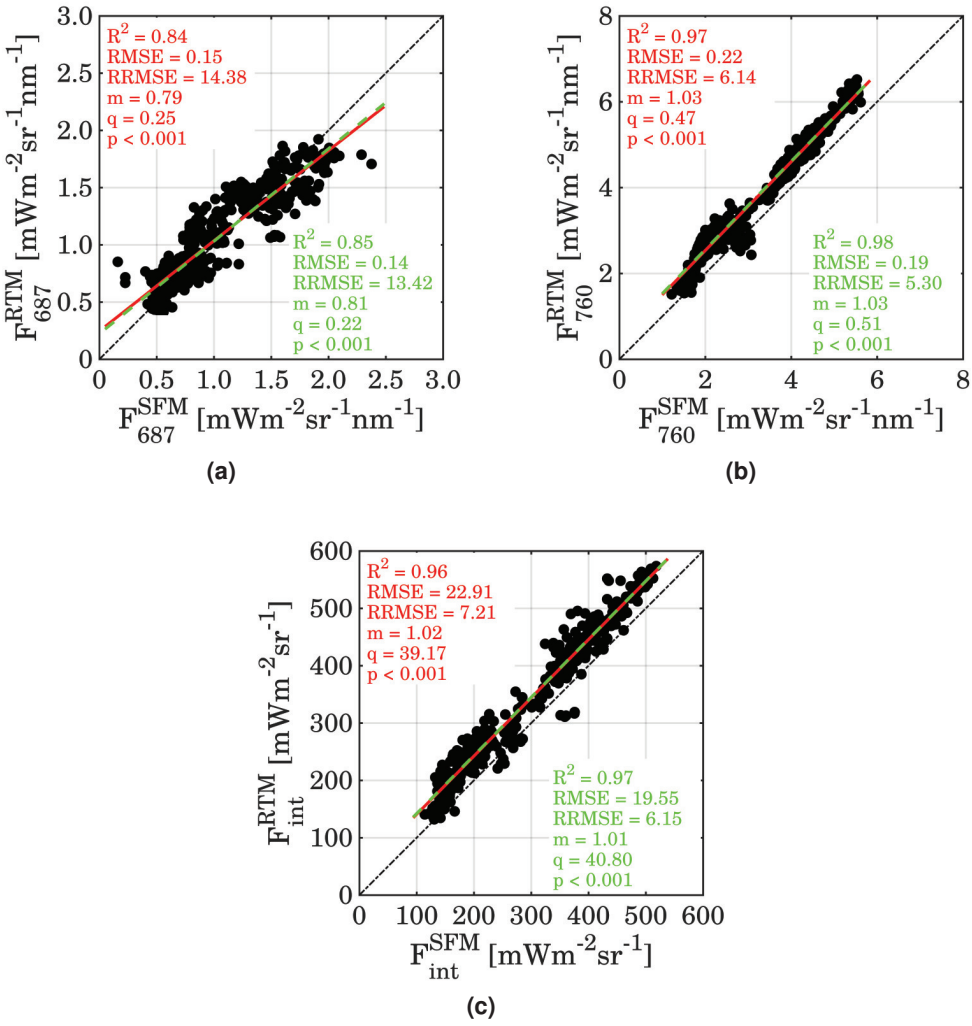

Figure 33: OLS (red solid line) and robust bisquare linear regression model (green dashed line) between F values retrieved with SFM and obtained with RTMc inversion. a) linear regression models for F_{687}; b) linear regression models for F_{760}; c) linear regression models for F_{int}.

4.3.2 Monitoring the retrieved parameters during the induced stress experiment

In this section the temporal evolution of a selection of parameters retrieved for the stress-detection field experiment, and the retrieved F radiances, are shown and discussed. In the following plots only data collected around solar noon, *i.e.*, ± one hour, are used to compute mean and standard deviation for each DAT. Data refer to a control ("Control") and two treated plots, one with the lowest ("Low Dose") and the other with the highest dose in the experimental setup ("High Dose").

Modeled fluorescence values at the O_2-B (Figure 34a) and O_2-A band (Figure 34c) follow the dynamics observed in fluorescence retrieved with SFM quite well (Figs. 34b and 34d). Just after the treatment, there is an abrupt increase of both F_{760} and F_{687} and a subsequent decrease in the following days. The control plot shows no significant variation in F values over time. Absolute F values are correctly reproduced as well, coherently with what already discussed in section 4.3.1. Although there is a systematic overestimation of F_{int}^{RTM} values of about $40\,mW\,m^{-2}\,sr^{-1}$ compared to $F_{int}^{SpecFit}$, the relative agreement between the observed values is still high, and the temporal dynamics are preserved. This bias in F_{int}^{RTM} can be attributed to the different shape of the fluorescence emission spectrum modeled by the two algorithms. In particular, RTMc based F spectra tend to systematically overestimate F in the far-red region (cfr. Figure 33b), and this triggers the overestimation in F_{int} as well.

Figure 35 shows the temporal variation of a selection of leaf and canopy retrieved parameters. A few hours after the treament was applied, the relative variation of leaf chlorophyll content (C_{ab}; Figure 35a) compared to the pre-treatment values was negligible. Starting from DAT 1, C_{ab} values of the treated plots started to decrease slowly. *LAI* values (Figure 35b) in contrast were stable over time (as foreseen considering that the treatment did not induce any structural variation). During the campaign the grassland was not cut, thus a certain increase in plant biomass in the control plot could be easily justified. The content of senescent material (C_s; Figure 35c) stays stable over time in both the control and the "Low Dose" plot, even though the average values differed almost by a factor of 2. In the "High Dose" plot, C_s increased over time following pigment degradation and plant browning. Retrieved Φ_F values (Figure 35d) clearly show a quick and strong response of the photosynthetic apparatus to the applied treatment, even on DAT 0, few hours after the application. Φ_F values are in agreement with both F^{RTM} and F^{SFM} (in particular with F_{760} values). This is largely driven by the fact that in this experiment the strongest driver of F variation is the inhibition of PQ and NPQ by the chemical application, so that in this specific case the informative content of F and Φ_F is similar (in particular when looking only at midday measure-

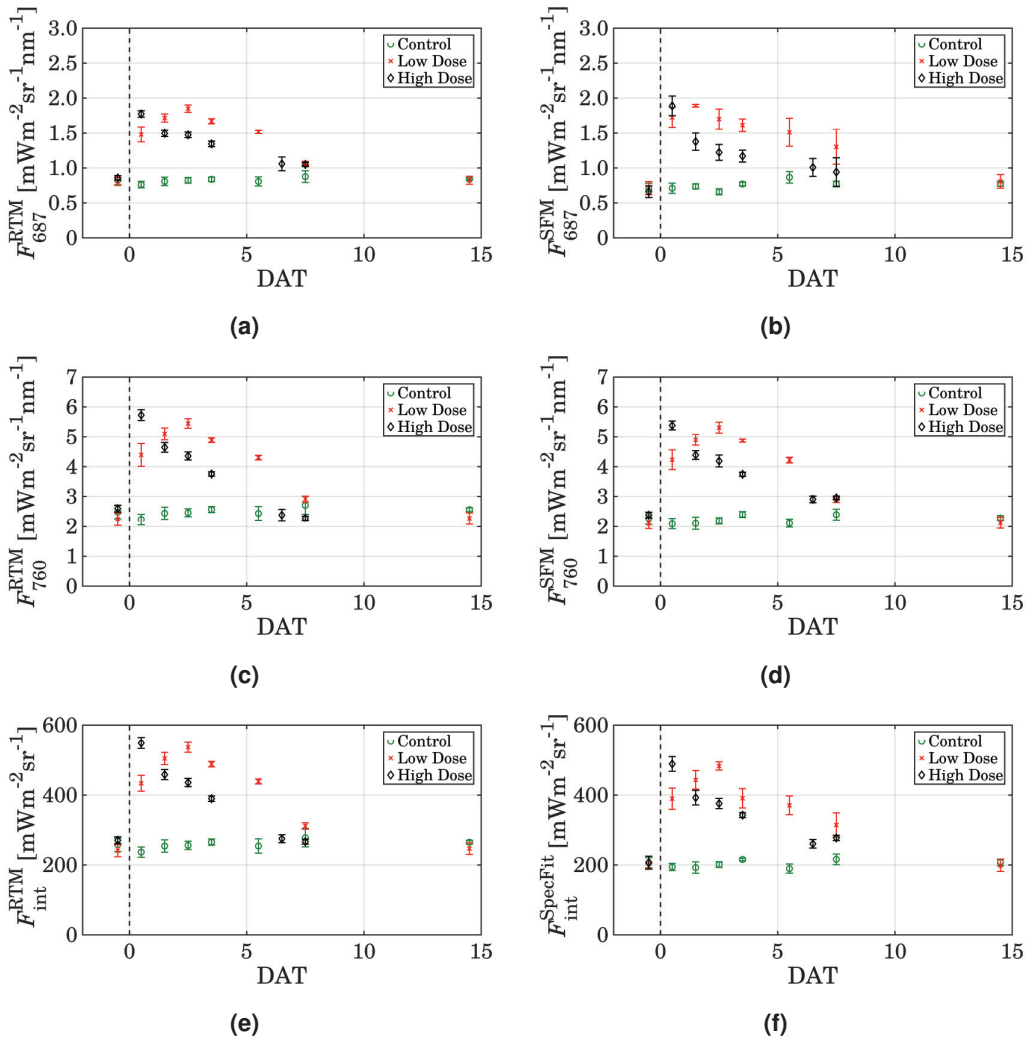

Figure 34: Time series of fluorescence values retrieved with RTMc inversion ("a", "c" and "e") and with the SFM algorithm ("b", "d" and "f"). The x axis shows the number of Days After the Treatment (DAT).

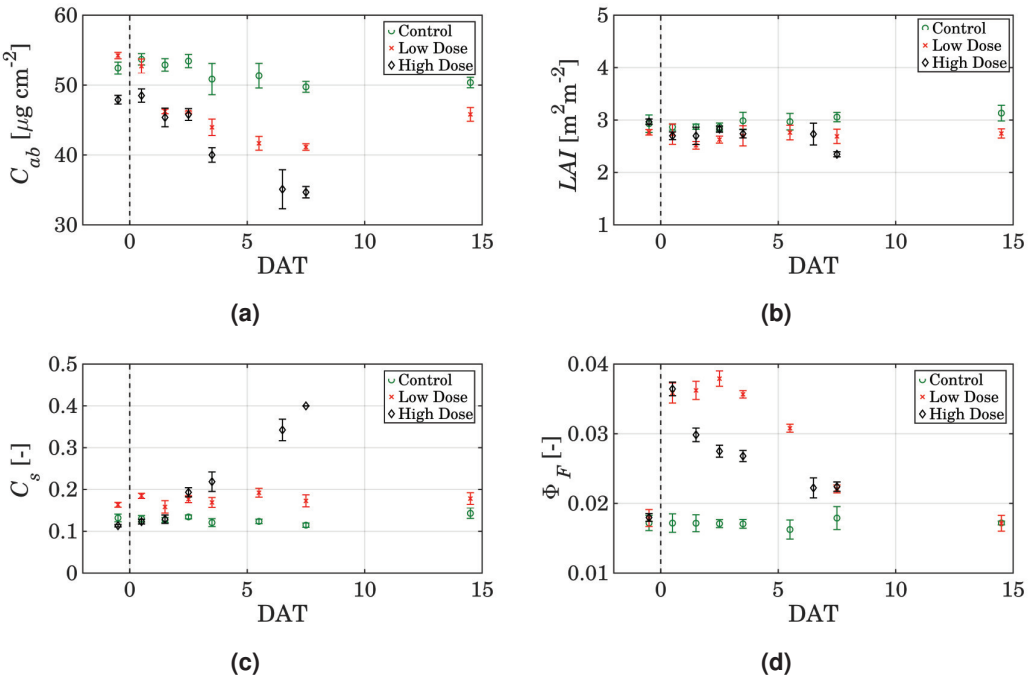

Figure 35: Time series of parameters retrieved from RTMc inversion. The x axis shows the Day After Treatment (DAT).

ments). Nevertheless these results are consistent with what was observed in a recent study by Hernández-Clemente et al. (2017) using a dataset simulated with the 3-D FluorFLIGHT model (in particular cfr. Figure 11d).

4.3.3 Combined observation of Φ_F and C_{ab} for stress detection

Figure 36 shows the combined variation of C_{ab} and Φ_F during the experiment for the three plots. The combined analysis of the variation of these two parameters helps to identify the different phases of the stress induced to the plants, and the resulting effects. In the control plot (Fig. 36a), Φ_F did not vary during the campaign, while there was a small fluctuation of C_{ab} values. This can be due to a compensation effect with other model parameters (*e.g.*, LAI) during the model inversion process, that showed a similar but opposite variation towards the end of the campaign (cfr. Figure 35b). Figure 36b shows a circular pattern of Φ_F versus C_{ab}, after application of a low dose of Dicuran ("Low Dose"). Immediately after the treatment, the abrupt rise of Φ_F with no variation of C_{ab} indicates that the plants were experiencing a strong physiological stress, without detectable physical damage to the photosynthetic apparatus. In the following three days, Φ_F values stayed high, while C_{ab} started decreasing due to the prolonged stress condition. From DAT 3 to 5, Φ_F and C_{ab} values decreased together, while from DAT 5 to 7 only Φ_F showed a further decrease, probably because the effect of Dicuran diminished and the grass recovered 14 days after the chemical was applied. Values of both Φ_F and C_{ab} were close to the pre-treatment ones. When the treatment was applied with a much higher dose ("High Dose"; Figure 36c), after a quick increase of Φ_F with almost no variation in C_{ab} values, both parameters started decreasing rapidly. Several days after the treatment, the plants were brownish, so that the measurements were stopped. At that point, almost 50% of the original C_{ab} content was lost, and the plants did not show any sign of recovery for the rest of the campaign. In this case the decrease in Φ_F can be attributed to a progressive deterioration of the photosynthetic machinery and not to a recovery after the stress event, but this becomes clear only when looking at the concurrent variation of pigment content (*i.e.*, C_{ab}) and efficiency (*i.e.*, Φ_F) parameters. Putting this into the perspective of a repeated (or continuous) observation through RS platforms, it will be possible to characterize stress-specific patterns and to effectively distinguish between acute stress events and prolonged stress phases, monitoring their implications on the long-term functioning of the vegetation.

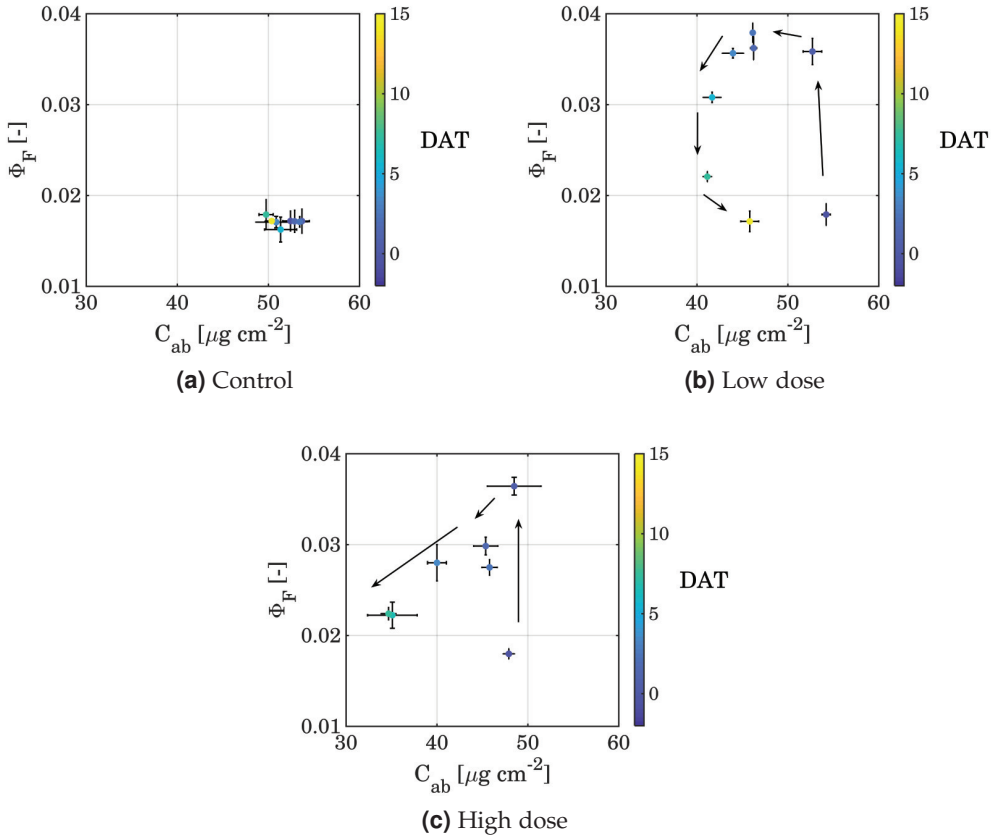

Figure 36: scatter plots between chlorophyll a+b content (C_{ab}) and fluorescence quantum yield (Φ_F), for three different plots: a control (panel "a"), a plot treated with a low dose ("b") and one with a high dose of herbicide ("c"). The color palette refers to the number of Days After the Treatment (DAT), the arrows follow the temporal dynamic as well.

4.3.4 Using Φ_F to invert a biochemical model for photosynthesis and fluorescence

We have already discussed that Φ_F is linked to the activity of the photosynthetic machinery, so that a variation in the photochemical (Φ_P) or non photochemical yield (Φ_N) reflects in a variation of Φ_F. Φ_F can be expressed as a ratio of rate coefficients (K) (Eq. 20), with $K_F = 0.05$ and $K_D = 0.95$. Φ_F is maximum when both K_P and K_N are 0 (*i.e.*, both PQ and NPQ are blocked), so that $\Phi_F^{max} = 0.05/1 = 0.05$, and minimum when K_P is high (*e.g.*, $K_P = 4$ and $K_N = 0$; van der Tol et al. 2014), so that $\Phi_F^{min} = 0.05/4 = 0.0125$, or when K_N is very high (*e.g.*, $K_N = 10$ and $K_P = 1$; Porcar-Castell 2011), so that $\Phi_F^{min} = 0.05/11 \approx 0.005$. With unstressed (control) values around 0.015 and maximum stressed (treated) values around 0.035–0.040, the Φ_F values retrieved from the apparent reflectance through RTMc inversion are close to the maximum, which is as expected considering that the Dicuran is known to strongly inhibit both PQ and NPQ. As a test, if we substitute $K_P = 0.15$ and $K_N = 0.15$ in equation 20, the resulting Φ_F value of 0.039 indicates that even a small amount of residual (*i.e.*, non inhibited) PQ and NPQ would be enough to justify the retrieved maximum values of Φ_F.

4.4 CONCLUSIONS

For the first time we concurrently retrieved the full spectrum of solar-induced chlorophyll a fluorescence (F), fluorescence quantum yield (Φ_F) and biochemical properties of grass inverting the optical radiative transfer routines of the SCOPE model. The promising results obtained in this study open interesting perspectives for exploiting the increasing number of high resolution data from multi-scale Remote Sensing (RS) platforms. Computational times could be shortened by means of emulators of the radiative transfer models (Rivera et al., 2015). Moreover, a multi-step inversion routine where computationally efficient retrieval algorithms would be used to retrieve key parameters like chlorophyll content (C_{ab}) and Leaf Area Index (LAI), then used as priors for a better regularization of the numerical optimization inversion scheme is already in development. In addition, in an operational perspective independently retrieved F values (*e.g.*, with SFM or SpecFit), could be used as a constrain inside the cost function as well, while in this study we used them as a benchmark for the modeled values. The future ESA FLEX mission is an ideal candidate for applying these combined retrieval approach, since it will provide hyperspectral data in the Visible and Near InfraRed (VNIR) spectral region, as well as very high resolution data around the oxygen absorption bands (*i.e.*, a spectral configuration similar to the one used in this study). The

HyPlant sensor (Rascher et al., 2015), developed by the Forschungszentrum Jülich (Germany) in collaboration with Specim Spectral Imaging Ltd (Finland), is the airborne demonstrator for the FLEX mission. Further developments are ongoing to apply a similar scheme to HyPlant imageries for producing maps of vegetation parameters, F and Φ_F, and developing and refining algorithms that will be applied to future satellite data.

Using Φ_F (or F) to derive information about plant photosynthesis is still challenging. In this study we sketched the feasibility of using Φ_F as a quantitative indicator of Photochemical Quenching (PQ). More efforts are needed in this regard, especially in enlarging the domain of the biochemical models to account for a wider range of physiological conditions, and in finding a proper regularization strategy for Non-Photochemical Quenching (NPQ). Nevertheless, first results indicate that it is possible to use Φ_F retrieved from hyperspectral RS observations to obtain information on PQ. This opens new perspective for using RS observation of F and Φ_F in dynamic vegetation models for a better quantification of photosynthesis from space.

5 SUMMARY AND CONCLUSIONS

The main aim of this research was to exploit multi-source remotely sensed data to improve vegetation status analysis. In particular, I focused on canopy level chlorophyll a fluorescence (F) and reflectance (ρ) retrieved from very high resolution data acquired with ground and airborne spectroradiometers. This thesis has been divided in five chapters. Chapter 1 gives an introduction about the framework within which this thesis was developed. Chapters 2, 3 and 4 address different approaches that pursue the combined use of F and reflectance for studying vegetation dynamics. Each of these chapters focuses on one of the specific objectives declared in Section 1.1. The main results of each of these chapters are summarized and discussed below, together with some concluding remarks and perspectives.

5.1 MAIN RESULTS

Red F metrics estimated from the high-performance HyPlant airborne sensor track changes in plant physiology associated with age-related hydraulic limitation

The results of this study (Chapter 2) aimed at the investigation of the relationship between stand age-related processes and remotely sensed F in a managed loblolly pine (*Pinus taeda* L.) forest in North Carolina (USA), show that: i) red fluorescence (F_{lob}^{690}) and red fluorescence yield (Fy_{lob}^{690}) change with stand age; younger loblolly pines dissipate more F_{lob}^{690} than older one, and the decline of Fy_{lob}^{690} with stand age is more pronounced than that for F_{lob}^{690}, or for the apparent red-fluorescence yield; ii) only F_{lob}^{690} and Fy_{lob}^{690} declined with tree age, while F_{lob}^{740} and Fy_{lob}^{740} did not. Leaf stomatal conductance measurements clearly show

significant reduction with stand age and potentially explain the drop of red fluorescence with age. Results observed in a similar loblolly pine forest site showed that leaf-level photosynthetic parameters declined with tree age due to an increasing water limitation of the plants, supporting the hydraulic limitation hypothesis. The stomatal limitation model shows an opposite trend compared to the observed decline in Fy_{lob}^{690}. In this framework, the decline of Fy_{lob}^{690} can be interpreted as a primary consequence of the increasing photosynthetic stomatal limitations in aging loblolly trees. Fy_{lob}^{690} is thus influenced by the reduced carbon and water availability induced by the water limitation processes, which occurs in older and larger trees.

Results from analysis with spatially aggregated data at stand-scale revealed that the relationships between red F radiances and yields with tree age were substantially weakened by spatial averaging. To mitigate the effect of heterogeneous canopy cover on F, the Canopy Cover Fluorescence Index was proposed to partially correct for the proportion of loblolly pine inside each aggregated pixel.

Ground and airborne measurements of red and far-red F, together with complementary remote sensing parameters, detect short-term dynamics of photosynthetic efficiency in vegetation

This study (Chapter 3), aimed at detecting short-term induced alterations of photosynthesis functioning in grass using ground and airborne measurements, shows that apparent fluorescence yield (Fy^*) quickly responded to the application of Dicuran. Changes in other RS parameters revealed that alterations produced by the herbicide involved various physiological and biophysical processes. The use of Dicuran as stressor permitted to have a quick and well-characterized effect in the photosynthetic apparatus. Despite of the differences that might exist between the action of Dicuran and natural stressors, the photochemistry was effectively blocked by the Dicuran as demonstrated by the rapid reduction of carbon dioxide (CO_2) assimilation rates and LUE. Moreover, the increase of canopy temperature suggests that treated plants closed their *stomata* the days following the application. Hence, the fast increase and later fluctuations of Fy^* observed after the application of Dicuran can be attributed to the sudden inhibition of the electron transport chain and the subsequent redistribution of energy in the available dissipation pathways. The differences in GPP, LUE, ΔT and Fy^* observed between the treatments immediately after the application of Dicuran denoted a higher degree of photosynthesis inhibition with increasing concentrations of the herbicide. The drop observed in chlorophyll content after the treatment - and in the related index Meris Terrestrial Chlorophyll Index (MTCI) - may respond to photodamage and

photoprotective mechanisms to reduce the absorbed radiation. This can contribute to the gradual drop of Fy^* observed toward the end of the experiment. The differences between the kinetics of Fy^*_{687} and Fy^*_{760} can provide valuable information to elucidate at which level the stress is affecting photosynthesis. In this experiment we observed that in the lower doses treatments the initial rise of Fy^*_{687} was quenched faster than Fy^*_{760}. This quick decrease of Fy^*_{687} coincides with the drop of Photochemical Reflectance Index (PRI) and thus can be attributed to the combined action of NPQ and the degradation of chlorophyll. In the case of Fy^*_{760}, the peak was observed after the PRI started to decrease. One reason for this can be that the Dicuran action affects directly the short-term regulatory mechanisms of light harvesting in the PSII, where the F_{687} originates. Hence, any evolution of the stress would modulate this signal almost instantaneously. On the other hand, F_{760} is emitted by both photosystems, therefore, the fraction of F_{760} emitted from the less regulated PSI would respond more slowly to adaptation mechanisms.

The numerical inversion of a physically based RTM on very high resolution field spectroscopy measurements successfully retrieves the full spectrum of F, Φ_F, and several biochemical and structural vegetation parameters

This study (Chapter 4) was aimed at inverting numerically a simplified version of the SCOPE model to retrieve concurrently the full spectrum of canopy F, the fluorescence quantum yield (Φ_F), as well as the main vegetation parameters that control light absorption and reabsorption from very high resolution field spectroscopy measurements. The results show that the model inversion was able to reproduce accurately the F values retrieved from the top-of-canopy radiance measurements with state-of-the-art spectral fitting methods, even if the two fluorescence retrievals are completely independent and use different parametrization of the functions describing both fluorescence and reflectance. Moreover, due to the herbicide application, the range of variation of F_{760} and F_{687} found in this study is extreme when compared to what has been observed with the same measurement setup over a wide range of crops and natural vegetation. This indicates that both spectral fitting methods and the SCOPE-based retrieval model are flexible enough to cope with different (up to extreme) variations in emitted F triggered by stress events. The model was also able to correctly reproduce the top-of-canopy reflectance spectra in the VNIR. Retrieved Φ_F values clearly show a quick and strong response of the photosynthetic apparatus to the applied treatment, even on the first Days After Treatment (DAT), few hours after the application. The dynamics of Φ_F values are in agreement with those of the F values (in particular

F_{760} values). This is largely driven by the fact that in this experiment the strongest driver of F variation is the inhibition of PQ and NPQ by the chemical application, so that in this specific case the informative content of F and Φ_F is similar (in particular when looking only at midday measurements). Finally, as a test, I compared the retrieved Φ_F values with an independent biophysical model of photosynthesis and fluorescence, finding good agreement in absolute maximum and minimum values.

5.2 CONCLUDING REMARKS

Fluorescence in the red region (*i.e.*, F_{690} in Chapter 2 and F_{687} in Chapter 2, respectively), and the derived yields (*i.e.*, Fy^{690} in Chapter 2 and Fy^{*}_{687} in Chapter 2, respectively) proved to be more sensible to variations in the functional state of the photosynthetic machinery than their counterparts in the far-red region. This was particularly true in regards to changes in hydraulic conductance in aging loblolly pines, but it was also observed as a faster quenching of the initial rise of Fy^{*}_{687} in the manipulated stress experiment. Nevertheless, both F_{687} and F_{760} demonstrated to be highly sensible to quick changes in photosynthesis function in the second case-study. However, additional biophysical and physiological parameters were necessary to interpret the temporal changes in fluorescence and finally unravel the mechanism of action of the stressor. By combining the information provided by the solar-induced fluorescence, the canopy temperature, and the vegetation indices it was possible to derive a conceptual model that explained the most relevant events that occurred in the photosynthetic apparatus after the application of the herbicide. These findings could be derived independently from both ground-based and aerial (even if with larger uncertainties) RS measurements using high-performance spectrometry. This indicates that remotely sensed solar-induced F is a meaningful signal that can be used to expand the possibilities of assessing the physiological status of vegetation at different spatial and temporal scales. Using measured hyperspectral data to invert a physically based model, the effects of pigment content, leaf/canopy structural properties and physiology were effectively discriminated, and their combined observation over time led to the recognition of dynamic patterns of stress adaptation and stress recovery in the plants. Putting this into the perspective of a repeated (or continuous) observation through RS platforms, it will be possible to characterize stress-specific patterns and to effectively distinguish between acute stress events and prolonged stress phases, monitoring their implications on the long-term functioning of the vegetation.

Overall, the results achieved in this thesis foster the use of hyperspectral RS to obtain information about plant status. In particular, they indicate that F yields

coupled with complementary RS parameters, can be effective indicators of the dynamic behavior of the photosynthetic machinery of the plants. Ground-based RS platforms continue to provide a solid basis for studying vegetation status, and are still fundamental tools to calibrate and validate airborne or satellite products. Nevertheless, they usually lack the spatial distribution given by the other two. On the other hand, automatic ground-based instruments can provide measurements with a high temporal resolution to fill the gap between two consecutive satellite or airborne overpasses. This stresses the need for a RS multi-scale approach to effectively understand and monitor vegetation dynamics at a relevant scale. The amount of multi-source hyperspectral data available is quickly increasing, also driven by the hyperspectral satellite missions to be launched in the next years. Prolonged combined measurements of solar-induced chlorophyll a fluorescence (F) and photosynthesis proxies (*e.g.*, GPP) at various scales are expected to enforce the experimental evidence of a functional link between F and photosynthesis, but flexible modeling frameworks will be compelling tools to ingest, combine and exploit this massive and diverse amount of data. Within this context, additional effort in building process based biophysical models able to cope with a wide variety of stressors and environmental conditions, will be mandatory to unravel the full potential of higher level RS products such as Φ_F for plant status monitoring.

BIBLIOGRAPHY

Ač, A., Z. Malenovský, J. Olejníčková, A. Gallé, U. Rascher, and G. Mohammed (2015). "Meta-analysis assessing potential of steady-state chlorophyll fluorescence for remote sensing detection of plant water, temperature and nitrogen stress". In: *Remote Sensing of Environment* 168, pages 420–436 (cited on pages 6, 13, 33, 36, 43).

Acosta, M., R. Juszczak, B. Chojnicki, M. Pavelka, K. Havránková, J. Lesny, L. Krupková, M. Urbaniak, K. Machačová, and J. Olejnik (2017). "CO2 Fluxes from Different Vegetation Communities on a Peatland Ecosystem". In: *Wetlands* 37.3, pages 423–435. DOI: 10.1007/s13157-017-0878-4 (cited on page 53).

Alonso, L., L. Gómez-Chova, J. Vila-Francés, J. Amorós-López, L. Guanter, J. Calpe, and J. Moreno (2008). "Improved fraunhofer line discrimination method for vegetation fluorescence quantification". In: *IEEE Geoscience and Remote Sensing Letters* 5.4, pages 620–624. DOI: 10.1109/LGRS.2008.2001180 (cited on pages 49, 50, 80).

Baret, F., O. Hagolle, B. Geiger, P. Bicheron, B. Miras, M. Huc, B. Berthelot, F. Niño, M. Weiss, O. Samain, J. L. Roujean, and M. Leroy (2007). "LAI, fAPAR and fCover CYCLOPES global products derived from VEGETATION. Part 1: Principles of the algorithm". In: *Remote Sensing of Environment* 110.3, pages 275–286. DOI: 10.1016/j.rse.2007.02.018 (cited on page 39).

Beeck, M. O. de, B. Gielen, I. Jonckheere, R. Samson, I. A. Janssens, and R. Ceulemans (2010). "Needle age-related and seasonal photosynthetic capacity variation is negligible for modelling yearly gas exchange of a sparse temperate Scots pine forest". In: *Biogeosciences* 7.1, pages 199–215. DOI: 10.5194/bgd-6-9737-2009 (cited on page 12).

Beer, C., M. Reichstein, E. Tomelleri, P. Ciais, M. Jung, N. Carvalhais, C. Rodenbeck, M. A. Arain, D. Baldocchi, G. B. Bonan, A. Bondeau, A. Cescatti, G. Lasslop, A. Lindroth, M. Lomas, S. Luyssaert, H. Margolis, K. W. Oleson, O. Roupsard, E. Veenendaal, N. Viovy, C. Williams, F. I. Woodward, and D. Papale (2010). "Terrestrial Gross Carbon Dioxide Uptake: Global Distribution and Covariation with Climate". In: *Science* 329.5993, pages 834–838. DOI: 10.1126/science.1184984 (cited on pages 1, 4).

Berk, A., P. Conforti, R. Kennett, T. Perkins, F. Hawes, and J. van den Bosch (2014). "MODTRAN6: a major upgrade of the MODTRAN radiative transfer code".

In: *SPIE Defense+ Security* 9088, 90880H. DOI: 10.1117/12.2050433 (cited on page 78).

Berni, J., P. Zarco-Tejada, L. Suarez, and E. Fereres (2009). "Thermal and Narrowband Multispectral Remote Sensing for Vegetation Monitoring From an Unmanned Aerial Vehicle". In: *IEEE Transactions on Geoscience and Remote Sensing* 47.3, pages 722–738. DOI: 10.1109/TGRS.2008.2010457 (cited on page 43).

Bond, B. J. (2000). "Age-related changes in photosynthesis of woody plants". In: *Trends in Plant Science* 5.8, pages 349–353. DOI: 10.1016/S1360-1385(00)01691-5 (cited on page 12).

Brook, B. W., L. W. Traill, and C. J. Bradshaw (2006). "Minimum viable population sizes and global extinction risk are unrelated". In: *Ecology Letters* 9.4, pages 375–382. DOI: 10.1111/j.1461-0248.2006.00883.x (cited on page 25).

Burns, R. M. and B. H. Honkala (1990). "Silvics of North America: 1. Conifers; 2. Hardwoods". In: *Agriculture Handbook 654*. Volume 2. Washington, D.C.: U.S. Dept. of Agriculture, Forest Service, page 877. DOI: 10.1093/infdis/jis908 (cited on page 36).

Busetto, L., M. Meroni, and R. Colombo (2008). "Combining medium and coarse spatial resolution satellite data to improve the estimation of sub-pixel NDVI time series". In: *Remote Sensing of Environment* 112.1, pages 118–131. DOI: 10.1016/j.rse.2007.04.004 (cited on page 39).

Butler, W. L. (1978). "Energy Distribution in the Photochemical Apparatus of Photosynthesis". In: *Annual Review of Plant Physiology* 29.1, pages 345–378. DOI: 10.1146/annurev.pp.29.060178.002021 (cited on page 71).

Carlson, T. N. and D. A. Ripley (1997). "On the relation between NDVI, fractional vegetation cover, and leaf area index". In: *Remote Sensing of Environment* 62.3, pages 241–252. DOI: 10.1016/S0034-4257(97)00104-1 (cited on page 39).

Carter, G. A., J. H. Jones, R. J. Mitchell, and C. H. Brewer (1996). "Detection of solar-excited chlorophyll a fluorescence and leaf photosynthetic capacity using a Fraunhofer Line Radiometer". In: *Remote Sensing of Environment* 55.1, pages 89–92. DOI: 10.1016/0034-4257(95)00192-1 (cited on page 44).

Cerovic, Z. G., Y. Goulas, M. Gorbunov, J. M. Briantais, L. Camenen, and I. Moya (1996). "Fluorosensing of water stress in plants: Diurnal changes of the mean lifetime and yield of chlorophyll fluorescence, measured simultaneously and at distance with a τ-LIDAR and a modified PAM-fluorimeter, in maize, sugar beet, and kalanchoe". In: *Remote Sensing of Environment* 58.3, pages 311–321. DOI: 10.1016/S0034-4257(96)00076-4 (cited on page 13).

Chapin III, F. S., A. J. Bloom, C. B. Field, and R. H. Waring (1987). "Plant Responses to Multiple Environmental Factors Plant Responses to Multiple Environmental Factors Physiological ecology provides tools for studying how interacting envi-

ronmental resources control plant growth". In: *Source: BioScience* 37.1, pages 49–57 (cited on page 3).

Chappelle, E. W., M. S. Kim, and J. E. McMurtrey (1992). "Ratio analysis of reflectance spectra (RARS): An algorithm for the remote estimation of the concentrations of chlorophyll A, chlorophyll B, and carotenoids in soybean leaves". In: *Remote Sensing of Environment* 39.3, pages 239–247. DOI: 10.1016/0034-4257(92)90089-3 (cited on page 17).

Chen, J. M. and J. Cihlar (1996). "Retrieving leaf area index of boreal conifer forests using landsat TM images". In: *Remote Sensing of Environment* 55.2, pages 153–162. DOI: 10.1016/0034-4257(95)00195-6 (cited on page 39).

Cheng, Y. B., E. M. Middleton, Q. Zhang, K. F. Huemmrich, P. K. E. Campbell, L. A. Corp, B. D. Cook, W. P. Kustas, and C. S. Daughtry (2013). "Integrating solar induced fluorescence and the photochemical reflectance index for estimating gross primary production in a cornfield". en. In: *Remote Sensing* 5.12, pages 6857–6879. DOI: 10.3390/rs5126857 (cited on pages 13, 38).

Chojnicki, B. H., M. Michalak, M. Acosta, R. Juszczak, J. Augustin, M. Drösler, and J. Olejnik (2010). "Measurements of carbon dioxide fluxes by chamber method at the Rzecin wetland ecosystem, Poland". In: *Polish Journal of Environmental Studies* 19.2, pages 283–291 (cited on page 53).

Cogliati, S., M. Rossini, T. Julitta, M. Meroni, A. Schickling, A. Burkart, F. Pinto, U. Rascher, and R. Colombo (2015a). "Continuous and long-term measurements of reflectance and sun-induced chlorophyll fluorescence by using novel automated field spectroscopy systems". In: *Remote Sensing of Environment* 164, pages 270–281. DOI: 10.1016/j.rse.2015.03.027 (cited on page 42).

Cogliati, S., W. Verhoef, S. Kraft, N. Sabater, L. Alonso, J. Vicent, J. Moreno, M. Drusch, and R. Colombo (2015b). "Retrieval of sun-induced fluorescence using advanced spectral fitting methods". In: *Remote Sensing of Environment* 169, pages 344–357. DOI: 10.1016/j.rse.2015.08.022 (cited on pages 4, 5, 8, 19, 52, 70, 72, 75, 83, 85).

Cogliati, S., W. Verhoef, S. Kraft, N. Sabater, L. Alonso, J. Moreno, U. Rascher, M. Drusch, and R. Colombo (2016). "Spectrum Fitting - a potential fluorescence retrieval for the FLEX mission". Presented at European Space Agency Living Planet Symposium, 9-13 May 2016, Prague, Czech Republic (cited on page 72).

Colombo, R., M. Meroni, and M. Rossini (2016). "Development of Fluorescence Indices to Minimise the Effects of Canopy Structural Parameters". In: *Annali di Botanica* 6, pages 93–99. DOI: 10.4462/annbotrm-13273 (cited on page 14).

Cook, B. D., L. A. Corp, R. F. Nelson, E. M. Middleton, D. C. Morton, J. T. McCorkel, J. G. Masek, K. J. Ranson, V. Ly, and P. M. Montesano (2013). "NASA goddard's LiDAR, hyperspectral and thermal (G-LiHT) airborne imager". In: *Remote Sensing* 5.8, pages 4045–4066. DOI: 10.3390/rs5084045 (cited on page 18).

Damm, A., L. Guanter, V. C. Laurent, M. E. Schaepman, A. Schickling, and U. Rascher (2014). "FLD-based retrieval of sun-induced chlorophyll fluorescence from medium spectral resolution airborne spectroscopy data". In: *Remote Sensing of Environment* 147, pages 256–266. DOI: 10.1016/j.rse.2014.03.009 (cited on pages 42, 51).

Damm, A., L. Guanter, E. Paul-Limoges, C. van der Tol, A. Hueni, N. Buchmann, W. Eugster, C. Ammann, and M. E. Schaepman (2015a). "Far-red sun-induced chlorophyll fluorescence shows ecosystem-specific relationships to gross primary production: An assessment based on observational and modeling approaches". In: *Remote Sensing of Environment* 166, pages 91–105. DOI: 10.1016/j.rse.2015.06.004 (cited on page 13).

Damm, A., L. Guanter, W. Verhoef, D. Schläpfer, S. Garbari, and M. E. Schaepman (2015b). "Impact of varying irradiance on vegetation indices and chlorophyll fluorescence derived from spectroscopy data". In: *Remote Sensing of Environment* 156, pages 202–215. DOI: 10.1016/j.rse.2014.09.031 (cited on pages 13, 21, 49, 50).

Damm, A., J. Elber, A. Erler, B. Gioli, K. Hamdi, R. Hutjes, M. Kosvancova, M. Meroni, F. Miglietta, A. Moersch, J. Moreno, A. Schickling, R. Sonnenschein, T. Udelhoven, S. van der Linden, P. Hostert, and U. Rascher (2010). "Remote sensing of sun-induced fluorescence to improve modeling of diurnal courses of gross primary production (GPP)". In: *Global Change Biology* 16.1, pages 171–186. DOI: 10.1111/j.1365-2486.2009.01908.x (cited on pages 5, 13, 20, 36, 43, 70).

Dash, J. and P. J. Curran (2007). "Evaluation of the MERIS terrestrial chlorophyll index (MTCI)". In: *Advances in Space Research* 39.1, pages 100–104. DOI: 10.1016/j.asr.2006.02.034 (cited on page 47).

Daughtry, C. S., L. L. Biehl, and K. J. Ranson (1989). "A new technique to measure the spectral properties of conifer needles". In: *Remote Sensing of Environment* 27.1, pages 81–91. DOI: 10.1016/0034-4257(89)90039-4 (cited on page 17).

Daumard, F., S. Champagne, A. Fournier, Y. Goulas, A. Ounis, J. F. Hanocq, and I. Moya (2010). "A field platform for continuous measurement of canopy fluorescence". In: *IEEE Transactions on Geoscience and Remote Sensing* 48.9, pages 3358–3368. DOI: 10.1109/TGRS.2010.2046420 (cited on pages 6, 13, 42).

Demmig-Adams, B. and W. W. Adams (2006). "Photoprotection in an ecological context: The remarkable complexity of thermal energy dissipation". In: *New Phytologist* 172.1, pages 11–21. DOI: 10.1111/j.1469-8137.2006.01835.x (cited on page 3).

D'Odorico, P., A. Gonsamo, B. Pinty, N. Gobron, N. Coops, E. Mendez, and M. E. Schaepman (2014). "Intercomparison of fraction of absorbed photosynthetically active radiation products derived from satellite data over Europe". In: *Remote*

Sensing of Environment 142, pages 141–154. DOI: 10.1016/j.rse.2013.12.005 (cited on page 20).

Domec, J. C., J. S. King, E. Ward, A. Christopher Oishi, S. Palmroth, A. Radecki, D. M. Bell, G. Miao, M. Gavazzi, D. M. Johnson, S. G. McNulty, G. Sun, and A. Noormets (2015). "Conversion of natural forests to managed forest plantations decreases tree resistance to prolonged droughts". In: *Forest Ecology and Management* 355, pages 58–71. DOI: 10.1016/j.foreco.2015.04.012 (cited on page 15).

Domec, J. C., G. Sun, A. Noormets, M. J. Gavazzi, E. A. Treasure, E. Cohen, J. J. Swenson, S. G. McNulty, and J. S. King (2012). "A comparison of three methods to estimate evapotranspiration in two contrasting loblolly pine plantations: Age-related changes in water use and drought sensitivity of evapotranspiration components". In: *Forest Science* 58.5, pages 497–512. DOI: 10.5849/forsci.11-051 (cited on pages 15, 35, 36).

Domec, J.-C. and B. L. Gartner (2003). "Relationship between growth rates and xylem hydraulic characteristics in young, mature and old-growth ponderosa pine trees". In: *Plant, cell & environment* 26, pages 471–483. DOI: 10.1046/j.1365-3040.2003.00978.x (cited on page 12).

Donohue, R. J., M. L. Roderick, and T. R. McVicar (2008). "Deriving consistent long-term vegetation information from AVHRR reflectance data using a cover-triangle-based framework". In: *Remote Sensing of Environment* 112.6, pages 2938–2949. DOI: 10.1016/j.rse.2008.02.008 (cited on page 20).

Drake, J. E., S. C. Davis, L. M. Raetz, and E. H. Delucia (2011). "Mechanisms of age-related changes in forest production: The influence of physiological and successional changes". In: *Global Change Biology* 17.4, pages 1522–1535. DOI: 10.1111/j.1365-2486.2010.02342.x (cited on pages 12, 35).

Drake, J. E., L. M. Raetz, S. C. Davis, and E. H. Delucia (2010). "Hydraulic limitation not declining nitrogen availability causes the age-related photosynthetic decline in loblolly pine (Pinus taeda L.)" In: *Plant, Cell and Environment* 33.10, pages 1756–1766. DOI: 10.1111/j.1365-3040.2010.02180.x (cited on pages 9, 17, 25, 35).

Drusch, M., J. Moreno, U. D. Bello, R. Franco, Y. Goulas, A. Huth, S. Kraft, E. M. Middleton, F. Miglietta, G. Mohammed, L. Nedbal, U. Rascher, D. Schüttemeyer, and W. Verhoef (2017). "Concept — ESA ' s Earth Explorer 8". In: *IEEE Trans. Geosci. Remote Sens.* 55.3, pages 1273–1284 (cited on pages 13, 43).

ESA (2015). *Report for mission selection: An Earth Explorer to observe vegetation fluorescence*. Technical report. ESA, page 192 (cited on page 23).

ESA (2017). *FLEX-EU Final Report, Technical Assistance for the Deployment of an advanced hyperspectral-imaging sensor during FLEX-EU Campaign*. Technical report (cited on page 22).

Féret, J. B., A. A. Gitelson, S. D. Noble, and S. Jacquemoud (2017). "PROSPECT-D: Towards modeling leaf optical properties through a complete lifecycle". In: *Remote Sensing of Environment* 193, pages 204–215. DOI: 10.1016/j.rse.2017.03.004 (cited on page 77).

Filella, I., A. Porcar-Castell, S. Munné-Bosch, J. Bäck, M. F. Garbulsky, J. Peñuelas, J. B. Ck, and J. Pe (2009). "International Journal of Remote Sensing PRI assessment of long-term changes in carotenoids/chlorophyll ratio and short-term changes in de-epoxidation state of the xanthophyll cycle PRI assessment of long-term changes in carotenoids/chlorophyll ratio and s". In: *International Journal of Remote Sensing* 30, pages 17–4443. DOI: 10.1080/01431160802575661 (cited on page 43).

Filella, I., T. Amaro, J. L. Araus, and J. Penuelas (1996). "Relationship between photosynthetic radiation-use efficiency of barley canopies and the photochemical reflectance index (PRI)". In: *Physiologia Plantarum* 96.2, pages 211–216. DOI: 10.1111/j.1399-3054.1996.tb00204.x (cited on page 43).

Flexas, J., J. M. Escalona, S. Evain, J. Gulías, I. Moya, C. B. Osmond, and H. Medrano (2002). "Steady-state chlorophyll fluorescence (Fs) measurements as a tool to follow variations of net CO2 assimilation and stomatal conductance during water-stress in C3 plants". In: *European Space Agency, (Special Publication) ESA SP* 527, pages 26–29. DOI: 10.1034/j.1399-3054.2002.1140209.x (cited on pages 3, 36).

Fournier, A., F. Daumard, S. Champagne, A. Ounis, Y. Goulas, and I. Moya (2012). "Effect of canopy structure on sun-induced chlorophyll fluorescence". In: *ISPRS Journal of Photogrammetry and Remote Sensing* 68.1, pages 112–120. DOI: 10.1016/j.isprsjprs.2012.01.003 (cited on page 13).

Franck, F., P. Juneau, and R. Popovic (2002). "Resolution of the Photosystem I and Photosystem II contributions to chlorophyll fluorescence of intact leaves at room temperature". In: *Biochimica et Biophysica Acta* 1556, pages 239–246 (cited on page 3).

Frankenberg, C., A. Butz, and G. C. Toon (2011). "Disentangling chlorophyll fluorescence from atmospheric scattering effects in O_2-A-band spectra of reflected sun-light". In: *Geophysical Research Letters* 38.3, pages 1–5. DOI: 10.1029/2010GL045896 (cited on page 42).

Frankenberg, C., J. B. Fisher, J. Worden, G. Badgley, S. S. Saatchi, J. E. Lee, G. C. Toon, A. Butz, M. Jung, A. Kuze, and T. Yokota (2011). "New global observations of the terrestrial carbon cycle from GOSAT: Patterns of plant fluorescence with gross primary productivity". In: *Geophysical Research Letters* 38.17. DOI: 10.1029/2011GL048738 (cited on page 42).

Franklin, J., J. M. Serra-Diaz, A. D. Syphard, and H. M. Regan (2016). "Global change and terrestrial plant community dynamics". In: *Proceedings of the National*

Academy of Sciences 113.14, pages 3725–3734. DOI: 10.1073/pnas.1519911113 (cited on page 1).

Fuentes, S., R. de Bei, J. Pech, and S. Tyerman (2012). "Computational water stress indices obtained from thermal image analysis of grapevine canopies". In: *Irrigation Science* 30.6, pages 523–536. DOI: 10.1007/s00271-012-0375-8 (cited on page 43).

Gamon, J. A., C. B. Field, W. Bilger, O. Björkman, A. L. Fredeen, and J. Peñuelas (1990). "Remote sensing of the xanthophyll cycle and chlorophyll fluorescence in sunflower leaves and canopies". In: *Oecologia* 85.1, pages 1–7. DOI: 10.1007/BF00317336 (cited on page 65).

Gamon, J. A., J. Peñuelas, and C. B. Field (1992). "A narrow-waveband spectral index that tracks diurnal changes in photosynthetic efficiency". In: *Remote Sensing of Environment* 41.1, pages 35–44. DOI: 10.1016/0034-4257(92)90059-S (cited on pages 43, 47, 65).

Garbulsky, M. F., J. Peñuelas, J. Gamon, Y. Inoue, and I. Filella (2011). "The photochemical reflectance index (PRI) and the remote sensing of leaf, canopy and ecosystem radiation use efficiencies. A review and meta-analysis". In: *Remote Sensing of Environment* 115.2, pages 281–297. DOI: 10.1016/j.rse.2010.08.023 (cited on pages 43, 65).

Garbulsky, M. F., J. Peñuelas, D. Papale, J. Ardö, M. L. Goulden, G. Kiely, A. D. Richardson, E. Rotenberg, E. M. Veenendaal, and I. Filella (2010). "Patterns and controls of the variability of radiation use efficiency and primary productivity across terrestrial ecosystems". In: *Global Ecology and Biogeography* 19.2, pages 253–267. DOI: 10.1111/j.1466-8238.2009.00504.x. arXiv: arXiv:1011.1669v3 (cited on page 72).

Garzonio, R., B. D. Mauro, R. Colombo, and S. Cogliati (2017). "Surface Reflectance and Sun-Induced Fluorescence Spectroscopy Measurements Using a Small Hyperspectral UAS". In: *Remote Sensing* 9.5, page 472. DOI: 10.3390/rs9050472 (cited on page 4).

Gastellu-Etchegorry, J. P., N. Lauret, T. Yin, L. Landier, A. Kallel, Z. Malenovský, A. Al Bitar, J. Aval, S. Benhmida, J. Qi, G. Medjdoub, J. Guilleux, E. Chavanon, B. Cook, D. Morton, N. Chrysoulakis, and Z. Mitraka (2017). "DART: Recent advances in remote sensing data modeling with atmosphere, polarization, and chlorophyll fluorescence". In: *IEEE Journal of Selected Topics in Applied Earth Observations and Remote Sensing* 10.6, pages 2640–2649. DOI: 10.1109/JSTARS.2017.2685528 (cited on page 40).

Genty, B., J. Wonders, and N. R. Baker (1990). "Non-photochemical quenching of Fo in leaves is emission wavelength dependent: consequences for quenching analysis and its interpretation". In: *Photosynthesis Research* 26.2, pages 133–139. DOI: 10.1007/BF00047085 (cited on page 3).

Gitelson, A. A., C. Buschmann, and H. K. Lichtenthaler (1998). "Leaf Chlorophyll Fluorescence Corrected for Re-absorption by Means of Absorption and Reflectance Measurements". In: *Journal of Plant Physiology* 152.2-3, pages 283–296. DOI: 10.1016/S0176-1617(98)80143-0 (cited on page 6).

Gitelson, A. A. and J. A. Gamon (2015). "The need for a common basis for defining light-use efficiency: Implications for productivity estimation". In: *Remote Sensing of Environment* 156, pages 196–201. DOI: 10.1016/j.rse.2014.09.017 (cited on pages 36, 72).

Gobron, N., B. Pinty, O. Aussedat, J. M. Chen, W. B. Cohen, R. Fensholt, V. Gond, K. F. Huemmrich, T. Lavergne, F. Mélin, J. L. Privette, I. Sandholt, M. Taberner, D. P. Turner, M. M. Verstraete, and J. L. Widlowski (2006). "Evaluation of fraction of absorbed photosynthetically active radiation products for different canopy radiation transfer regimes: Methodology and results using Joint Research Center products derived from SeaWiFS against ground-based estimations". In: *Journal of Geophysical Research Atmospheres* 111.13, pages 1–15. DOI: 10.1029/2005JD006511 (cited on page 20).

Goulas, Y., A. Fournier, F. Daumard, S. Champagne, A. Ounis, O. Marloie, and I. Moya (2017). "Gross Primary Production of a Wheat Canopy Relates Stronger to Far Red Than to Red Solar-Induced Chlorophyll Fluorescence". In: *Remote Sensing* 9.1, page 97. DOI: 10.3390/rs9010097 (cited on pages 13, 38).

Goward, S. N. and K. F. Huemmrich (1992). "Vegetation canopy PAR absorptance and the normalized difference vegetation index: An assessment using the SAIL model". In: *Remote Sensing of Environment* 39.2, pages 119–140. DOI: 10.1016/0034-4257(92)90131-3 (cited on page 20).

Gower, S. T., R. E. McMurtrie, and D. Murty (1996). *Aboveground net primary production decline with stand age: Potential causes*. DOI: 10.1016/0169-5347(96)10042-2 (cited on page 12).

Greenwood, M. S. (1995). "Juvenility and maturation in conifers: current concepts." In: *Tree physiology* 15.7_8, pages 433–438. DOI: 10.1093/treephys/15.7-8.433 (cited on page 12).

Guanter, L., I. Aben, P. Tol, J. M. Krijger, A. Hollstein, P. Köhler, A. Damm, J. Joiner, C. Frankenberg, and J. Landgraf (2015). "Potential of the TROPOspheric Monitoring Instrument (TROPOMI) onboard the Sentinel-5 Precursor for the monitoring of terrestrial chlorophyll fluorescence". In: *Atmospheric Measurement Techniques* 8.3, pages 1337–1352. DOI: 10.5194/amt-8-1337-2015 (cited on pages 4, 70).

Guanter, L., L. Alonso, L. Gómez-Chova, M. Meroni, R. Preusker, J. Fischer, and J. Moreno (2010). "Developments for vegetation fluorescence retrieval from spaceborne high-resolution spectrometry in the O2-A and O2-B absorption bands".

In: *Journal of Geophysical Research Atmospheres* 115.19. DOI: 10.1029/2009JD013716 (cited on pages 4, 70).

Guanter, L., Y. Zhang, M. Jung, J. Joiner, M. Voigt, J. A. Berry, C. Frankenberg, A. R. Huete, P. Zarco-Tejada, J.-E. Lee, M. S. Moran, G. Ponce-Campos, C. Beer, G. Camps-Valls, N. Buchmann, D. Gianelle, K. Klumpp, A. Cescatti, J. M. Baker, and T. J. Griffis (2014a). "Global and time-resolved monitoring of crop photosynthesis with chlorophyll fluorescence". en. In: *Proceedings of the National Academy of Sciences* 111.14, E1327–E1333. DOI: 10.1073/pnas.1320008111 (cited on pages 5, 43, 70).

Guanter, L., Y. Zhang, M. Jung, J. Joiner, M. Voigt, J. A. Berry, C. Frankenberg, A. R. Huete, P. Zarco-Tejada, J.-E. Lee, M. S. Moran, G. Ponce-Campos, C. Beer, G. Camps-Valls, N. Buchmann, D. Gianelle, K. Klumpp, A. Cescatti, J. M. Baker, and T. J. Griffis (2014b). "Reply to Magnani et al.: Linking large-scale chlorophyll fluorescence observations with cropland gross primary production". In: *Proceedings of the National Academy of Sciences* 111.25, E2511–E2511. DOI: 10.1073/pnas.1406996111 (cited on pages 13, 21).

Guanter, L., L. Alonso, L. Gómez-Chova, J. Amorós-López, J. Vila, and J. Moreno (2007). "Estimation of solar-induced vegetation fluorescence from space measurements". In: *Geophysical Research Letters* 34.8, page L08401. DOI: 10.1029/2007GL029289 (cited on page 51).

Guanter, L., C. Frankenberg, A. Dudhia, P. E. Lewis, J. Gómez-Dans, A. Kuze, H. Suto, and R. G. Grainger (2012). "Retrieval and global assessment of terrestrial chlorophyll fluorescence from GOSAT space measurements". In: *Remote Sensing of Environment* 121, pages 236–251. DOI: 10.1016/j.rse.2012.02.006 (cited on pages 5, 19, 42).

Guanter, L., M. Rossini, R. Colombo, M. Meroni, C. Frankenberg, J. E. Lee, and J. Joiner (2013). "Using field spectroscopy to assess the potential of statistical approaches for the retrieval of sun-induced chlorophyll fluorescence from ground and space". In: *Remote Sensing of Environment* 133, pages 52–61. DOI: 10.1016/j.rse.2013.01.017 (cited on page 19).

Gutman, G. and A. Ignatov (1998). "The derivation of the green vegetation fraction from NOAA/AVHRR data for use in numerical weather prediction models". In: *International Journal of Remote Sensing* 19.8, pages 1533–1543. DOI: 10.1080/014311698215333 (cited on page 39).

Hatfield, J. L., G. Asrar, and E. T. Kanemasu (1984). "Intercepted photosynthetically active radiation estimated by spectral reflectance". In: *Remote Sensing of Environment* 14.1-3, pages 65–75. DOI: 10.1016/0034-4257(84)90008-7 (cited on page 20).

Hernández-Clemente, R., P. R. North, A. Hornero, and P. J. Zarco-Tejada (2017). "Assessing the effects of forest health on sun-induced chlorophyll fluorescence

using the FluorFLIGHT 3-D radiative transfer model to account for forest structure". In: *Remote Sensing of Environment* 193, pages 165–179. DOI: 10.1016/j.rse.2017.02.012 (cited on pages 14, 22, 38, 40, 72, 92).

Hoffmann, M., N. Jurisch, E. Albiac Borraz, U. Hagemann, M. Drösler, M. Sommer, and J. Augustin (2015). "Automated modeling of ecosystem CO2 fluxes based on periodic closed chamber measurements: A standardized conceptual and practical approach". In: *Agricultural and Forest Meteorology* 200, pages 30–45. DOI: 10.1016/j.agrformet.2014.09.005 (cited on page 53).

Hoge, F. E., R. N. Swift, and J. K. Yungel (1983). "Feasibility of airborne detection of laser-induced fluorescence emissions from green terrestrial plants." In: *Applied optics* 22.19, page 2991. DOI: 10.1364/AO.22.002991 (cited on page 13).

Hubbard, R. M., B. J. Bond, and M. G. Ryan (1999). "Evidence that hydraulic conductance limits photosynthesis in old Pinus ponderosa trees". In: *Tree Physiology* 19.3, pages 165–172. DOI: 10.1093/treephys/19.3.165 (cited on page 12).

Introna, L. D. and D. Wood (2004). "Picturing algorithmic surveillance: The politics of facial recognition systems". In: *Surveillance and Society* 2.2-3, pages 177–198. DOI: 10.1017/CBO9781107415324.004. arXiv: arXiv:1011.1669v3 (cited on page 13).

Jacquemoud, S. and F. Baret (1990). "PROSPECT: A model of leaf optical properties spectra". In: *Remote Sensing of Environment* 34.2, pages 75–91. DOI: 10.1016/0034-4257(90)90100-Z (cited on pages 7, 77).

Jacquemoud, S., W. Verhoef, F. Baret, C. Bacour, P. J. Zarco-Tejada, G. P. Asner, C. François, and S. L. Ustin (2009). "PROSPECT + SAIL models: A review of use for vegetation characterization". In: *Remote Sensing of Environment* 113.SUPPL. 1, S56–S66. DOI: 10.1016/j.rse.2008.01.026 (cited on page 7).

Jiang, C. and F. Hongliang (2012). "Modeling Soil Reflectance Using a Global Spectral Library". In: *Agu* (cited on page 77).

Jiménez-Muñoz, J., J. Sobrino, L. Guanter, J. Moreno, A. Plaza, and P. Martínez (2005). "Fractional Vegetation Cover Estimation from PROBA/CHRIS Data: Methods, Analysis of Angular Effects and Application to the Land Surface Emissivity." In: (cited on page 39).

Joiner, J., Y. Yoshida, A. P. Vasilkov, K. Schaefer, M. Jung, L. Guanter, Y. Zhang, S. Garrity, E. M. Middleton, K. F. Huemmrich, L. Gu, and L. Belelli Marchesini (2014). "The seasonal cycle of satellite chlorophyll fluorescence observations and its relationship to vegetation phenology and ecosystem atmosphere carbon exchange". In: *Remote Sensing of Environment* 152, pages 375–391. DOI: 10.1016/j.rse.2014.06.022 (cited on page 13).

Joiner, J., Y. Yoshida, A. P. Vasilkov, Y. Yoshida, L. A. Corp, and E. M. Middleton (2011). "First observations of global and seasonal terrestrial chlorophyll fluores-

cence from space". In: *Biogeosciences* 8.3, pages 637–651. DOI: 10.5194/bg-8-637-2011 (cited on page 42).

Joiner, J., Y. Yoshida, L. Guanter, and E. M. Middleton (2016). "New methods for the retrieval of chlorophyll red fluorescence from hyperspectral satellite instruments: Simulations and application to GOME-2 and SCIAMACHY". In: *Atmospheric Measurement Techniques* 9.8, pages 3939–3967. DOI: 10.5194/amt-9-3939-2016 (cited on pages 4, 6, 38, 42).

Julitta, T., L. Corp, M. Rossini, A. Burkart, S. Cogliati, N. Davies, M. Hom, A. Mac Arthur, E. Middleton, U. Rascher, A. Schickling, and R. Colombo (2016). "Comparison of Sun-Induced Chlorophyll Fluorescence Estimates Obtained from Four Portable Field Spectroradiometers". In: *Remote Sensing* 8.2, page 122. DOI: 10.3390/rs8020122 (cited on pages 4, 8).

Juszczak, R. and J. Augustin (2013). "Exchange of the greenhouse gases methane and nitrous oxide between the atmosphere and a temperate peatland in Central Europe". In: *Wetlands* 33.5, pages 895–907. DOI: 10.1007/s13157-013-0448-3 (cited on pages 52, 53).

Knyazikhin, Y., M. A. Schull, P. Stenberg, M. Mottus, M. Rautiainen, Y. Yang, A. Marshak, P. Latorre Carmona, R. K. Kaufmann, P. Lewis, M. I. Disney, V. Vanderbilt, A. B. Davis, F. Baret, S. Jacquemoud, A. Lyapustin, and R. B. Myneni (2013). "Hyperspectral remote sensing of foliar nitrogen content". In: *Proceedings of the National Academy of Sciences* 110.3, E185–E192. DOI: 10.1073/pnas.1210196109 (cited on page 14).

Koffi, E. N., P. J. Rayner, A. J. Norton, C. Frankenberg, and M. Scholze (2015). "Investigating the usefulness of satellite-derived fluorescence data in inferring gross primary productivity within the carbon cycle data assimilation system". In: *Biogeosciences* 12.13, pages 4067–4084. DOI: 10.5194/bg-12-4067-2015 (cited on page 13).

Köhler, P., L. Guanter, H. Kobayashi, S. Walther, and W. Yang (2017). *Assessing the potential of sun-induced fluorescence and the canopy scattering coefficient to track large-scale vegetation dynamics in Amazon forests*. DOI: 10.1016/j.rse.2017.09.025 (cited on page 5).

Larcher, W. (1969). "The effect of enviromental and physiological variables on the carbon dioxide gas exchange of trees". In: *Photosynthetica* 3.2, pages 167–198 (cited on page 12).

Latifovic, R. and I. Olthof (2004). "Accuracy assessment using sub-pixel fractional error matrices of global land cover products derived from satellite data". In: *Remote Sensing of Environment* 90.2, pages 153–165. DOI: 10.1016/j.rse.2003.11.016 (cited on page 39).

Lee, J.-E., C. Frankenberg, C. van der Tol, J. A. Berry, L. Guanter, C. K. Boyce, J. B. Fisher, E. Morrow, J. R. Worden, S. Asefi, G. Badgley, and S. Saatchi (2013).

"Forest productivity and water stress in Amazonia: observations from GOSAT chlorophyll fluorescence". In: *Proceedings of the Royal Society B: Biological Sciences* 280.1761, pages 20130171–20130171. DOI: 10.1098/rspb.2013.0171 (cited on pages 6, 20, 43, 70).

Li, Z.-L., B.-H. Tang, H. Wu, H. Ren, G. Yan, Z. Wan, I. F. Trigo, and J. a Sobrino (2013). "Satellite-derived land surface temperature: Current status and perspectives". In: *Remote Sensing of Environment* 131, pages 14–37. DOI: 10.1016/j.rse.2012.12.008 (cited on page 53).

Lichtenthaler, H. K. and C. Buschmann (2001). "Chlorophylls and carotenoids: Measurement and characterization by UV-VIS spectroscopy". In: *Current protocols in food analytical chemistry* (cited on page 54).

Lichtenthaler, H. K. and U. Rinderle (1988). "The Role of Chlorophyll Fluorescence in The Detection of Stress Conditions in Plants". In: *C R C Critical Reviews in Analytical Chemistry* 19.sup1, S29–S85. DOI: 10.1080/15476510.1988.10401466 (cited on page 44).

Linkosalo, T., J. Heikkinen, P. Pulkkinen, and R. Mäkipää (2014). "Fluorescence measurements show stronger cold inhibition of photosynthetic light reactions in Scots pine compared to Norway spruce as well as during spring compared to autumn." In: *Frontiers in plant science* 5.June, page 264. DOI: 10.3389/fpls.2014.00264 (cited on page 12).

Liu, L., L. Guan, and X. Liu (2017). "Directly estimating diurnal changes in GPP for C3 and C4 crops using far-red sun-induced chlorophyll fluorescence". In: *Agricultural and Forest Meteorology* 232, pages 1–9. DOI: 10.1016/j.agrformet.2016.06.014 (cited on page 20).

Liu, W., J. Atherton, M. Mõttus, A. MacArthur, H. Teemu, K. Maseyk, I. Robinson, E. Honkavaara, and A. Porcar-Castell (2017). "UPSCALING OF SOLAR INDUCED CHLOROPHYLL FLUORESCENCE FROM LEAF TO CANOPY USING THE DART MODEL AND A REALISTIC 3D FOREST SCENE". In: *ISPRS - International Archives of the Photogrammetry, Remote Sensing and Spatial Information Sciences* XLII-3/W3, pages 107–111. DOI: 10.5194/isprs-archives-XLII-3-W3-107-2017 (cited on page 72).

Liu, X., L. Liu, S. Zhang, and X. Zhou (2015). "New spectral fitting method for full-spectrum solar-induced chlorophyll fluorescence retrieval based on principal components analysis". In: *Remote Sensing* 7.8, pages 10626–10645. DOI: 10.3390/rs70810626 (cited on pages 5, 71).

Liu, Z., H. Yan, K. Wang, T. Kuang, J. Zhang, L. Gui, X. An, and W. Chang (2004). "Crystal structure of spinach major light-harvesting complex at 2.72 A resolution". In: *Nature* 428.6980, pages 287–292. DOI: 10.1038/nature02373 (cited on page 1).

Louis, J., A. Ounis, J. M. Ducruet, S. Evain, T. Laurila, T. Thum, M. Aurela, G. Wingsle, L. Alonso, R. Pedros, and I. Moya (2005). "Remote sensing of sunlight-induced chlorophyll fluorescence and reflectance of Scots pine in the boreal forest during spring recovery". In: *Remote Sensing of Environment* 96.1, pages 37–48. DOI: 10.1016/j.rse.2005.01.013 (cited on page 38).

Maier, C. A., K. H. Johnsen, J. Butnor, L. W. Kress, and P. H. Anderson (2002). "Branch growth and gas exchange in 13-year-old loblolly pine (Pinus taeda) trees in response to elevated carbon dioxide concentration and fertilization". In: *Tree Physiology* 22.15-16, pages 1093–1106. DOI: 10.1093/treephys/22.15-16.1093 (cited on page 17).

Maier, S. W., K. P. Günther, and M. Stellmes (2003). "Sun-induced fluorescence: a new tool for precision farming". In: *Digital Imaging and Spectral Techniques: Applications to Precision Agriculture and Crop Physiology*, pages 209–222. DOI: 10.2134/asaspecpub66.c16 (cited on page 49).

Malenovský, Z., L. Homolová, R. Zurita-Milla, P. Lukeš, V. Kaplan, J. Hanuš, J.-P. Gastellu-Etchegorry, and M. E. Schaepman (2013). "Retrieval of spruce leaf chlorophyll content from airborne image data using continuum removal and radiative transfer". In: *Remote Sensing of Environment* 131, pages 85–102. DOI: 10.1016/j.rse.2012.12.015 (cited on page 21).

Meinzer, F. C., B. Lachenbruch, and T. E. Dawson (2011). "Size- and Age-Related Changes in Tree Structure and Function". In: *Tree Physiology* 4, page 514. DOI: 10.1007/978-94-007-1242-3 (cited on page 12).

Meroni, M., A. Barducci, S. Cogliati, F. Castagnoli, M. Rossini, L. Busetto, M. Migliavacca, E. Cremonese, M. Galvagno, R. Colombo, and U. M. Di Cella (2011). "The hyperspectral irradiometer, a new instrument for long-term and unattended field spectroscopy measurements". In: *Review of Scientific Instruments* 82.4, pages 1–10. DOI: 10.1063/1.3574360 (cited on pages 52, 74).

Meroni, M., L. Busetto, R. Colombo, L. Guanter, J. Moreno, and W. Verhoef (2010). "Performance of Spectral Fitting Methods for vegetation fluorescence quantification". In: *Remote Sensing of Environment* 114.2, pages 363–374. DOI: 10.1016/j.rse.2009.09.010 (cited on page 75).

Meroni, M. and R. Colombo (2006). "Leaf level detection of solar induced chlorophyll fluorescence by means of a subnanometer resolution spectroradiometer". In: *Remote Sensing of Environment* 103.4, pages 438–448. DOI: 10.1016/j.rse.2006.03.016 (cited on pages 5, 13, 52, 75).

Meroni, M., M. Rossini, L. Guanter, L. Alonso, U. Rascher, R. Colombo, and J. Moreno (2009). "Remote sensing of solar-induced chlorophyll fluorescence: Review of methods and applications". In: *Remote Sensing of Environment* 113.10, pages 2037–2051. DOI: 10.1016/j.rse.2009.05.003 (cited on pages 4, 33, 42, 49, 70).

Meroni, M., C. Atzberger, C. Vancutsem, N. Gobron, F. Baret, R. Lacaze, H. Eerens, and O. Leo (2013). "Evaluation of agreement between space remote sensing SPOT-VEGETATION fAPAR Time Series". In: *IEEE Transactions on Geoscience and Remote Sensing* 51.4, pages 1951–1962. DOI: 10.1109/TGRS.2012.2212447 (cited on pages 6, 72).

Meroni, M. and R. Colombo (2009). "3S: A novel program for field spectroscopy". In: *Computers and Geosciences* 35.7, pages 1491–1496. DOI: 10.1016/j.cageo.2009.01.005 (cited on pages 51, 52, 74).

Meroni, M., M. Rossini, V. Picchi, C. Panigada, S. Cogliati, C. Nali, and R. Colombo (2008). "Assessing Steady-state Fluorescence and PRI from Hyperspectral Proximal Sensing as Early Indicators of Plant Stress: The Case of Ozone Exposure". In: *Sensors* 8.3, pages 1740–1754. DOI: 10.3390/s8031740 (cited on pages 5, 13, 43, 70).

Middleton, E. M., U. Rascher, L. A. Corp, K. F. Huemmrich, B. D. Cook, A. Noormets, A. Schickling, F. Pinto, L. Alonso, A. Damm, L. Guanter, R. Colombo, P. K. Campbell, D. R. Landis, Q. Zhang, M. Rossini, D. Schuettemeyer, and R. Bianchi (2017). "The 2013 FLEX-US airborne campaign at the parker tract loblolly pine plantation in North Carolina, USA". In: *Remote Sensing* 9.6, pages 1–31. DOI: 10.3390/rs9060612 (cited on pages 14, 18).

Middleton, E., Y. Cheng, P. Campbell, K. Huemmrich, L. Corp, S. Bernardes, Q. Zhang, D. Landis, W. Kustas, C. Daughtry, and A. Russ (2015). "Multi-angle hyperspectral observations with SIF and PRI to detect plant stress & GPP in a cornfield". In: *Proceedings of the 9th EARSeL SIG Workshop on Imaging Spectroscopy, CD-ROM, Luxembourg City, Luxembourg, April 2015* (cited on pages 6, 38).

Middleton, E., K. Huemmrich, Y. Cheng, and H. Margolis (2012). "Spectral bio-indicators of photosynthetic efficiency and vegetation stress". In: *Hyperspectral Remote Sensing of Vegetation, Editors: P.S. Thenkabail, J.G. Lyon, and A. Huete* (cited on page 13).

Migliavacca, M., O. Perez-Priego, M. Rossini, T. S. El-Madany, G. Moreno, C. van der Tol, U. Rascher, A. Berninger, V. Bessenbacher, A. Burkart, A. Carrara, F. Fava, J. H. Guan, T. W. Hammer, K. Henkel, E. Juarez-Alcalde, T. Julitta, O. Kolle, M. P. Martín, T. Musavi, J. Pacheco-Labrador, A. Pérez-Burgueño, T. Wutzler, S. Zaehle, and M. Reichstein (2017). "Plant functional traits and canopy structure control the relationship between photosynthetic CO2 uptake and far-red sun-induced fluorescence in a Mediterranean grassland under different nutrient availability". In: *New Phytologist* 214.3, pages 1078–1091. DOI: 10.1111/nph.14437 (cited on page 70).

Monson, R. R. b and D. D. Baldocchi (2013). *Terrestrial biosphere-atmosphere fluxes*, pages 1–495. DOI: 10.1017/CBO9781139629218 (cited on page 1).

Monteith, J. L. (1972). "Solar Radiation and Productivity in Tropical Ecosystems". In: *The Journal of Applied Ecology* 9.3, page 747. DOI: 10.2307/2401901. arXiv: arXiv:1011.1669v3 (cited on pages 3, 6, 70).

Moya, I., L. Camenen, S. Evain, Y. Goulas, Z. G. Cerovic, G. Latouche, J. Flexas, and A. Ounis (2004). "A new instrument for passive remote sensing: 1. Measurements of sunlight-induced chlorophyll fluorescence". In: *Remote Sensing of Environment* 91.2, pages 186–197. DOI: 10.1016/j.rse.2004.02.012 (cited on page 13).

Moya, I., F. Daumard, N. Moise, A. Ounis, and Y. Goulas (2006). "First airborne multiwavelength passive chlorophyll fluorescence measurements over La Mancha (Spain) fields". In: *2nd International Symposium on Recent Advances in Quantitative Remote Sensing: RAQRS'II, 25–29th September, Torrent (Valencia), Spain* (cited on page 13).

Muller, P. (2001). "Non-Photochemical Quenching. A Response to Excess Light Energy". en. In: *Plant Physiology* 125.4, pages 1558–1566. DOI: 10.1104/pp.125.4.1558 (cited on page 65).

Myneni, R. B., S. Hoffman, Y. Knyazikhin, J. L. Privette, J. Glassy, Y. Tian, Y. Wang, X. Song, Y. Zhang, G. R. Smith, A. Lotsch, M. Friedl, J. T. Morisette, P. Votava, R. R. Nemani, and S. W. Running (2002). "Global products of vegetation leaf area and fraction absorbed PAR from year one of MODIS data". In: *Remote Sensing of Environment* 83.1-2, pages 214–231. DOI: 10.1016/S0034-4257(02)00074-3 (cited on page 20).

Myneni, R. B. and D. L. Williams (1994). "On the relationship between FAPAR and NDVI". In: *Remote Sensing of Environment* 49.3, pages 200–211. DOI: 10.1016/0034-4257(94)90016-7 (cited on page 20).

Noormets, A., M. Gavazzi, S. McNulty, J.-C. Domec, G. Sun, J. S. King, and J. Chen (2010). "Response of carbon fluxes to drought in a coastal plain loblolly pine forest". In: *Global Change Biology* 16.1, pages 272–287. DOI: 10.1111/j.1365-2486.2009.01928.x (cited on pages 15, 35).

North, P. R. J. (2002). "Estimation of fAPAR, LAI, and vegetation fractional cover from ATSR-2 imagery". In: *Remote Sensing of Environment* 80.1, pages 114–121. DOI: 10.1016/S0034-4257(01)00292-9 (cited on page 39).

Novick, K., R. Oren, P. Stoy, J. Y. Juang, M. Siqueira, and G. Katul (2009). "The relationship between reference canopy conductance and simplified hydraulic architecture". In: *Advances in Water Resources* 32.6, pages 809–819. DOI: 10.1016/j.advwatres.2009.02.004 (cited on page 15).

Olioso, A., M. Méthy, and B. Lacaze (1992). "Simulation of canopy fluorescence as a function of canopy structure and leaf fluorescence". In: *Remote Sensing of Environment* 41.2-3, pages 239–247. DOI: 10.1016/0034-4257(92)90081-T (cited on page 13).

Olthof, I. and R. H. Fraser (2007). "Mapping northern land cover fractions using Landsat ETM+". In: *Remote Sensing of Environment* 107.3, pages 496–509. DOI: 10.1016/j.rse.2006.10.009 (cited on page 39).

Oren, R., C. I. Hsieh, P. Stoy, J. Albertson, H. R. McCarthy, P. Harrell, and G. G. Katul (2006). "Estimating the uncertainty in annual net ecosystem carbon exchange: Spatial variation in turbulent fluxes and sampling errors in eddy-covariance measurements". In: *Global Change Biology* 12.5, pages 883–896. DOI: 10.1111/j.1365-2486.2006.01131.x (cited on page 15).

Osmond, C. B. (1994). "What is photoinhibition? Some insights from comparisons of shade and sun plants". In: *Photoinhibition of Photosynthesis from molecular mechanisms to the field* (cited on page 65).

Panigada, C., M. Rossini, M. Meroni, C. Cilia, L. Busetto, S. Amaducci, M. Boschetti, S. Cogliati, V. Picchi, F. Pinto, A. Marchesi, and R. Colombo (2014). "Fluorescence, PRI and canopy temperature for water stress detection in cereal crops". In: *International Journal of Applied Earth Observation and Geoinformation* 30.1, pages 167–178. DOI: 10.1016/j.jag.2014.02.002 (cited on pages 43, 65).

Panigada, C., M. Rossini, M. Meroni, R. Marzuoli, G. Gerosa, and R. Colombo (2009). "Indicators of ozone effects on Fagus sylvatica L. by means of spectroradiometric measurements". In: *Italian Journal of Remote Sensing* 41.2, pages 3–20. DOI: 10.5721/ItJRS20094121 (cited on pages 65, 66).

Papageorgiou, G. C. and Govindjee (2004). *Chlorophyll a fluorescence: a signature of photosynthesis*. Springer Science & Business Media, page 820 (cited on pages 4, 42).

Perez-Priego, O., J. Guan, M. Rossini, F. Fava, T. Wutzler, G. Moreno, N. Carvalhais, A. Carrara, O. Kolle, T. Julitta, M. Schrumpf, M. Reichstein, and M. Migliavacca (2015). "Sun-induced chlorophyll fluorescence and photochemical reflectance index improve remote-sensing gross primary production estimates under varying nutrient availability in a typical Mediterranean savanna ecosystem". In: *Biogeosciences* 12.21, pages 6351–6367. DOI: 10.5194/bg-12-6351-2015 (cited on pages 43, 53).

Pickett-Heaps, C. A., J. G. Canadell, P. R. Briggs, N. Gobron, V. Haverd, M. J. Paget, B. Pinty, and M. R. Raupach (2014). "Evaluation of six satellite-derived Fraction of Absorbed Photosynthetic Active Radiation (FAPAR) products across the Australian continent". In: *Remote Sensing of Environment* 140, pages 241–256. DOI: 10.1016/j.rse.2013.08.037 (cited on pages 6, 20, 39, 72).

Pignatti, S., V. Lapenna, A. Palombo, S. Pascucci, N. Pergola, and V. Cuomo (2011). "An advanced tool of the CNR IMAA EO facilities: Overview of the TASI-600 hyperspectral thermal spectrometer". In: *Workshop on Hyperspectral Image and Signal Processing, Evolution in Remote Sensing*. DOI: 10.1109/WHISPERS.2011.6080890 (cited on page 47).

Pinto, F., A. Damm, A. Schickling, C. Panigada, S. Cogliati, M. Müller-Linow, A. Balvora, and U. Rascher (2016). "Sun-induced chlorophyll fluorescence from high-resolution imaging spectroscopy data to quantify spatio-temporal patterns of photosynthetic function in crop canopies". In: *Plant Cell and Environment* 39.7, pages 1500–1512. DOI: 10.1111/pce.12710 (cited on pages 42, 51).

Plascyk, J. (1975). "The MK II Fraunhofer Line Discriminator (FLD-II) The MK II Fraunhofer Line Discriminator (FLD -II) for Airborne and Orbital Remote Sensing of Solar-Stimulated Luminescence". In: *Optical Engineering* 14.4, pages 339–346. DOI: 10.1117/12.7971842 (cited on pages 5, 49).

Porcar-Castell, A. (2011). "A high-resolution portrait of the annual dynamics of photochemical and non-photochemical quenching in needles of Pinus sylvestris". In: *Physiologia Plantarum* 143.2, pages 139–153. DOI: 10.1111/j.1399-3054.2011.01488.x (cited on pages 71, 94).

Porcar-Castell, A., J. I. Garcia-Plazaola, C. J. Nichol, P. Kolari, B. Olascoaga, N. Kuusinen, B. Fernández-Marín, M. Pulkkinen, E. Juurola, and E. Nikinmaa (2012). "Physiology of the seasonal relationship between the photochemical reflectance index and photosynthetic light use efficiency". In: *Oecologia* 170.2, pages 313–323. DOI: 10.1007/s00442-012-2317-9 (cited on page 43).

Porcar-Castell, A., E. Tyystjärvi, J. Atherton, C. Van Der Tol, J. Flexas, E. E. Pfündel, J. Moreno, C. Frankenberg, and J. A. Berry (2014). "Linking chlorophyll a fluorescence to photosynthesis for remote sensing applications: Mechanisms and challenges". In: *Journal of Experimental Botany* 65.15, pages 4065–4095. DOI: 10.1093/jxb/eru191 (cited on pages 3–6, 12, 42, 70).

Quantum GIS Development Team (2016). *Quantum GIS Geographic Information System* (cited on page 23).

Ramanathan, V. (1987). "The role of earth radiation budget studies in climate and general circulation research". In: *Journal of Geophysical Research: Atmospheres* 92.D4, pages 4075–4095. DOI: 10.1029/JD092iD04p04075 (cited on page 1).

Rascher, U., G. Agati, L. Alonso, G. Cecchi, S. Champagne, R. Colombo, A. Damm, F. Daumard, E. De Miguel, G. Fernandez, B. Franch, J. Franke, C. Gerbig, B. Gioli, J. A. Gómez, Y. Goulas, L. Guanter, O. Gutiérrez-De-La-Cámara, K. Hamdi, P. Hostert, M. Jiménez, M. Kosvancova, D. Lognoli, M. Meroni, F. Miglietta, A. Moersch, J. Moreno, I. Moya, B. Neininger, A. Okujeni, A. Ounis, L. Palombi, V. Raimondi, A. Schickling, J. A. Sobrino, M. Stellmes, G. Toci, P. Toscano, T. Udelhoven, S. Van Der Linden, and A. Zaldei (2009). "CEFLES2: the remote sensing component to quantify photosynthetic efficiency from the leaf to the region by measuring sun-induced fluorescence in the oxygen absorption bands". In: *Biogeosciences* 6.1, pages 1181–1198. DOI: 10.5194/bgd-6-2217-2009 (cited on page 13).

Rascher, U., L. Alonso, A. Burkart, C. Cilia, S. Cogliati, R. Colombo, A. Damm, M. Drusch, L. Guanter, J. Hanus, T. Hyvärinen, T. Julitta, J. Jussila, K. Kataja, P. Kokkalis, S. Kraft, T. Kraska, M. Matveeva, J. Moreno, O. Muller, C. Panigada, M. Pikl, F. Pinto, L. Prey, R. Pude, M. Rossini, A. Schickling, U. Schurr, D. Schüttemeyer, J. Verrelst, and F. Zemek (2015). "Sun-induced fluorescence - a new probe of photosynthesis: First maps from the imaging spectrometer HyPlant". In: *Global Change Biology* 21.12, pages 4673–4684. DOI: 10.1111/gcb.13017 (cited on pages 4, 5, 8, 18, 42, 45, 70, 95).

Rascher, U., E. G. Bobich, G. H. Lin, A. Walter, T. Morris, M. Naumann, C. J. Nichol, D. Pierce, K. Bil, V. Kudeyarov, and J. A. Berry (2004). "Functional diversity of photosynthesis during drought in a model tropical rainforest - The contributions of leaf area, photosynthetic electron transport and stomatal conductance to reduction in net ecosystem carbon exchange". In: *Plant, Cell and Environment* 27.10, pages 1239–1256. DOI: 10.1111/j.1365-3040.2004.01231.x (cited on page 36).

Reinhardt, K., D. M. Johnson, and W. K. Smith (2009). "Age-class differences in shoot photosynthesis and water relations of Fraser fir (Abies fraseri), southern Appalachian Mountains, USA". In: *Canadian Journal of Forest Research* 39.1, pages 193–197. DOI: 10.1139/X08-163 (cited on page 12).

Rivera, J. P., J. Verrelst, J. Gómez-Dans, J. Muñoz-Marí, J. Moreno, and G. Camps-Valls (2015). "An emulator toolbox to approximate radiative transfer models with statistical learning". In: *Remote Sensing* 7.7, pages 9347–9370. DOI: 10.3390/rs70709347 (cited on page 94).

Rossini, M., L. Nedbal, L. Guanter, A. Ač, L. Alonso, A. Burkart, S. Cogliati, R. Colombo, A. Damm, M. Drusch, J. Hanus, R. Janoutova, T. Julitta, P. Kokkalis, J. Moreno, J. Novotny, C. Panigada, F. Pinto, A. Schickling, D. Schüttemeyer, F. Zemek, and U. Rascher (2015a). "Red and far red Sun-induced chlorophyll fluorescence as a measure of plant photosynthesis". In: 42.6, pages 1632–1639. DOI: 10.1002/2014GL062943.Received (cited on pages 4–6, 13, 19, 28, 38, 42, 43, 64, 70, 73).

Rossini, M., M. Meroni, M. Celesti, S. Cogliati, T. Julitta, C. Panigada, U. Rascher, C. van der Tol, and R. Colombo (2016). "Analysis of red and far-red sun-induced chlorophyll fluorescence and their ratio in different canopies based on observed and modeled data". In: *Remote Sensing* 8.5, page 412. DOI: 10.3390/rs8050412 (cited on pages 4, 13, 23, 42, 51, 70, 74, 87).

Rossini, M., M. Meroni, M. Migliavacca, G. Manca, S. Cogliati, L. Busetto, V. Picchi, A. Cescatti, G. Seufert, and R. Colombo (2010). "High resolution field spectroscopy measurements for estimating gross ecosystem production in a rice field". In: *Agricultural and Forest Meteorology* 150.9, pages 1283–1296. DOI: 10.1016/j.agrformet.2010.05.011 (cited on pages 5, 13, 42, 43).

Rossini, M., C. Panigada, C. Cilia, M. Meroni, L. Busetto, S. Cogliati, S. Amaducci, and R. Colombo (2015b). "Discriminating Irrigated and Rainfed Maize with Diurnal Fluorescence and Canopy Temperature Airborne Maps". In: *ISPRS International Journal of Geo-Information* 4.2, pages 626–646. DOI: 10.3390/ijgi4020626 (cited on page 43).

Rouse, J. W., R. H. Haas, J. A. Schell, and D. W. Deering (1973). "Monitoring Vegetation Systems in the Great Okains with ERTS". In: *Third Earth Resources Technology Satellite-1 Symposium* 1, pages 325–333 (cited on page 47).

Rundel, P. and B. Yoder (1998). "Ecophysiology of pinus". In: *Ecology and Biogeography of Pinus (ed. D.M. Richardson)*, pages 296–323 (cited on page 17).

Running, S. W. and S. T. Gower (1991). "FOREST-BGC, A general model of forest ecosystem processes for regional applications. II. Dynamic carbon allocation and nitrogen budgets." In: *Tree physiology* 9.1_2, pages 147–160 (cited on page 38).

Ryan, M. G., D. Binkley, and J. H. Fownes (1997). "Age-Related Decline in Forest Productivity: Pattern and Process". In: *Advances in Ecological Research* 27.C, pages 213–262. DOI: 10.1016/S0065-2504(08)60009-4 (cited on page 12).

Ryan, M. G. and B. J. Yoder (1997). "Hydraulic limits to tree height and tree growth: what keeps trees from growing beyond a certain height?" In: *BioScience* 47.4, pages 235–242. DOI: 10.2307/1313077 (cited on page 12).

Ryan, M. G., D. Binkley, J. H. Fownes, C. P. Giardina, and R. S. Senock (2004). "An experimental test of the causes of forest growth decline with stand age". In: *Ecological Monographs* 74.3, pages 393–414. DOI: 10.1890/03-4037 (cited on page 35).

Ryan, M. G., N. Phillips, and B. J. Bond (2006). *The hydraulic limitation hypothesis revisited*. DOI: 10.1111/j.1365-3040.2005.01478.x (cited on pages 12, 35).

Sabater, N., L. Alonso, S. Cogliati, J. Vicent, C. Tenjo, J. Verrelst, and J. Moreno (2015). "A sun-induced vegetation fluorescence retrieval method from top of atmosphere radiance for the FLEX/Sentinel-3 TanDEM mission". In: *2015 IEEE International Geoscience and Remote Sensing Symposium (IGARSS)*. 1, pages 2669–2672. DOI: 10.1109/IGARSS.2015.7326362 (cited on page 72).

Santini, F., A. Palombo, R. J. Dekker, S. Pignatti, S. Pascucci, and P. B. Schwering (2014). "Advanced anomalous pixel correction algorithms for hyperspectral thermal infrared data: The TASI-600 case study". In: *IEEE Journal of Selected Topics in Applied Earth Observations and Remote Sensing* 7.6, pages 2393–2404. DOI: 10.1109/JSTARS.2014.2324654 (cited on page 53).

Schickling, A., M. Matveeva, A. Damm, J. H. Schween, A. Wahner, A. Graf, S. Crewell, and U. Rascher (2016). "Combining sun-induced chlorophyll fluorescence and photochemical reflectance index improves diurnal modeling of gross primary productivity". In: *Remote Sensing* 8.7, page 574. DOI: 10.3390/rs8070574 (cited on pages 43, 65).

Schreiber, U. (1986). "Detection of rapid induction kinetics with a new type of high-frequency modulated chlorophyll fluorometer". In: *Photosynthesis Research* 9, pages 261–272 (cited on pages 44, 64).

Schulze, E.-D. and M. M. Caldwell (1995). *Ecophysiology of photosynthesis*. Springer Science & Business Media (cited on page 5).

Sellers, P. J. (1997). "Modeling the Exchanges of Energy, Water, and Carbon Between Continents and the Atmosphere". In: *Science* 275.5299, pages 502–509. DOI: 10.1126/science.275.5299.502 (cited on pages 7, 72).

Shirke, P. A. (2001). "Leaf photosynthesis, dark respiration and fluorescence as influenced by leaf age in an evergreen tree, Prosopis juliflora". In: *Photosynthetica* 39.2, pages 305–311. DOI: 10.1023/A:1013761410734 (cited on page 12).

Sun, Y., C. Frankenberg, J. D. Wood, D. S. Schimel, M. Jung, L. Guanter, D. T. Drewry, M. Verma, A. Porcar-Castell, T. J. Griffis, L. Gu, T. S. Magney, P. Köhler, B. Evans, and K. Yuen (2017). "OCO-2 advances photosynthesis observation from space via solar-induced chlorophyll fluorescence". In: *Science* 358.6360, eaam5747. DOI: 10.1126/science.aam5747 (cited on page 5).

Tasissa, G. and H. E. Burkhart (1998). "Juvenile-mature wood demarcation in loblolly pine trees". In: *Wood and Fiber Science* 30.2, pages 119–127 (cited on page 36).

Thenkabail, P. S., J. G. Lyon, and A. Huete (2012). *Hyperspectral remote sensing of vegetation*. CRC Press (cited on page 1).

van der Tol, C., J. A. Berry, P. K. Campbell, and U. Rascher (2014). "Models of fluorescence and photosynthesis for interpreting measurements of solar-induced chlorophyll fluorescence". In: *Journal of Geophysical Research: Biogeosciences* 119.12, pages 2312–2327. DOI: 10.1002/2014JG002713 (cited on pages 73, 94).

van der Tol, C., W. Verhoef, J. Timmermans, A. Verhoef, and Z. Su (2009). "An integrated model of soil-canopy spectral radiances, photosynthesis, fluorescence, temperature and energy balance". English. In: *Biogeosciences* 6.12, pages 3109–3129. DOI: 10.5194/bg-6-3109-2009 (cited on pages 7, 9, 38, 72).

van der Tol, C., M. Rossini, S. Cogliati, W. Verhoef, R. Colombo, U. Rascher, and G. Mohammed (2016). "A model and measurement comparison of diurnal cycles of sun-induced chlorophyll fluorescence of crops". In: *Remote Sensing of Environment* 186.iii, pages 663–677. DOI: 10.1016/j.rse.2016.09.021 (cited on pages 7, 14, 72, 79, 80, 85).

Van Rensen, J. (1989). "Herbicides interacting with photosystem II". In: *Herbicides and Plant Metabolism*, pages 21–36 (cited on page 64).

Van Wittenberghe, S., L. Alonso, J. Verrelst, I. Hermans, J. Delegido, F. Veroustraete, R. Valcke, J. Moreno, and R. Samson (2013). "Upward and downward solar-induced chlorophyll fluorescence yield indices of four tree species as indicators

of traffic pollution in Valencia". In: *Environmental Pollution* 173, pages 29–37. DOI: 10.1016/j.envpol.2012.10.003 (cited on page 13).

Verhoef, A. and S. J. Allen (2000). "A SVAT scheme describing energy and CO2 fluxes for multi-component vegetation: Calibration and test for a Sahelian savannah". In: *Ecological Modelling* 127.2-3, pages 245–267. DOI: 10.1016/S0304-3800(99)00213-6 (cited on pages 7, 72).

Verhoef, W. (1984). "Light scattering by leaf layers with application to canopy reflectance modeling: The SAIL model". In: *Remote Sensing of Environment* 16.2, pages 125–141. DOI: 10.1016/0034-4257(84)90057-9 (cited on pages 7, 77).

Verhoef, W. (2011). "Modelling vegetation fluorescence observations : abstract." In: *7th EARSEL workshop of the Special Interest Group in imaging spectroscopy : final programme, 11-13 April 2011, Edinburgh, UK*. Pages 41–42 (cited on page 77).

Verhoef, W., C. V. D. Tol, and E. M. Middleton (2014). "Vegetation Canopy Fluorescence and Reflectance Retrieval By Model Inversion Using Optimization". In: *5th International Workshop on Remote Sensing of Vegetation Fluorescence* 1, pages 759–770 (cited on page 77).

Verhoef, W. and H. Bach (2003). "Simulation of hyperspectral and directional radiance images using coupled biophysical and atmospheric radiative transfer models". In: *Remote Sensing of Environment* 87.1, pages 23–41. DOI: 10.1016/S0034-4257(03)00143-3 (cited on pages 7, 72).

Verhoef, W. and H. Bach (2007). "Coupled soil-leaf-canopy and atmosphere radiative transfer modeling to simulate hyperspectral multi-angular surface reflectance and TOA radiance data". In: *Remote Sensing of Environment* 109.2, pages 166–182. DOI: 10.1016/j.rse.2006.12.013 (cited on pages 7, 39, 72).

Verhoef, W., C. Van Der Tol, and E. M. Middleton (2017). "Hyperspectral radiative transfer modeling to explore the combined retrieval of biophysical parameters and canopy fluorescence from FLEX – Sentinel-3 tandem mission multi-sensor data". In: DOI: 10.1016/j.rse.2017.08.006 (cited on page 7).

Verrelst, J., G. Camps-Valls, J. Muñoz-Marí, J. P. Rivera, F. Veroustraete, J. G. Clevers, and J. Moreno (2015a). "Optical remote sensing and the retrieval of terrestrial vegetation bio-geophysical properties - A review". In: *ISPRS Journal of Photogrammetry and Remote Sensing* 108, pages 273–290. DOI: 10.1016/j.isprsjprs.2015.05.005 (cited on pages 7, 72).

Verrelst, J., J. P. Rivera, C. van der Tol, F. Magnani, G. Mohammed, and J. Moreno (2015b). "Global sensitivity analysis of the SCOPE model: What drives simulated canopy-leaving sun-induced fluorescence?" In: *Remote Sensing of Environment* 166, pages 8–21. DOI: 10.1016/j.rse.2015.06.002 (cited on pages 5, 13, 70).

Verrelst, J., C. van der Tol, F. Magnani, N. Sabater, J. P. Rivera, G. Mohammed, and J. Moreno (2016). "Evaluating the predictive power of sun-induced chlorophyll fluorescence to estimate net photosynthesis of vegetation canopies: A SCOPE

modeling study". In: *Remote Sensing of Environment* 176, pages 139–151. DOI: 10.1016/j.rse.2016.01.018 (cited on page 38).

Vilfan, N., C. van der Tol, O. Muller, U. Rascher, and W. Verhoef (2016). "Fluspect-B: A model for leaf fluorescence, reflectance and transmittance spectra". In: *Remote Sensing of Environment* 186, pages 596–615. DOI: 10.1016/j.rse.2016.09.017 (cited on page 77).

Walters, R. G. (2005). "Towards an understanding of photosynthetic acclimation". In: *Journal of Experimental Botany* 56.411, pages 435–447. DOI: 10.1093/jxb/eri060 (cited on page 3).

Walter-Shea, E. A., J. Privette, D. Cornell, M. A. Mesarch, and C. J. Hays (1997). "Relations between directional spectral vegetation indices and leaf area and absorbed radiation in alfalfa". In: *Remote Sensing of Environment* 61.1, pages 162–177. DOI: 10.1016/S0034-4257(96)00250-7 (cited on page 20).

Walther, S., M. Voigt, T. Thum, A. Gonsamo, Y. Zhang, P. Köhler, M. Jung, A. Varlagin, and L. Guanter (2016). "Satellite chlorophyll fluorescence measurements reveal large-scale decoupling of photosynthesis and greenness dynamics in boreal evergreen forests". In: *Global Change Biology* 22.9, pages 2979–2996. DOI: 10.1111/gcb.13200 (cited on page 5).

Weed Science Society of America (2016). *Herbicide Mechanism of Action (MOA) Classification List* (cited on page 44).

Widlowski, J. L. (2010). "On the bias of instantaneous FAPAR estimates in open-canopy forests". In: *Agricultural and Forest Meteorology* 150.12, pages 1501–1522. DOI: 10.1016/j.agrformet.2010.07.011 (cited on page 20).

Wieneke, S., H. Ahrends, A. Damm, F. Pinto, A. Stadler, M. Rossini, and U. Rascher (2016). "Airborne based spectroscopy of red and far-red sun-induced chlorophyll fluorescence: Implications for improved estimates of gross primary productivity". In: *Remote Sensing of Environment* 184, pages 654–667. DOI: 10.1016/j.rse.2016.07.025 (cited on pages 5, 13, 38, 43).

Williams, D. L. (1991). "A comparison of spectral reflectance properties at the needle, branch, and canopy level for selected Conifer species". In: *Remote Sensing of Environment* 35.2-3, pages 79–93. DOI: 10.1016/0034-4257(91)90002-N (cited on page 17).

Yang, X., J. Tang, J. F. Mustard, J.-e. Lee, M. Rossini, J. Joiner, J. W. Munger, A. Kornfeld, and A. D. Richardson (2015). "Solar-induced chlorophyll fluorescence correlates with canopy photosynthesis on diurnal and seasonal scales in a temperate deciduous forest". In: *Geophysical Research Letters RESEARCH* 42, pages 2977–2987. DOI: 10.1002/2015GL063201.Received (cited on pages 5, 70).

Yoder, B. J., M. G. Ryan, R. H. Waring, A. W. Schoettle, and M. R. Kaufmann (1994). "Evidence of reduced photosynthetic rates in old trees". In: *Forest Science* 40.3, pages 513–527 (cited on page 12).

Young, S. J. (1998). "In scene atmospheric compensation: Application to SEBASS data collected at the ARM Site. Part II". In: *Aerospace Report ATR-99 (8407), Part II* (cited on page 53).

Zarco-Tejada, P. J., M. V. González-Dugo, and E. Fereres (2016). "Seasonal stability of chlorophyll fluorescence quantified from airborne hyperspectral imagery as an indicator of net photosynthesis in the context of precision agriculture". In: *Remote Sensing of Environment* 179, pages 89–103. DOI: 10.1016/j.rse.2016.03.024 (cited on pages 13, 36).

Zarco-Tejada, P. J., V. González-Dugo, and J. A. Berni (2012). "Fluorescence, temperature and narrow-band indices acquired from a UAV platform for water stress detection using a micro-hyperspectral imager and a thermal camera". In: *Remote Sensing of Environment* 117, pages 322–337. DOI: 10.1016/j.rse.2011.10.007 (cited on pages 13, 43).

Zarco-Tejada, P. J., J. R. Miller, A. Morales, A. Berjón, and J. Agüera (2004). "Hyperspectral indices and model simulation for chlorophyll estimation in open-canopy tree crops". In: *Remote Sensing of Environment* 90.4, pages 463–476. DOI: 10.1016/j.rse.2004.01.017 (cited on page 21).

Zarco-Tejada, P. J., A. Morales, L. Testi, and F. J. Villalobos (2013). "Spatio-temporal patterns of chlorophyll fluorescence and physiological and structural indices acquired from hyperspectral imagery as compared with carbon fluxes measured with eddy covariance". In: *Remote Sensing of Environment* 133, pages 102–115. DOI: 10.1016/j.rse.2013.02.003 (cited on page 4).

Zarco-Tejada, P. J., L. Suarez, and V. Gonzalez-Dugo (2013). "Spatial resolution effects on chlorophyll fluorescence retrieval in a heterogeneous canopy using hyperspectral imagery and radiative transfer simulation". In: *IEEE Geoscience and Remote Sensing Letters* 10.4, pages 937–941. DOI: 10.1109/LGRS.2013.2252877 (cited on page 22).

Zhang, Y., L. Guanter, J. A. Berry, J. Joiner, C. van der Tol, A. Huete, A. Gitelson, M. Voigt, and P. Köhler (2014). "Estimation of vegetation photosynthetic capacity from space-based measurements of chlorophyll fluorescence for terrestrial biosphere models". In: *Global Change Biology* 20.12, pages 3727–3742. DOI: 10.1111/gcb.12664 (cited on pages 5, 13).

Zhang, Y., L. Guanter, J. A. Berry, C. van der Tol, X. Yang, J. Tang, and F. Zhang (2016). "Model-based analysis of the relationship between sun-induced chlorophyll fluorescence and gross primary production for remote sensing applications". In: *Remote Sensing of Environment* 187, pages 145–155. DOI: 10.1016/j.rse.2016.10.016 (cited on page 36).

Zhao, F., X. Dai, W. Verhoef, Y. Guo, C. van der Tol, Y. Li, and Y. Huang (2016). "FluorWPS: A Monte Carlo ray-tracing model to compute sun-induced chlorophyll fluorescence of three-dimensional canopy". In: *Remote Sensing of Environ-*

ment 187, pages 385–399. DOI: 10.1016/j.rse.2016.10.036 (cited on pages 14, 40, 72).

Zhao, F., Y. Guo, W. Verhoef, X. Gu, L. Liu, and G. Yang (2014). "A method to reconstruct the solar-induced canopy fluorescence spectrum from hyperspectral measurements". In: *Remote Sensing* 6.10, pages 10171–10192. DOI: 10.3390/rs61010171 (cited on page 71).